Modelling the Permeability of Nitrile Rubber

A thesis presented by

Mohammed Musab Khawaja

to

The Department of Physics,
Imperial College London

in partial fulfillment of the requirements
for the degree of
Doctor of Philosophy

December 2016

Abstract

Elastomer seals are widely used in the oil and gas industry and form small but crucial parts of critical mechanical and electronic components. Ideally, to prevent damage to such components, the seals should act as impermeable barriers. However, under the high pressures and temperatures found downhole, they are liable to suffer two main types of permeation-driven failure, either by gases permeating through the entire seal, or by dissolved gases causing swelling and rupture, in a process known as explosive decompression. Neither failure mode is particularly well understood, and experimental approaches have encountered difficulties in replicating service conditions and providing insight into the mechanisms responsible.

In this work, I use a molecular-simulation-based approach to investigate the drivers of and trends in the permeation of gases as a function of the underlying polymer chemistry and the environmental conditions. I focus on two elastomers in particular that are widely used in the oil and gas industry due to their resistance to hydrocarbons and to thermal degradation: nitrile butadiene rubber, or NBR, which is a statistical copolymer of acrylonitrile and butadiene, and hydrogenated-NBR, or HNBR, which is a polymer derived from the cross-linking and saturation of NBR.

For NBR, I first develop a fully atomistic model using the OPLS-AA force-field. I demonstrate that solubility increases with acrylonitrile content, the cyano group plays a crucial role in the enhanced solubility of polar gases, and that the effects of pressure and temperature are heavily gas-dependent. In contrast, the diffusivity is found to decrease with increasing acrylonitrile content. For HNBR, I show that, while the diffusivity decreases with increasing cross-link fraction, counter-intuitively, the solubility increases. The work in this thesis provides a set of molecular-level design principles for the future development of corrosion- and decompression-resistant elastomers.

The work in this thesis was carried out at Imperial College London under the supervision of Arash A. Mostofi and Adrian P. Sutton, in collaboration with Baker Hughes.

The research presented in this thesis is my own. Wherever the work of other authors is referenced, it has been duly acknowledged and appropriately cited within the text.

The copyright of this thesis rests with the author and is made available under a Creative Commons Attribution Non-Commercial No Derivatives licence. Researchers are free to copy, distribute or transmit the thesis on the condition that they attribute it, that they do not use it for commercial purposes and that they do not alter, transform or build upon it. For any reuse or redistribution, researchers must make clear to others the licence terms of this work.

Mohammed Musab Khawaja

Acknowledgments

This research was funded by Baker Hughes, and was supported through a studentship in the Centre for Doctoral Training on Theory and Simulation of Materials at Imperial College funded by the Engineering and Physical Sciences Research Council (EPSRC), grant number EP/G036888/1. It required extensive use of high performance computational facilities: those at Imperial College as well as the UK's national facility, ARCHER, access to which was through the UK's HEC Materials Chemistry Consortium, funded by EPSRC grant EP/L000202.

The work in this thesis would not have been possible without the guidance, support and encouragement of my supervisors, Arash Mostofi and Adrian Sutton. I am also grateful to John Stevens, Jimmy Eason, Helmut Benning and David Curry, at Baker Hughes, for their engagement with and contribution to this collaborative effort. It would be remiss of me not to thank Peter Haynes for a smoothly orchestrated office relocation, and the members of my cohort and our mentor, Daniele Dini, for both the frequent cohort breakfasts as well as the games of football in unorthodox places. Finally, to my friends and family — for your patience and kindness — thank you.

Contents

1 Introduction 13
1.1 Thesis outline . . . 15

2 Industrial context 17
2.1 Oil and gas exploration . . . 17
2.2 Elastomers . . . 21
2.2.1 Cross-linking . . . 24
2.2.2 Fillers . . . 28
2.3 Seal failure . . . 30
2.3.1 Existing approaches . . . 31

3 Permeation through polymers 35
3.1 Theory . . . 35
3.2 Experiment . . . 40
3.3 Molecular simulation . . . 42
3.3.1 Solubility . . . 42
3.3.2 Diffusivity . . . 45

4 A molecular model for NBR 49
4.1 Model . . . 49
4.1.1 Intermolecular interactions . . . 49
4.1.2 Initial structure generation . . . 52
4.1.3 Equilibration . . . 58
4.1.4 Assumptions . . . 58
4.2 Computational details . . . 61
4.3 Bulk property results . . . 63
4.3.1 Density . . . 63

4.3.2 Bulk modulus . . . 66
4.3.3 Glass transition temperature . . . 70
4.3.4 Thermal expansion coefficient . . . 76
4.4 Summary . . . 78

5 Solubility in NBR 80
5.1 Method . . . 81
5.1.1 NBR model . . . 81
5.1.2 Solubility . . . 82
5.2 Results and discussion . . . 88
5.2.1 Convergence . . . 88
5.2.2 Solubility at standard conditions . . . 95
5.2.3 Solubility at elevated temperature and pressure . . . 100
5.3 Summary . . . 102

6 Diffusivity in NBR 106
6.1 Method . . . 107
6.2 Results and discussion . . . 109
6.2.1 Homogeneity and isotropy of diffusion . . . 109
6.2.2 Importance of polymer relaxation . . . 110
6.2.3 Anomalous diffusion . . . 111
6.2.4 Effect of acrylonitrile content on diffusivity . . . 114
6.2.5 Effect of acrylonitrile content on permeability . . . 117
6.2.6 Macroscopic picture . . . 121

7 Permeability in HNBR 127
7.1 Method . . . 128
7.1.1 A molecular model for HNBR . . . 128
7.1.2 Validation of the model . . . 129
7.2 Transport properties . . . 134
7.2.1 Solubility . . . 134
7.2.2 Diffusivity . . . 140

8 Conclusions 143
8.1 Further work 147

References 150

Appendix A Force-field parameters 165
A.1 Nitrile butadiene rubber 165
A.2 Gases 168

Appendix B Supplementary volume-temperature plots 169

Appendix C Republication permissions 174

List of Figures

1.1 Chemical structure of nitrile butadiene rubber 16

2.1 Schematic of an off-shore drilling rig 19
2.2 High-pressure high-temperature oil wells 20
2.3 Schematic of polyisoprene cross-linked by sulfur 25
2.4 Styrene-butadiene-styrene block copolymer structure 26
2.5 Electron microscope images of carbon black 29
2.6 Rubber bellow seal 30
2.7 Examples of explosive decompression failure in rubber O-rings 32

3.1 Permeation of gas across a membrane 37
3.2 Measuring permeability in experiment 41
3.3 Measuring solubility in experiment 41

4.1 Molecules in OPLS from which the NBR parameters are derived 52
4.2 ACN monomer fraction pre- and post-polymerisation 55
4.3 Components of butadiene in NBR 55
4.4 Limited segmental motion of NBR 57
4.5 Packing of an amorphous polymer 58
4.6 Parallel efficiency of MD simulations 62
4.7 Density as a function of ACN content 65
4.8 Pressure-volume curve obtained upon compression of NBR 68
4.9 Bulk modulus of NBR as a function of ACN content 69
4.10 Volume fluctuations during T_g simulations 71
4.11 Volume-temperature data during a T_g simulation 74
4.12 Thermal hysteresis during T_g simulations 75
4.13 T_g as a function of ACN content 76

4.14 Distribution of T_g values over 80 configurations 77
4.15 Linear thermal expansion coefficient as a function of ACN content 78

5.1 Voronoi decomposition procedure 87
5.2 Convergence of solubility with number of configurations 90
5.3 Inhomogeneity of insertions 91
5.4 Local solubilities 92
5.5 Convergence of solubility with number of insertions 93
5.6 Convergence of solubility with number of grid points 94
5.7 Convergence of solubility and free volume with α 95
5.8 Solubility in NBR as a function of ACN content versus experiment 96
5.9 Solubility in NBR as a function of ACN content, from simulation 98
5.10 Local solubility in NBR 99
5.11 Solubility in NBR as a function of temperature 101
5.12 Solubility in NBR as a function of density 103

6.1 Gas trajectories in NBR 109
6.2 Anisotropy of diffusion 110
6.3 Important of polymer relaxation to small gas diffusion 112
6.4 Anomalous and normal diffusive regimes 113
6.5 Diffusivity in NBR as a function of ACN content versus experiment 114
6.6 Diffusivity in NBR as a function of ACN content, from simulation 116
6.7 Diffusion residence times in NBR 118
6.8 Permeability in NBR as a function of ACN content versus experiment . . . 119
6.9 Permeability in NBR as a function of ACN content, from simulation 120
6.10 Permeation through semi-infinite NBR 125
6.11 Diffusion in NBR at high densities 126

7.1 HNBR cross-linking procedure 130
7.2 True cross-link fraction as a function of target cross-link fraction 131
7.3 Density of HNBR as a function of cross-link fraction 132
7.4 Glass transition temperature of HNBR as a function of cross-link fraction . 133
7.5 Bulk modulus of HNBR as a function of cross-link fraction 134

7.6 Solubility in HNBR as a function of cross-link fraction 136
7.7 Correlation between cell volume and free volume in HNBR 136
7.8 Solubility as a function of free volume and cross-link fraction 137
7.9 Maximum cluster size as a function of cross-link fraction in HNBR 139
7.10 Diffusivity in HNBR as a function of cross-link fraction 141
7.11 Permeability in HNBR as a function of cross-link fraction 142

B.1 Volume-temperature plot 1 170
B.2 Volume-temperature plot 2 170
B.3 Volume-temperature plot 3 171
B.4 Volume-temperature plot 4 171
B.5 Volume-temperature plot 5 172
B.6 Volume-temperature plot 6 172
B.7 Volume-temperature plot 7 173

List of Tables

2.1 Typical formulation of Perbunan 28
2.2 Effect of carbon black on mechanical properties of natural rubber 29

4.1 Missing NBR dihedral parameters in OPLS 53
4.2 Equilibration procedure 59
4.3 Speed-up attempts 64

6.1 Diffusive exponents of different gases in NBR 113
6.2 Comparison between simulated diffusivities in OPLS and COMPASS . . . 115

A.1 OPLS force-field atom types for NBR. 166
A.2 OPLS force-field bond types for NBR. 166
A.3 OPLS force-field angle types for NBR. 167
A.4 OPLS force-field dihedral types for NBR. 167
A.5 Non-bonded force-field parameters for gases studied 168
A.6 Bonded force-field parameters for gases studied 168

Acronyms

ACN	Acrylonitrile
COMPASS	Condensed-phase optimized molecular potentials for atomistic simulation studies
DFT	Density functional theory
GCMC	Grand canonical Monte Carlo
GROMACS	Groningen machine for chemical simulations
HNBR	Hydrogenated nitrile butadiene rubber
HPHT	High-pressure high-temperature (oil and gas wells)
LAMMPS	Large-scale atomic/molecular massively parallel simulator
LJ	Lennard-Jones
MD	Molecular dynamics
MSD	Mean squared displacement
NBR	Nitrile butadiene rubber
OPLS-AA	Optimised potential for liquid simulation - all atom
phr	Parts per hundred rubber (by mass)
SATP	Standard ambient temperature and pressure (25 °C and 100 kPa)
STP	Standard temperature and pressure (0 °C and 100 kPa)
TST	Transition state theory

1 Introduction

Elastomers are a versatile class of material. The wide range of applications that they enjoy stems from the numerous chemical compositions of the base polymer, in combination with fillers and plasticisers. The former can enhance properties such as the resistance to chemical attack by fuels, while the latter can enhance mechanical properties such as stiffness and strength [1, 2].

This diversity has led to their widespread use in sealing components such as hoses, gaskets, O-rings etc. [3], particularly in the oil and gas industry, where one of their key roles is to protect sensitive monitoring equipment from contamination by fluids in conditions found downhole, where temperatures and pressures can reach 225 °C and 200 MPa [4–6], respectively. Under these conditions two modes of permeation-driven failure have been observed. The first involves the permeation of gases through the seal, leading to corrosion of the electronic components that were intended to be protected. The second occurs upon decompression, when seals are returned to the surface relatively quickly with respect to the time spent downhole, leading to a rapid pressure reduction, followed by swelling and rupture in a process known as explosive decompression [7]. This latter phenomenon is driven by the initial permeation of gases into the seal, saturating some of the voids naturally dispersed throughout the rubber [8], followed by the insufficiently rapid egress of gases out of

the seal when the external pressure is relieved [9]. It can lead to the failure of critical tools used for the purposes of telemetry. Such failures have proven costly to oil and gas companies such as Baker Hughes [10], with whom this work has been conducted. This issue could be approached in a top-down manner, in which different choices of material for the seals could be tested with the underlying aim of reducing gas permeabilities. The disadvantage of this method is that it would give limited insight into the mechanisms behind seal failure, the understanding of which could enable better-informed choices of materials. Furthermore, it would be difficult to perform experiments in conditions reflecting those found downhole.

The permeation of small gases through a polymer membrane can be described by the solution-diffusion model [11], in which the boundary conditions for diffusion through the polymer are set by the product of the solubility coefficient and the external pressures on either side of the membrane, using Henry's law [12]. Therefore, one way of ameliorating the corrosion and decompression problems is to separately focus on the constituent parts of the permeability — the solubility and the diffusivity. The former inherently limits the amount of gas absorbed by the seal and sets the pressure gradient that produces the rupture, while the latter determines the mobility of the gas. To do this, a molecular-level understanding of the factors controlling permeability in the elastomer is required. Hence molecular simulation is a natural choice of investigative tool in this work. This approach permits a finer degree of control than is possible in experiment, and results in a nanoscopic picture of the permeation process. Although the nature of the gas-polymer interaction is governed by quantum mechanics, density functional theory (DFT) simulations are incapable of encapsulating the length- and time-scales over which permeation takes place in an elastomer, and standard approximations for the exchange and correlation functional are unable to account for dispersion interactions, which are an important component of the gas-polymer interaction.* Instead, I have used classical molecular dynamics, utilising fully atomistic force-fields to approximate the interatomic interactions, sacrificing accuracy in exchange for the ability to observe the permeation process. This is a widely used tactic, and has found success across disciplines, from protein folding [15] to fluid dynamics [16]. Representing every atom ex-

*Only recently has there been some progress on the development of non-local dispersion-corrected functionals (e.g., Refs. [13, 14]), and it is still an area under active development.

plicitly is more computationally costly than grouping atoms together in a coarse-grained manner, e.g., by combining the four atoms of a CH_3 group into a single 'united-atom'. However, coarse-grained approaches come at the expense of chemical specificity, something that is critical when investigating permeation of specific gases through specific materials.

Two elastomers in particular are the focus of this work: nitrile butadiene rubber (NBR), a copolymer of butadiene and acrylonitrile (ACN), shown in Figure 1.1, and hydrogenated-NBR (HNBR), a derivative of NBR formed by selective saturation of the carbon-carbon double bonds found in the butadiene monomers. NBR is a popular choice of material for seals in the oil and gas industry due to its mechanical properties and resistance to hydrocarbons and thermal degradation [2, 17]. HNBR is preferred when the seals are required to perform under high temperatures [2, 18]. While both have been studied in experiment, there is a paucity of freely available molecular models. Existing models of NBR [19–22] rely exclusively on the COMPASS* force-field [23], available from BIOVIA [24] through their proprietary Materials Studio package. The parameters of this force-field are held within an encrypted database, and are thus inaccessible to the user. Without knowing what parameters are in use, it is difficult to debug any problems that might arise, and to understand the relationship between the parameters and any properties of interest.† In this thesis I have sought to remedy this issue by developing a model using a freely available force-field, which I have then used to study the permeation of small gases in NBR as a function of the chemistry of the polymer and environmental conditions. By using an extension of this model to HNBR, developed by Molinari [25], I have also been able to study permeation in HNBR. It is hoped that the insights developed in this work of the permeation process in these two widely used elastomers can be used to inform the design and development of higher performance materials, resistant to permeative failure.

1.1 Thesis outline

In chapters 2 and 3, I cover the industrial background to the problem and the techniques used to study permeation using theory, simulation and experiment. In chapter 4, I develop

*Condensed-phase optimized molecular potentials for atomistic simulation studies

†This black box approach also runs against the grain of good science.

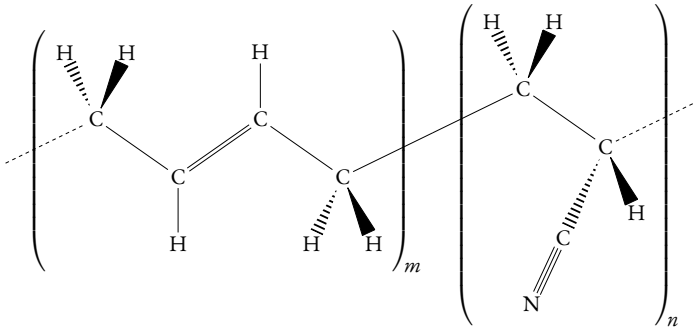


Figure 1.1: Nitrile butadiene rubber, a random copolymer of butadiene (left) and ACN (right).

a model for NBR using the OPLS-AA* force-field [26], and verify it by computing bulk properties such as density and glass transition temperature and comparing them to experiment.† This model is used in chapter 5 to compute solubilities in NBR as a function of ACN content, temperature and pressure. Solubilities are obtained using a biased variant of the Widom particle insertion technique, and care is taken to explicitly demonstrate the convergence of the method.‡ I demonstrate the importance of the cyano group in ACN to the solution of polar gases in particular, by breaking down the total solubility into its per-atom, localised analogue, using a Voronoi cell decomposition method. In chapter 6, the work on NBR concludes with an investigation of the diffusivity as a function of ACN content, which is then combined with the solubility results to calculate permeabilities. Particular emphasis is placed on linking these simulation results back to the macroscopic picture of permeation through an elastomer seal, using a simple yet instructive model. In chapter 7, I present Molinari's [25] algorithm for cross-linking and hydrogenating NBR to form HNBR. I implement this algorithm, verify it by computing bulk properties, and use it to compute solubilities and diffusivities as a function of cross-link fraction. I summarise my findings in chapter 8, and discuss potentially fruitful avenues for further work.

*Optimized Potentials for Liquid Simulations — All Atom

†The work in this chapter represents my contribution to a collaborative publication with Molinari [25].

‡The work in this chapter has also been published [27].

2

Industrial context

This chapter covers the industrial problem that motivates this thesis: elastomer seal failure via permeation in the context of oil and gas exploration. An overview of the drilling process is given to highlight the environmental conditions in which the seals operate, in the form of high temperatures and pressures, frequent shocks from fragments of rock and chemical exposure. The influence of cross-linking and additives such as filler particles on the material properties of the elastomer are described, to illustrate why elastomers are so widely used for sealing purposes. Finally, the specific failure mechanisms of interest in this work are discussed, namely corrosion and explosive decompression, and previous approaches to tackling them through experiment and finite element modelling described.

2.1 Oil and gas exploration

The production of petroleum represents a multi-trillion dollar industry and is a vital part of global energy requirements. Oil wells have been drilled for nearly 2000 years, since bamboo pipes attached to drill bits were used in China to dig wells up to a depth of 200 m [28]. The techniques have changed since then but the overall principles remain the same.

From the surface, a series of 10 m long steel pipes are connected together ('tripped'), until they reach the bottom hole assembly, or BHA. The BHA consists of the drill collar, an especially thick series of pipes whose weight assists the drilling, and the drill bit. Depending on the type of bit, the rock is fractured by compressive failure and/or shearing. Once a hole of diameter 0.1–1 m is created by the drill bit, the integrity of the hole needs to be protected, both to prevent the well from collapsing, and to act as a barrier to unwanted contaminants. This is done by a process known as casing, which consists of running a pipe down the well and filling any gaps between the well and the rock formation with cement. This process is repeated with successively smaller drill bits and a telescopic series of pipes, with cement added between the casing and rock at each stage to fortify the formation, as shown in Figure 2.1.

When the drilling is completed, perforations are made in the part of the drill casing that lies in the hydrocarbon production zone, creating a path for the flow of oil and gas back to the surface. Stimulation of the well will typically be required at some point to increase the rate of production [31]. In the nineteenth century this was done using dynamite. After being lowered into the well and detonated, the exploding nitroglycerin would create cracks inside the rocks below [32]. Nowadays more sophisticated methods are used such as acidising, where acid* is pumped into the well to break down lime based rocks.

Critical to the entire drilling process is the drilling fluid, known as drilling mud. When pumped in at high pressure through the drill bit it is able to remove rock cuttings from the drill string [33]. In its most common form it is a suspension of bentonite clay† in water [34, 35]. The bentonite suspension is a viscous, shear thinning fluid. When the mud stops it becomes gel-like, thereby suspending the cuttings [36]. This helps to build up a 'mud cake' around the completed well, which consolidates the hole structurally and prevents other fluids from entering [37]. By acting as a lubricant, the fluid is able to reduce mechanical friction between the drill bit and rock. Furthermore, its high thermal conductivity‡ helps to dissipate any heat generated by both the drilling and the geothermal gradient deep inside the well, where temperatures can reach over 300 °C.

*Typically hydrochloric acid is used, at a concentration of 5 M [32].

†$Al_2O_3 4\,SiO_2 H_2O$

‡Drilling mud typically has a thermal conductivity of 1.7 $m^{-1}\,K^{-1}$ [38] compared to 0.6 $m^{-1}\,K^{-1}$ for water, at standard temperature and pressure (STP) [39].

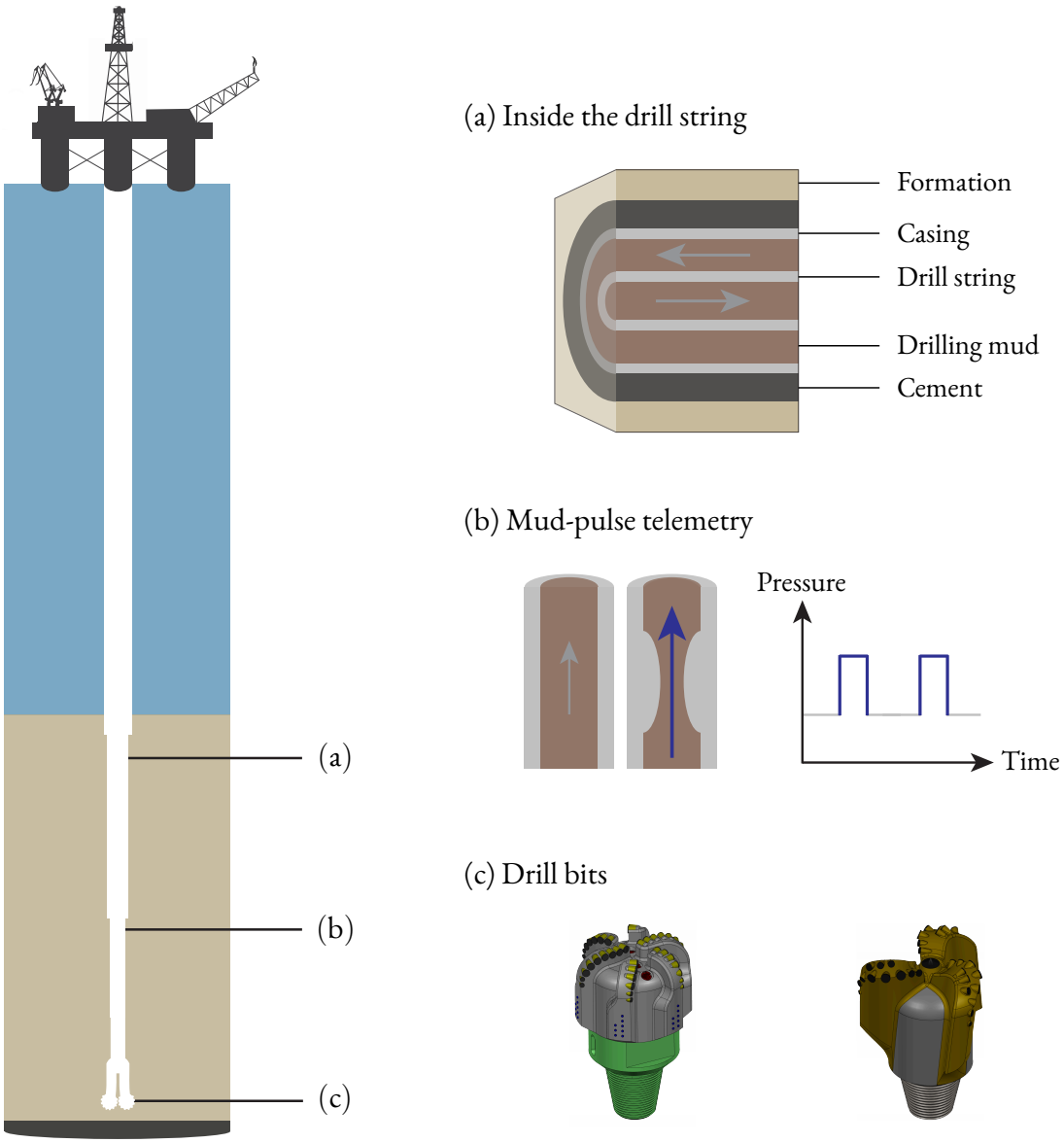


Figure 2.1: Schematic of an off-shore drilling rig.
(a) At points along the drill string, the casing is separated from the rock formation via cement. Drilling fluid is pumped down the drill string through the drill bit, flowing back up to the surface through the region between the drill string and the casing, known as the annulus, along with any rock cuttings,
(b) Mud-pulse telemetry enables operators at the surface to communicate with and control downhole tools, by sending acoustic signals through the drilling mud. One way of accomplishing this is by opening and closing a valve, causing a fluctuation in the pressure.
(c) Polycrystalline diamond compact (PDC) drill bits are widely used in modern drilling rigs, removing rock using a shearing action. The PDC bit with fewer 'cutters' (right) is able to cut deeper and sustain an increased torque, but has a shorter lifespan [4]. CAD drill bit models obtained from GrabCAD [29, 30].

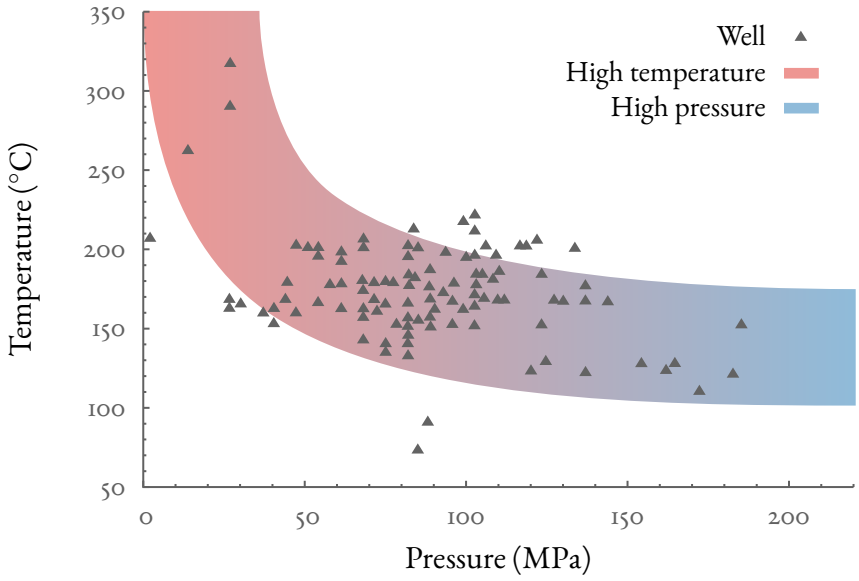


Figure 2.2: High-pressure high-temperature oil wells. Most wells have temperatures and pressures below 200 °C and 100 MPa, respectively. Data and style of figure from Schlumberger [42], based on wells drilled worldwide between 2007 to 2010.

Figure 2.2, which shows the distribution of oil wells drilled between 2007 and 2010 as a function of temperature and pressure, demonstrates that such high temperatures are generally rare, with most high-pressure high-temperature (HPHT) wells having temperatures below 200 °C and pressures below 100 MPa. As shown, there is a trade-off between extreme pressures and extreme temperatures, with most wells demonstrating one or the other but not both. Sources of high pressure inside the well include lithostatic pressure from the rock formation, hydrostatic pressure from the body of water[*] (if any), and fluid pressure from, e.g., the drilling mud and the released hydrocarbons. The drill string is also frequently subjected to shocks,[†] since, during the drilling process, stress builds up around the bit and is only relieved when the formation is broken, sending fragments of rock up the casing.

Throughout the drilling and extraction process, it is important to be able to monitor and

[*]Deepwater Horizon was considered an 'ultra-deepwater' rig, drilling the deepest oil well in history at nearly 11 km below sea level, but only 1 km of that depth was in open water and the rest was through rock [40].

[†]These shocks can be as high as 100g [41], where g is the acceleration due to gravity.

control what is occurring downhole, e.g., to determine what type of rock is being drilled and alter the direction of the drill bit to seek out reservoirs of hydrocarbons. While a fully hardwired electronics solution would be ideal, it would require potentially kilometres of special drill pipes and electronics that must function continuously under tough conditions. Instead, pressure waves are sent along the drill string from a so-called bi-directional communication and power module (BCPM) by modulating the flow of the drilling fluid, in a process known as mud-pulse telemetry, illustrated in Figure 2.1. Naturally there is a lot of noise in the signal that is being sent through kilometres of fluid, so typical data transfer rates are limited to around 10 bits/second [43].

The BCPM is a critical component of the set-up as it is responsible for relaying information from the hole to the surface, and commands from the surface to the hole. This module needs to be protected from the environment downhole, e.g., from entrainment of fluid, so that it functions reliably. Baker Hughes have found that it is NBR and HNBR seals inside the BCPM that are failing due to swelling and/or explosive decompression, jeopardising the ability to measure and control the drilling process, and costing millions of dollars in repairs. Before the failure mechanisms can be described, however, the relevant material properties must be discussed.

2.2 Elastomers

An elastomer is any type of polymer that exhibits highly elastic behaviour, meaning that it can be deformed extensively before returning to its original shape [44]. For example, a rubber band can be stretched to multiple times its original length but still snap back, whereas a steel wire can only be stretched by approximately 1 % before it begins to deform plastically [45]. This property makes rubber* invaluable for sealing applications, as it is able to conform to and change with its surroundings.

Entropy is the driving force behind this elasticity. This can be shown by approximating the polymer as an ideal, or Gaussian, chain, corresponding to a random walk. Assuming the polymer has N bonds of length b, with one end fixed at the origin, the probability of the

*The terms rubber and elastomer are interchangeable [46].

other end being at a distance R — referred to as the end-to-end distance — is [47]

$$P(R) = \left(\frac{3}{2\pi N b^2}\right)^{3/2} \exp\left(-\frac{3R^2}{2Nb^2}\right) , \tag{2.1}$$

in the limit of large N.* The number of possible configurations, Ω, that the ideal chain can take up is [45]

$$\Omega(R) \propto \exp\left(-\frac{3R^2}{2Nb^2}\right) . \tag{2.2}$$

Hence the entropy S and free energy F at temperature T and constant internal energy U are given by

$$S = k_B \ln \Omega , \tag{2.3}$$

$$\propto -\frac{3k_B}{2Nb^2} R^2 + \text{constant} , \tag{2.4}$$

$$F = U - TS , \tag{2.5}$$

$$\propto \frac{3k_B T}{2Nb^2} R^2 + \text{constant} , \tag{2.6}$$

where k_B is the Boltzmann constant. The tension, f, that pulls on the ends of the ideal polymer chain is then

$$f = -\frac{\partial F}{\partial R} , \tag{2.7}$$

$$= -\frac{3k_B T}{Nb^2} R . \tag{2.8}$$

This force is not due to a change in internal energy, which was held fixed, but a change in entropy. When the polymer is stretched there are fewer configurations that it can take. The tension effectively tries to return the chain to a state with more possible configurations and thus higher entropy [49].†

*This is a consequence of the Central Limit Theorem [48].

†The force can be compared to a Hookean spring with spring constant $k = 3k_B T/Nb^2$, which is why a bead-spring model, e.g., that of Kremer-Grest [50], is often used to model polymers.

The degree of stretching attainable by polymers can be estimated from the end-to-end displacement, $\vec{R}$:

$$\vec{R} = \sum_{i=1}^{N} \vec{r}_i \,, \tag{2.9}$$

where $\vec{r}_i$ is the position of monomer i. The equilibrium end-to-end distance, R_{eq}, is then found by taking the ensemble average over all possible configurations:

$$\langle R_{\text{eq}}^2 \rangle = \sum_{i=1}^{N} \sum_{j=1}^{N} \langle \vec{r}_i \cdot \vec{r}_j \rangle \,, \tag{2.10}$$

$$= \sum_{i=1}^{N} \sum_{j=1}^{N} b^2 \delta_{ij} \,, \tag{2.11}$$

$$= Nb^2 \,, \tag{2.12}$$

$$\Rightarrow \sqrt{\langle R_{\text{eq}}^2 \rangle} = \sqrt{N} b \,, \tag{2.13}$$

where δ_{ij} is the Kronecker delta and $\langle \vec{r}_i \cdot \vec{r}_j \rangle = b^2 \delta_{ij}$ because there is no correlation between the directions of different bonds, since the chain is Gaussian. The largest possible end-to-end distance is attained when the chain is pulled taut, and is $R_{\text{max}} = Nb$. Therefore the maximum strain, ε_{max}, is given by [47]

$$\varepsilon_{\text{max}} = \frac{R_{\text{max}}}{\sqrt{\langle R_{\text{eq}}^2 \rangle}} \,, \tag{2.14}$$

$$= \sqrt{N} \,. \tag{2.15}$$

Although this is an approximation, as the random walk model used here allows overlaps between bonds,* it illustrates how an elastomer is able to deform to multiple times its original length.

An important property of all elastomers is their glass transition temperature [51], T_g,

*Resolving this would require considering the correlation between the directions of different bonds in Eqns. (2.10) and (2.11).

which is defined as the temperature above which the material softens due to the beginning of long-range co-ordinated motion of molecules [45]. This softening is manifested as a drop in Young's modulus by a factor of approximately 10^3 [45], and can also be seen as a discontinuity in the gradient of the density as a function of temperature. Below T_g, the material will be hard and brittle, as the molecular motion is restricted to short range thermal vibrations. This is the glassy state, in which the elastomer lacks long-range order. Above T_g, the chains are able to flow along their own contours, following a snake-like motion known as reptation [47]. This freedom of large-scale segmental movement above T_g means most *polymers* are not able to achieve such large deformations reversibly, especially at high temperatures. *Elastomers* overcome this by forming cross-linked networks.

2.2.1 Cross-linking

When natural rubber, a compound mainly comprised of polyisoprene, is taken from trees such as *Hevea brasiliensis*, it comes out in colloidal form as latex [52]. Once coagulated and processed, it forms a highly elastic and waterproof material at room temperature [45]. This form of rubber was used for over 2000 years. However, its practicality is limited by the fact that at slightly higher temperatures it becomes sticky and at lower temperatures it becomes brittle [3]. Furthermore, it is easily dissolved in toluene and acetone, for example [53].

The real breakthrough came in the nineteenth century when Charles Goodyear* discovered the process of vulcanisation. He combined sulfur with natural rubber and heat, to find the resulting compound had none of the stickiness or brittleness of the original rubber [55]. In this vulcanisation process (also known as curing or cross-linking), the polyisoprene chains become cross-linked via (poly)sulfide bonds, as shown in Figure 2.3. This constrains the long-range movement of the chains in their rubbery state ($T > T_g$), such that while the resulting structure is still able to deform, it tends to return to its original configuration [45]. Eventually enough cross-links can form between the chains to result in an interconnected network, such that a Maxwellian demon could traverse across the entire system hopping from one covalent bond to the next [45].

*The same Goodyear for whom the tyre company would later be named [54].

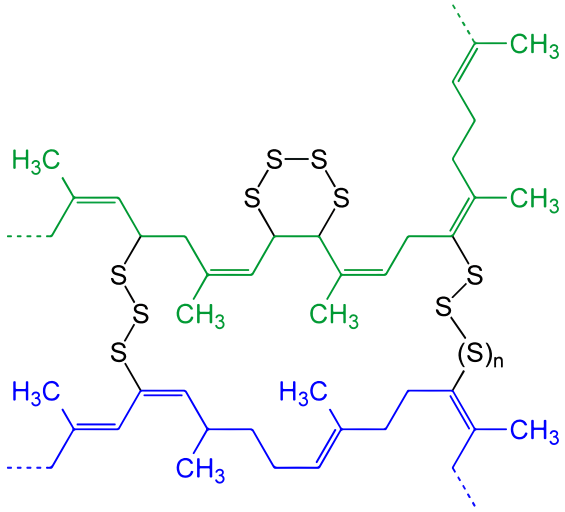


Figure 2.3: Schematic of two chains of natural rubber (polyisoprene) cross-linked by sulfur. The sulfur atoms form links between different chains or even within the same chain. This reduces the degrees of freedom of the polymer, forming a reversibly deformable network. In reality the cross-link density of elastomers is not as high as shown in this schematic, as otherwise the material would be more resin-like than rubber-like. Reproduced from Wikimedia Commons (CC0 1.0 Universal license) [56].

Vulcanised natural rubber is an example of a thermoset elastomer. All thermoset elastomers are chemically cross-linked and therefore insoluble. This makes their recycling difficult, as they cannot be melted and will instead burn. Thermoplastic elastomers are not chemically cross-linked, however. Instead, the cross-links are weaker dipole or hydrogen bonds. This means it is easy to process them as melts, thus making them amenable to recycling. One of the most widely used thermoplastics is styrene-butadiene rubber (SBR), which is made of alternating blocks of polystyrene and polybutadiene, as shown in Figure 2.4 [58]. The polystyrene phase exists in blocks with a T_g above the ambient temperature and is therefore glassy, while the polybutadiene phase has a low T_g and is rubbery. There is a phase separation of the blocks, due to the low entropy gain on mixing. To obtain the required elastomeric properties, the molecular weights of the blocks are altered so that the amorphous phase dominates [45]. However, thermoplastics do not have the same high temperature performance as cured elastomers [58]. SBS rubber cannot be used beyond temperatures of 100 °C, for example [59]. As I am interested in the use of elastomers in high temperature oil and gas wells, I restrict my attention to thermoset elastomers, of which

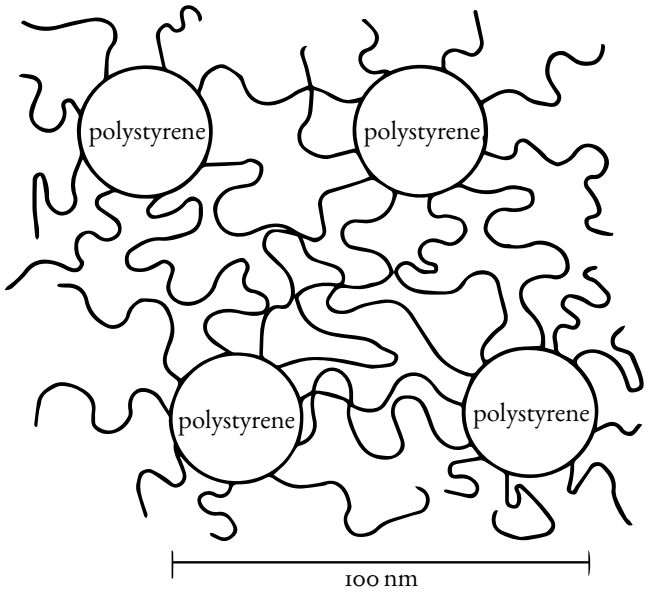


Figure 2.4: Styrene-butadiene-styrene block copolymer structure. The polystyrene blocks tend to aggregate and act as cross-links for the long, rubbery polybutadiene sections. In a typical formulation, the polystyrene will make 20 % of the SBS rubber by mass and each block will have a radius of $\approx$ 10 nm [45]. Reproduced and modified from Wikimedia Commons (public domain) [57].

NBR and HNBR are examples.

The way in which thermosets are cured affects their material properties. Vulcanisation with sulfur is an example of covalent curing, and is one manner in which NBR can be cross-linked. It requires the presence of unsaturated carbon-carbon double bonds, which are reactive [3]. The sulfur atoms then link carbon atoms on one chain to another. If the resulting elastomer is mainly cross-linked by polysulfide bonds as opposed to individual sulfur atoms, it will have a greater tensile strength. This is attributed to the ability of the sulfur-sulfur bonds in the cross-link to break reversibly, thereby relieving any applied stress that might cause failure [58]. However, the instability of the sulfur-sulfur bond compared to the carbon-sulfur bond means that the elastomer will be more susceptible to thermal degradation [3]. This is why elemental sulfur is replaced in some cures with larger molecules that contain sulfur, such that the molecule acts as a sulfur donor [60]. Examples include tetramethylthiuram disulfide (TMTD) [61] and dithiodimorpholine (DTDM) [62]. This process is known as (semi-)efficient vulcanisation [5].

Saturated polymers such as HNBR cannot be cross-linked with sulfur [3]. Peroxide-based cures are an alternative. These react with polymer chains by removing hydrogen from the backbone carbon, creating active radical sites [63]. Radicals on different chains then become attached to one another, creating a carbon-carbon cross-link [64]. This is stronger and more thermally stable than a carbon-sulfur link [3]. Another example of a thermoset cured this way is EPM rubber, a copolymer of ethylene and propylene [63].

Thermoset elastomers can also be cured by ionising radiation, in the form of electron beams or gamma rays. This method can be used for both NBR and HNBR [65]. The radiation induces scission and cross-linking of chains, the balance of which will determine the material properties [66]. If chain scission dominates, then the elastomer softens and becomes sticky [58]. Radiation promoting agents, known as prorads, are used to enhance radiation induced cross-linking, by forming radicals faster than typical curing agents, resulting in a lower radiation dose being required [67]. Trimethylolpropane trimethacrylate is a common example of a prorad [68]. Radiation-cured elastomers exhibit lower thermal degradation rates than chemically-cured elastomers. However, the maximum operating temperature is typically lower: 150 °C versus 280 °C for perfluoroelastomers, for example [68].

Ingredient	Purpose	Quantity (phr)
Perbunan	rubber	100
Sulfur	vulcanising agent	1.5
Zinc Oxide	vulcanisation accelerator	5
Vulkacit AZ ®	vulcanisation accelerator	1.8
Vulkacit P ®	vulcanisation accelerator	1.5
Phenyl-β-naphthylamine	anti-oxidant	1
Vulcanisation temperature	142 °C	
Vulcanisation time	30 min	

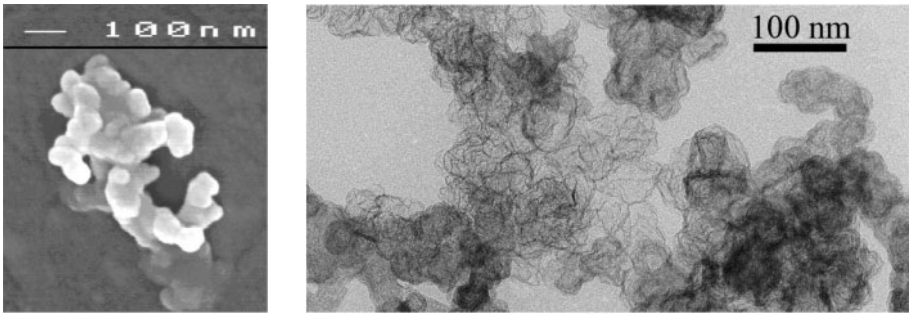
Table 2.1: Typical formulation of Perbunan, a type of NBR consisting of 27 % ACN content. Units are parts per hundred rubber (phr) by mass. Data from Van Amerongen [71].

Curing can be a slow process and so accelerators are used to speed up the process from hours to minutes [3]. The most common examples are zinc oxide and stearic acid [69]. Delayed action accelerators, such as zinc dibutyl dithiocarbamate [70], can be used to introduce a delay at the start of the curing process, e.g., if a compound takes a long time to fill a heated mould [3]. Other additives commonly used include antidegradants that slow down the deterioration caused by ozone, oxidation and/or light, by providing sacrificial protection [68]. Plasticisers are also used to aid in processing. They are normally based on aromatic hydrocarbons and reduce the viscosity of the uncured compound [3]. A typical formulation of a NBR is shown in Table 2.1. There is a key ingredient missing from this formulation, however, that is present in practically all commercial elastomers: filler particles.

2.2.2 Fillers

Fillers are nanoparticles used to change the mechanical properties of elastomers. They typically increase tensile strength, hardness and stiffness, while reducing the breaking elongation [58]. They tend to form aggregates that vary in size from tens to hundreds of nanometres, which can themselves coalesce to form microscopic agglomerates, as shown in Figure 2.5. Their effect on the elastomer can be tuned by changing their quantity and/or shape [72].

The filler bonds to the polymer through van der Waals forces [74]. The surface of the filler is also bonded covalently to free radicals on the polymer chains [74]. This physical and



(a) Scanning electron microscope image of carbon black aggregate

(b) Transmission electron microscope image of carbon black agglomerate trapped in rubber

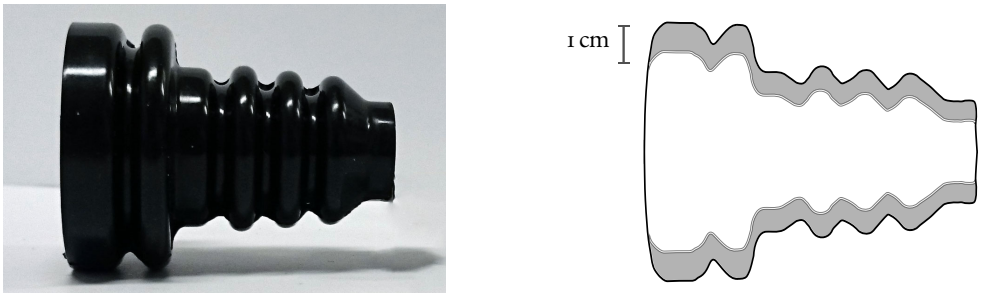
Figure 2.5: Images of carbon black structures, from the nanoparticles (small white circles) and aggregates in (a), to the agglomerates (dark grey) inside the rubber (light grey background) in (b). Reproduced with permission from Jha *et al.* [73].

Filler content (phr)	25	50	75
Shore A Hardness	51	62	72
300 % Modulus (MPa)	7	9	11
Tensile Strength (MPa)	22	24	25
Breaking Elongation (%)	700	600	550

Table 2.2: Effect of N550 carbon black on mechanical properties of vulcanised natural rubber. While increasing the filler content increases the hardness and modulus of the elastomer, it does so at the expense of its maximum extensibility. Carbon black quantity is measured in parts per hundred parts of rubber (phr), by mass. Data from Gent [58].

chemical bonding allows local segmental motion while preventing long-range motion, i.e., flow, and thus raises the glass transition temperature of the material. The mechanical interlocking of the filler with the local polymer network contributes to the increase in stiffness, as the free volume of the elastomer is reduced and thus so is the deformation for a given applied stress [68].

The most widely used filler is carbon black. It is produced by the partial combustion of oil or gas. Its effect on the mechanical properties of natural rubber as a function of filler mass fraction is shown in Table 2.2. Another compound often used as a filler is silica. Although it provides greater tear strength and thermal ageing properties to elastomers than carbon black, and is translucent and so can have coloured pigments added to it, it is not



(a) Photo **(b)** Cross-section

Figure 2.6: Rubber bellow seal. The seal is held in metallic grooves on both ends, and is squeezed laterally as part of a pump in the BCPM. Ideally the seal should act as a barrier to stop fluids from outside the seal mixing with fluids inside, but upon swelling and/or decompression this is no longer the case and the pump fails.

available in as wide a range of sizes and structures [3]. Since it is also more expensive, and one of the purposes of fillers is to reduce costs, silica is therefore not as widely used [58].

2.3 Seal failure

Elastomer seals play small but vital roles in industrial components, and, as evidenced by the Challenger disaster [75], their failure can have catastrophic consequences. Seals are typically held in place by some form of metallic housing. Their most common mode of failure is via extrusion, when the seal and its housing are subjected to higher pressures and/or shock loading than they were designed to handle, forcing the seal either wholly or partially out of its groove [76].

In this thesis the mode of failure of interest is not due to extrusion, however, but to permeation. Baker Hughes have, on occasion, detected corrosion damage to sensitive electronic parts in the drill string, as well as outright failure of BCPM tools that contain rubber bellow seals (Figure 2.6), resulting in millions of dollars of repairs. Sometimes this occurs without damage to the seal, meaning that gases have permeated entirely through.* On other occasions the seal itself may exhibit visible signs of damage, such as being swollen, or, in extreme cases, ruptured, through a process known as explosive decompression. The first stage

*Their internal testing has told them that partial extrusion is not to blame, i.e., gases are going through the seal, not through some gap between the seal and its housing.

of explosive decompression is the ingress of gases into the elastomer. Sources of gas include the drilling mud as well as the oil itself, which may have natural gas dissolved in it.

Meanwhile the elastomer is not a perfectly homogeneous material, containing microscopic voids due to the manufacturing process [58] that act as sinks for gas molecules. Fillers can also potentially act as sinks for gases, since, while the bulk of the filler is effectively excluded volume, the surface can either attract or repel gas molecules, depending on its functionalisation and the specific gas species [7, 77].

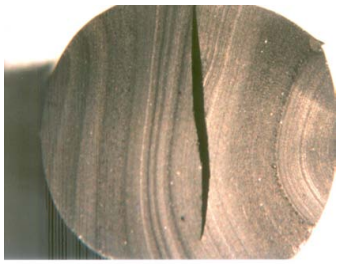
The high temperatures and pressures found downhole (Figure 2.2) can accelerate the permeation of gases into the seal. Furthermore, the length of a typical drilling operation means that it can be weeks before the seals are returned to the surface, leaving plenty of time for gases to enter the material. In contrast, once the drilling operation is complete the seals are returned to the surface in a matter of hours.* It is this mismatch of timescales that is the root cause of explosive decompression. The sudden release in pressure outside the seal as it returns to ambient conditions causes a large pressure gradient that attempts to drive the diffusion of gases back out of the seal.† If the seal is unable to sustain these forces, it either swells due to the gas-driven enlargement of internal voids or defects, or cracks develop, rupturing the seal outright. Examples of seal failure by explosive decompression are shown in Figure 2.7.

2.3.1 Existing approaches

The experimental approach to studying explosive decompression is to subject elastomer seals to a long period of compression under a gas such as CO_2, under high temperature, followed by a period of rapid depressurisation. This process is usually repeated multiple times before any decompression is found. The seal is then visually inspected for signs of damage, and cross sections are taken to determine the type of failure that occurred in the form of cracks or blisters, with the former being the most commonly observed, even at low depressurisation rates [7]. In order to have a clear picture of the material failure, translucent and unfilled elastomers are often used, e.g., those made of silicone, which are more liable to

*For example, one manufacturer quotes 18 hours to retrieve the drill string from a depth of 1 km [78].

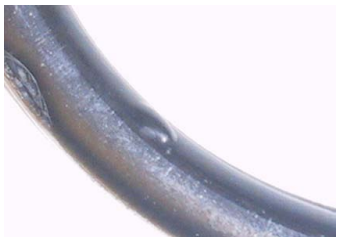
†As I will show in chapter 6, the distance the gas is able to diffuse over the time it takes to raise the drill string is short, relative to the width of the seal.



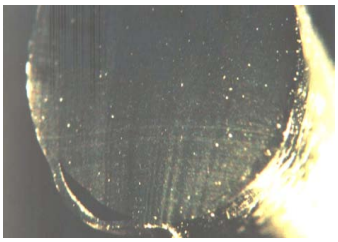
(a) Single crack



(b) Multiple cracks



(c) Blister



(d) Internal crack under blister

Figure 2.7: Examples of explosive decompression failure in rubber O-rings. Long, single cracks are indicative of rapid failure, whereas multiple short cracks are found when the seal fails gradually. Blistering can occur on a free surface of the O-ring that was not facing the seal's housing. However, these blisters can deflate over time, leaving no visible signs of damage until cut open, at which point internal cracks reveal themselves. Images reproduced from Ho *et al*. [79] (Open Government Licence).

swelling and rupture than commercial formulations of seals, which always contain fillers. Therefore the experiments do not give insight into the behaviour of elastomer seals as used in industry. Furthermore, the pressures and temperatures used are low in comparison to those found in an oil and gas exploration context, and when higher pressures and temperatures were used by one author, it was found that the elastomer degradation was so severe it was not possible to diagnose any specific failure mechanism [80].

Existing approaches to modelling explosive decompression have been at the finite element level [81, 82]. This is particularly challenging due to the coupling of mechanical, transport and thermal phenomena in an elastic medium — a highly non-linear problem. For example, the rate of gas diffusion through the seal depends on the concentration gradient, but the presence of gas in the seal can have a plasticising effect on the polymer [7], increasing the available free volume and mobility of the gas molecules, which in turn changes the concentration gradient, which in turn changes the region of the polymer being plasticised etc.* Instead, a subset of these phenomena are usually tackled. However, this makes it difficult to compare the predictions of the model to experiment. Routh [81], for example, focused on gas transport and stress-field modelling, but, due to the difficulty in obtaining solubility data under the elevated conditions found in an industrial context, made the approximation that data from experiments conducted under ambient conditions could be used. As I will show in chapter 5, for the case of small gas solution in NBR, at least, this approximation is flawed.

In practice, the main approach used in the oil and gas industry to avoid permeative seal failure is to use decompression-resistant elastomers, typically (per)fluoroelastomers† with high volume fractions of fillers and high cross-link densities [79, 81]. However, these seals are an order of magnitude more expensive than the non-fluorinated seals normally used such as NBR and HNBR [83], and thus are not ideal from a commercial perspective.‡

*Effectively, the gas diffusivity through the material is a function of the concentration, not a constant.

†Fluoroelastomers are organic polymers with partially fluorinated backbones, whereas perfluoroelastomers have fully fluorinated backbones.

‡Another potential approach to reduce the incidence of failure would be to raise the drill string more slowly, reducing the depressurisation rate. However, firstly, it is not clear how much of a reduction would be required — it could well be multiple orders of magnitude. Secondly, drilling is an expensive business, with day rates for deepwater rigs reaching up to $0.5 m [84], meaning that it would most likely be cheaper to simply use perfluoroelastomers.

Instead, the ultimate aim of this work is to lead to suggestions for modifying NBR and HNBR seals, not replacing them outright, to reduce the permeation of gases into the rubber, and ameliorate the explosive decompression problem.

3

Permeation through polymers

The characterisation of permeation through polymers is a topic relevant to a diverse range of fields, from creating water purification membranes [85] to designing slow-release drugs [86]. This chapter covers the methods used to study permeation in dense polymer systems. First, the solution-diffusion model — a set of equations that govern the transport of gases through membranes — is derived. Then the history of the experimental study of permeation is reviewed in brief, to illustrate the techniques used by experimentalists, and to highlight previous work in the literature on the permeability of gases in NBR. Finally, the different approaches to studying permeation via nanoscale computational methods are presented.

3.1 Theory

Developed in the nineteenth century [87], the pore-flow and solution-diffusion models were the first to describe permeation through polymers. In the pore-flow model, the transport of gases is a pressure-driven convective process through small but permanent pores inside the material. These pores have the ability to act as molecular sieves, separating gases by size, and therefore this model has found particular success in describing filtration processes [11]. In the solution-diffusion model, permeation is described as a three stage process

consisting of absorption, diffusion through the bulk driven by a concentration gradient, and desorption. Gas molecules still exist in pores, but the pockets of free volume are treated as temporary statistical fluctuations. For the dense, amorphous polymer systems considered in this work, this model is more appropriate, since the surface tension required to sustain multiple pores in this compressive elastic medium is prohibitively high [8].

The solution-diffusion model can be derived with a thermodynamic model and some simplifying assumptions. The flux of molecules, $\vec{J}$, at a point $\vec{r}$ is defined as

$$\vec{J}(\vec{r}) = c(\vec{r})\,\vec{v}(\vec{r})\,, \tag{3.1}$$

where c is the local concentration and $\vec{v}$ is the average velocity. The molecules are driven by the gradient in chemical potential, $\nabla\mu(\vec{r})$, at a rate proportional to their mobility, L:

$$\vec{v}(\vec{r}) = -L\,\nabla\mu(\vec{r})\,, \tag{3.2}$$

$$\vec{J}(\vec{r}) = -L\,c(\vec{r})\,\nabla\mu(\vec{r})\,. \tag{3.3}$$

From the Einstein relation [88], the mobility can be identified with the diffusivity, D, as

$$L = \frac{D}{RT}\,, \tag{3.4}$$

and therefore the flux can be written as

$$\vec{J}(\vec{r}) = -\frac{D}{RT}\,c(\vec{r})\,\nabla\mu(\vec{r})\,. \tag{3.5}$$

This is the general form of Fick's first law [89].

The chemical potential of an ideal gas at a concentration c is

$$\mu(\vec{r}) = \mu_{\circ} + RT\,\ln c(\vec{r})\,, \tag{3.6}$$

where $\mu_{\circ}$ is the reference chemical potential, usually taken at standard temperature and pressure (STP), and R is the molar gas constant. Deviations from ideal behaviour are ex-

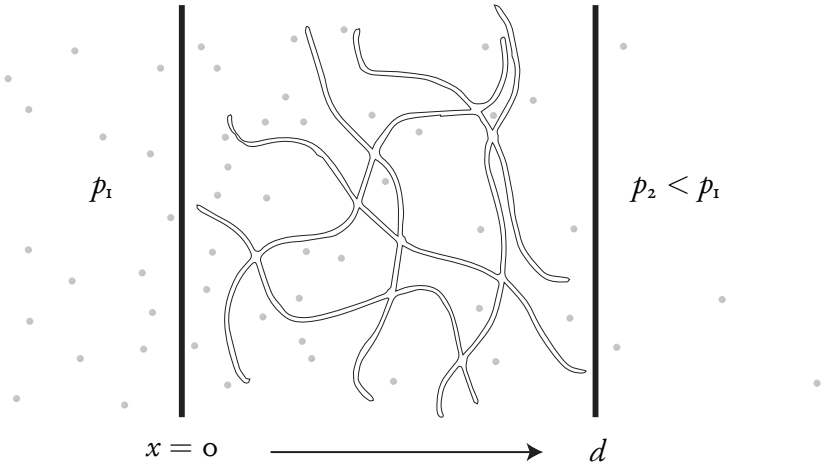


Figure 3.1: Permeation of gas across a membrane of width d. The pressure is maintained at p_1 at the feed side, and $p_2 < p_1$ at the permeate side.

pressed with the addition of a term dependent on $\gamma(c)$, the activity coefficient:

$$\mu(r) = \mu_\circ + RT \ln c(\vec{r}) + RT \ln \gamma(c)\,, \tag{3.7}$$

$$= \mu_\circ + RT \ln a(c)\,, \tag{3.8}$$

where $a = \gamma(c)\, c(\vec{r})$ is known as the activity (or fugacity). Combining this with Eqn. (3.5), the flux is now

$$\vec{J}(\vec{r}) = -\frac{D}{RT} c(\vec{r}) \nabla \left[\mu_\circ + RT \ln c(\vec{r}) + RT \ln \gamma(c)\right] \tag{3.9}$$

$$= -D\, c(\vec{r}) \left[\frac{\nabla c(\vec{r})}{c(\vec{r})} + \frac{\nabla \gamma(c)}{\gamma(c)}\right]\,. \tag{3.10}$$

When γ is independent of c, as is the case for an ideal solution, where $\gamma = 1$, and also for a dilute solution, where γ is constant, this simplifies to

$$J(\vec{r}) = -D \nabla c\,. \tag{3.11}$$

This is the more common form of Fick's first law.

Eqn. (3.11) can now be applied to the specific problem of permeation across a homogeneous membrane in the x direction. The membrane is in contact with a gas at partial pressure p_1 (concentration c_1) at the feed side, $x = 0$, and partial pressure $p_2 < p_1$ (concentration $c_2 < c_1$) at the permeate side, $x = d$, as shown in Figure 3.1. Using Eqn. (3.11) and assuming that the flux is constant in time, such that $\frac{d^2c}{dx^2} = 0$:

$$\vec{J}(\vec{r}) = J(x) = -D\frac{dc(x)}{dx}\,, \tag{3.12}$$

$$= -D\frac{c(x=d) - c(x=0)}{d}\,. \tag{3.13}$$

Assuming that the gas is ideal, the chemical potential outside the membrane is constant and can be written as

$$\mu_{\text{gas}} = \mu_0 + RT\ln c\,. \tag{3.14}$$

The chemical potential inside the membrane, μ_{membrane}, is written in terms of the position dependent concentration and an excess term, μ_{ex},* which represents the difference in chemical potential of the dissolved gas with respect to the pure gas state:

$$\mu_{\text{membrane}}(x) = \mu_0 + RT\ln c(x) + \mu_{\text{ex}}(x)\,. \tag{3.15}$$

The excess chemical potential effectively describes the free energy gained or lost per molecule, due to being in solution.

At both interfaces, $x = 0$ and $x = d$, it is assumed that the gas is in equilibrium. This means that μ is continuous. It is also assumed that the membrane is homogeneous, so μ_{ex} is

*A term which is related to the activity coefficient, γ, by $\mu_{\text{ex}} = RT\ln\gamma$

constant, and thus

$$\mu_\circ + RT \ln c_1 = \mu_\circ + RT \ln c(x = 0) + \mu_{ex} \,, \tag{3.16}$$

$$\mu_\circ + RT \ln c_2 = \mu_\circ + RT \ln c(x = d) + \mu_{ex} \,, \tag{3.17}$$

$$\Rightarrow c(x = 0) = c_1 \exp(-\mu_{ex}/RT) \tag{3.18}$$

$$\Rightarrow c(x = d) = c_2 \exp(-\mu_{ex}/RT) \,. \tag{3.19}$$

These last two equations are effectively statements of Henry's law [12], which states that in equilibrium the concentration of an ideal gas in a dilute solution is proportional to the concentration/partial pressure of gas above the solution. Combining this with Eqn. (3.13), the flux can be written as

$$J = -D \exp(-\mu_{ex}/RT) \left(\frac{c_2 - c_1}{d} \right) \,, \tag{3.20}$$

$$= -Ds \frac{\Delta c}{d} \,, \tag{3.21}$$

where the dimensionless solubility $s = \exp(-\mu_{ex}/RT)$ and $\Delta c = c_2 - c_1$. The flux, J, has the dimensions of quantity of molecules, which is dimensionless, per unit area per second. Experimentally, however, the quantity of gas molecules is usually expressed as the volume that the gas would take up at standard temperature $T_\circ$ and pressure $p_\circ$ if it were ideal. Therefore, using the ideal gas law $pV = nRT$, where n is the number of moles of gas, the flux usually measured in experiment is

$$J_{\text{experimental}} = J \cdot \frac{RT_\circ}{p_\circ} \,, \tag{3.22}$$

$$= -Ds \frac{\Delta c}{d} \cdot \frac{RT_\circ}{p_\circ} \,, \tag{3.23}$$

$$= -\frac{Ds}{d} \cdot \frac{\Delta p}{RT} \cdot \frac{RT_\circ}{p_\circ} \,, \tag{3.24}$$

$$= -D \left(\frac{T_\circ}{p_\circ T} s \right) \cdot \frac{\Delta p}{d} \,, \tag{3.25}$$

$$= -DS \frac{\Delta p}{d} \,, \tag{3.26}$$

where $\Delta p = p_2 - p_1 = \Delta c\, RT$ and the experimental solubility is given by $S = \frac{T_0}{P_0 T} s$, which is the volume of gas at STP dissolved per unit volume of solvent, per unit of absolute pressure. The diffusivity and solubility can be combined such that the flux becomes:

$$J_{\text{experimental}} = -P\frac{\Delta p}{d}\,, \tag{3.27}$$

in terms of the permeability, P, i.e.,

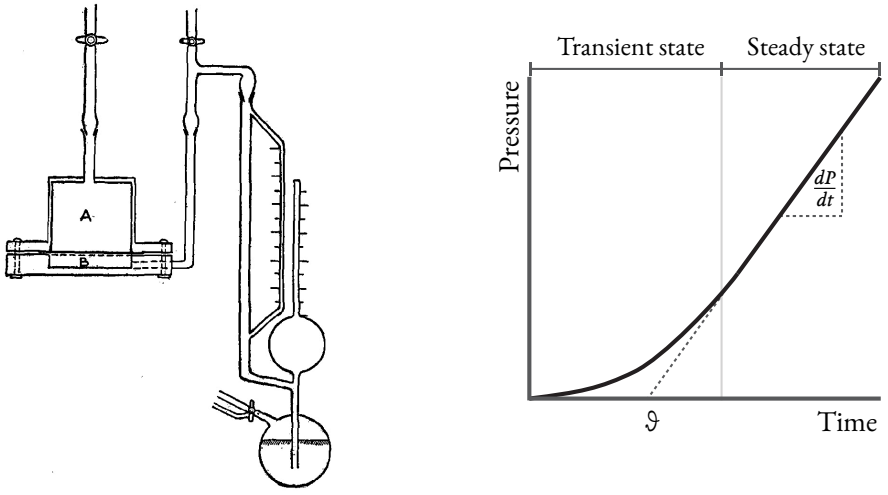
$$P = DS\,. \tag{3.28}$$

This equation encapsulates the solution-diffusion model.

3.2 Experiment

One of the first methods for measuring permeation rates through rubber was to fill a small balloon with a particular gas, and measure the rate of collapse of the balloon in air [87]. A breakthrough came in 1866 from Graham [90], who developed a device with two chambers separated by a rubber membrane, the first of which contained the test gas, while the second was evacuated and connected to a column of mercury. Gases permeating through the membrane would cause the mercury to be displaced, allowing the pressure to be measured. This apparatus is known as a permeation cell (Figure 3.2a), and is still in use today. While Graham used the device to measure steady state permeation rates, it was Daynes [91] who realised that the same equipment could be used to determine the diffusivity as well, by considering the time taken to reach the steady state. This time-lag (Figure 3.2b) is inversely proportional to the diffusivity, while the rate of change of pressure in the steady state is proportional to the permeability. The solubility is then inferred via the solution-diffusion model as the ratio of the permeability to the diffusivity. Direct measurement of solubility is also possible by observing the volume of gas absorbed by small samples of rubber (Figure 3.3), with Van Amerongen [71, 92] finding agreement to within 5 % between the two methods across a range of gases and polymers.

Barrer [93] was the first to study the permeability of gases in NBR, finding that the permeability of N_2 and H_2 increased with temperature. Van Amerongen [71, 92] later ex-



(a) Permeation cell

(b) Measuring permeability and diffusivity

Figure 3.2: (a) Two chambers, A and B, are separated from one another by a sheet of rubber. B is evacuated and connected to a mercury pressure gauge, and the test gas is pumped into A. (b) As the gas permeates from A to B, the pressure increases. The transient in the pressure can be used to measure the diffusivity, which is inversely proportional to the the time-lag, ϑ. The slope of the steady state part of the curve, $\frac{dP}{dt}$, is proportional to the permeability. The solubility can then be inferred from the ratio of the measurements via the solution-diffusion model. Permeation cell diagram reproduced with permission from Van Amerongen [92].

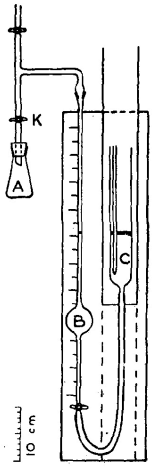


Figure 3.3: Direct measurement of solubility. Small samples of the elastomer are placed in flask A, which is initially evacuated. A controlled amount of test gas is pumped in, and allowed to saturate the rubber. The volume of gas remaining in the tubes is measured, and the volume absorbed by the material is deduced. Diagram reproduced with permission from Van Amerongen [92].

panded this to consider NBR samples of differing ACN content, to test more gases (O_2, CO_2, CH_4, He, NH_3 and SO_2), and to look at diffusivities and solubilities too.* Among the gases investigated, CO_2 was found to have the highest permeability.† While the diffusivity is correlated with molecular size and follows the order one might expect of $D(\mathrm{He}) > D(H_2) > D(O_2) > D(CO_2)$, it is the enhanced solubility of CO_2 as compared with other gases that leads to its relatively high permeability. Van Amerongen attributed this enhanced absorption to the electrostatic interaction between CO_2 and NBR. To investigate this behaviour further, I employ molecular simulation.

3.3 Molecular simulation

Molecular simulation is widely used to model the permeation of gases through polymers. In the membrane community it is an invaluable tool for characterising the relative permeability of two gases, known as the selectivity, in materials used for separation purposes. Simulation is useful for quickly screening potential materials, prior to testing in the lab. It is also able to reveal insights in situations that macroscopic experiments cannot, e.g., showing how the solution-diffusion model breaks down in lipid membranes due to the inhomogeneity of the bilayer [94].

Simulating the experimental procedure used by Van Amerongen directly is impractical due to the time- and length-scales involved.‡ As an alternative, the use of periodic boundary conditions enables the equilibrium diffusivities and solubilities of gases in the bulk environment of the polymer to be calculated. The permeability is then inferred from the solution-diffusion model.

3.3.1 Solubility

As discussed in section 3.1, the solubility can be expressed in terms of the excess chemical potential, μ_{ex}. In the 1960s, Widom [95] devised a method for computing μ_{ex} through sim-

*Diffusivities, solubilities and permeabilities were not measured for every combination of gas and rubber.

†Double that of He in NBR of 27 % ACN content, for example.

‡For example, from the experimental diffusivity of CO_2 in NBR, the distance a CO_2 molecule traverses in a second can be estimated as approximately 10 μm. Extrapolating linearly from the scaling of my simulations (a generous assumption), this would take about 200 million years to compute on current hardware.

ulation. First, consider the chemical potential of N identical gas molecules, μ, defined in terms of the Helmholtz free energy, $F(N, V, T)$, as

$$\mu = \left(\frac{\partial F}{\partial N}\right)_{V,T} . \tag{3.29}$$

The free energy can be written in terms of the partition function, $Q(N, V, T)$, as

$$F = -k_B T \ln Q(N, V, T) . \tag{3.30}$$

In the limit of large N, the chemical potential can be written as

$$\mu = \frac{F(N+1, V, T) - F(N, V, T)}{(N+1) - N} = F(N+1, V, T) - F(N, V, T) , \tag{3.31}$$

$$= -k_B T \ln \left(\frac{Q(N+1, V, T)}{Q(N, V, T)}\right) . \tag{3.32}$$

The canonical partition function is

$$Q(N, V, T) = \frac{1}{N! \Lambda^{3N}} \int_V \dots \int_V \exp\left[-U(r^N)/k_B T\right] \, dr^N , \tag{3.33}$$

$$= \frac{V^N}{N! \Lambda^{3N}} \int_0^1 \dots \int_0^1 \exp\left[-U(\tau^N, L)/k_B T\right] \, d\tau^N , \tag{3.34}$$

where Λ is the de Broglie wavelength, $U(r^N)$ is the intermolecular potential energy as a function of the positions of the atoms, and in Eqn. (3.34) the positions are expressed in terms of scaled co-ordinates τ, for atoms inside a cubic box of length L. The chemical potential is therefore

$$\mu = -k_B T \ln \left[\frac{V}{\Lambda^3 (N+1)}\right] - k_B T \ln \left\{ \frac{\int_0^1 \exp\left[-U(\tau^{N+1}, L)/k_B T\right] \, d\tau^{N+1}}{\int_0^1 \exp\left[-U(\tau^N, L)/k_B T\right] \, d\tau^N} \right\} \tag{3.35}$$

where the first term corresponds to the chemical potential of an ideal gas [96], and the second corresponds to the excess chemical potential, μ_{ex}. The energy, U, can be split into the

energy of the N particle system and the energy, ΔU_i, between this system and the extra particle i:

$$U(\tau^{N+1}, L) = U(\tau^N, L) + \Delta U_i \,. \tag{3.36}$$

The excess chemical potential can therefore be written as [97]

$$\mu_{ex} = -k_B T \ln\langle \exp(-\Delta U_i / k_B T)\rangle \,, \tag{3.37}$$

where $\langle \ldots \rangle$ denotes an ensemble average over the configuration space. Eqn. (3.37) is computed in simulation by randomly choosing a trial position for a molecule, inserting it, calculating the change in energy and the corresponding Boltzmann factor, removing the particle, and then repeating this process. The excess chemical potential here is defined in the dilute limit, i.e., such that there are no gas-gas interactions inside the polymer, and, as shown in section 3.1, is directly related to the solubility s:

$$s = \exp(-\mu_{ex}/k_B T) = \langle \exp(-\Delta U_i / k_B T)\rangle \,. \tag{3.38}$$

One issue with Widom insertion is that, since the insertions are performed randomly, there is a high probability of atomic overlap between solute and host. Due to Pauli repulsion this results in a large, positive ΔU, leading to the majority of insertions contributing a negligible amount to the solubility. Care therefore has to be taken to ensure adequate sampling, particularly at high polymer densities. An approach to alleviating this sampling problem is to use biased insertion techniques such as excluded volume map sampling [98], in which regions of free volume are first identified into which gas molecules are then inserted. This bias is then corrected for when computing the ensemble average in Eqns. (3.37) and (3.38) by multiplying the computed solubility by the fractional free volume [99]. As the fractional free volume is small in dense amorphous polymer systems,* this can result in a significant speed-up. However, since insertions can take place only in the sites predetermined to be free volume, this method is inherently sensitive to the manner in which the free volume is defined.

*Less than 3 % in NBR, for example, as I will show in chapter 5.

Another limitation of Widom insertion is that, since the polymer remains fixed while the rigid gas particles are randomly positioned and orientated, the efficacy of the technique is limited to small molecules for which the relaxation of both the polymer and inserted molecule are unimportant [100]. An approach to solving the polymer relaxation issue is to use simulations in a grand canonical Monte Carlo (GCMC) ensemble, i.e., under fixed temperature, volume and chemical potential [96]. In GCMC, steps of trial insertions and deletions of the rigid molecule are performed, interspersed with steps of dynamics to allow polymer and gas relaxation. The sorption isotherm can then be computed. To solve the relaxation issue for the inserted molecule, a configurationally biased Monte Carlo insertion procedure can be used [96]. In this method, the molecule is inserted one atom or monomer at a time, and a trial configuration is stochastically grown inside the solvent, and is then accepted or rejected depending on the degree of overlap. This is particularly important when considering long chain alkanes, for example, which otherwise would have a low chance of being successfully inserted. In this work I only consider insertion of small gas molecules, for which relaxation is not as important.

To my knowledge, Kucukpinar and Doruker [19] are the only other authors to have investigated gas solubility in NBR through simulation. They studied the solution of small gases (the largest being methane) in NBR with 39 % ACN content using a grid-based biased insertion technique and the COMPASS force-field [23]. While they were able to reproduce the ordering of solubilities found in experiment,* precise values were generally overestimated by up to a factor of 3.4. This overestimation of solubilities is found across the polymer simulation literature [101–104], and is usually attributed to unphysically large voids forming in the simulation cell or the sensitivity of the solubility to the force-field, which is heightened by the exponential factor in Eqn. (3.37).

3.3.2 Diffusivity

The motion of penetrants through dense amorphous polymers proceeds by two stages. Initially, the gas molecule is trapped inside one of the many small cavities in the polymer, forced to rattle around. These regions of free volume may fluctuate in size and shape, but

*$s(CO_2) > s(O_2) > s(N_2) > s(Ne) > s(He)$

are typically not connected. Occasionally, due to random fluctuations of the elastic matrix, a sufficiently wide channel will open up between two cavities and the molecule will be able to jump from one to the next. The channel closes behind the molecule, leading to the separation of the cavities once more, which is why this rattle and jump type motion has been dubbed the "Red Sea mechanism" of diffusion [100].

This behaviour can be observed and diffusion constants extracted using two main classes of molecular simulation methods: Monte Carlo and molecular dynamics (MD). In the Monte Carlo approach the positions of the polymer atoms are first discretised on a grid. The gas molecule of interest is placed on each grid point and the potential energy is computed. The energy landscape is mapped out, consisting of low energy sites that represent free volume, and high energy sites representing excluded volume. Transition pathways can thus be identified, with corresponding energy barriers and rate constants. Kinetic Monte Carlo simulations are then performed to generate thousands of trajectories, and the diffusivity can be computed in terms of the ensemble averaged mean squared displacement (MSD) as a function of time [88]:

$$D = \frac{\langle |\vec{R}_i(t) - \vec{R}_i(0)|^2 \rangle}{6t} \,, \tag{3.39}$$

where $\vec{R}_i(t)$ is the position of molecule i at time t, and the average is performed over all molecules and time origins.

This is an example of a transition state theory (TST) simulation, and has successfully been used to model diffusion through porous materials such as zeolites [105]. For polymers, however, this 'frozen polymer method' tends to underestimate diffusion coefficients since it inherently neglects any structural fluctuations in the medium [106, 107]. Other TST approaches include the 'average fluctuating polymer method' [106, 108] in which a smearing factor is added to the energy of the polymer sites, allowing them to harmonically oscillate about their initial positions. While this has the advantage of allowing a degree of polymer movement, the diffusivity is then sensitive to the parameter controlling the permissible degree of vibration, Δ.* If Δ is too small, the method is effectively the same as the frozen polymer method, and will underestimate the diffusivity. If it is too large, jumps become too

*Δ has units of length.

easy, and the diffusivity will be overestimated. Furthermore, Δ is sensitive to both the penetrant and the timescale of the simulation [106]. Because of these issues, a TST approach is not used in this thesis.

MD offers an alternative for computing diffusion coefficients. The trajectories of penetrants can be tracked inside a simulation cell filled with the amorphous polymer. The MSD can then be computed and related to the diffusivity, as in Eqn. (3.39), where the ensemble average is performed over multiple time origins to improve statistics. The diffusivity can also be computed from the velocity autocorrelation function:

$$D = \frac{1}{3} \int_0^\infty \langle \vec{v}_i(t)\, \vec{v}_i(0) \rangle \; dt \,, \tag{3.40}$$

where $\vec{v}_i$ is the velocity of particle i. This integral is only valid in the dilute limit,* and can be shown to be equal to Eqn. (3.39) in the long-time limit. This is an example of a Green-Kubo relation, a type of relation used across molecular simulation, e.g., the shear viscosity Green-Kubo relation involves computing the autocorrelation of components of the stress tensor [96].

Kucukpinar and Doruker [19] studied diffusion of small gases in NBR of fixed ACN content† in relatively small simulation cells.‡ Diffusivities were calculated using a fluctuating polymer TST method, and were inversely correlated with molecular size. Precise values were overestimated by up to a factor of 2.8. As with solubility, this overestimation of experimental diffusivities by atomistic simulations is consistently found across the literature (e.g., [110–113]). The fluctuations that open channels between cavities, thereby facilitating diffusion, are dependent on an atomistic level of precision in terms of describing the motion of the polymer. In contrast, the force-fields used to describe the interatomic interactions in the polymer, which I will discuss in chapter 4, are parameterised partly using simulations that seek to optimise the bulk properties such as the density. Reproducing macroscopic morphological properties using atomistic simulation is no guarantee of reproducing molecular transport properties. Nevertheless, simulation remains a powerful tool in pre-

*Otherwise cross-terms of the form $\langle \vec{v}_i(t)\, \vec{v}_j(0) \rangle$ between particles i and j have to be considered [109].

†39 %

‡They used a single 164 monomer-long chain, while the degree of polymerisation of NBR has been measured to be in the range of 400–20 000 monomers [2].

dicting and explaining trends in transport properties, providing a nanoscopic picture of the permeation process while offering a controlled and systematic way to vary the model parameters. Some of these parameters are difficult to control in experiment. For example, as discussed in section 2.3.1, when investigating seal failure it can be hard to replicate the high pressures and temperatures found downhole. Others are impossible to alter. For example, in chapter 5 I switch off the partial charges on the H_2O molecule, to illustrate the importance of electrostatics to the absorption of H_2O in NBR. Simulation therefore provides insight complementary to that attainable from experiment.

4

A molecular model for NBR

The morphological and transport properties of amorphous polymers such as NBR may be determined through molecular simulation. Before determining these properties a representative model must first be chosen; one that includes all the degrees of freedom required to enable the accurate computation of the desired properties, while minimising the computational cost. In this chapter, a molecular model for NBR is presented and, to demonstrate its validity, the model is used to compute bulk properties that are compared with experiment. The assumptions behind the model are explained, its strengths highlighted and its limitations evaluated.

4.1 Model

4.1.1 Intermolecular interactions

Ideally, a fully quantum-mechanical description of the polymer would be used to describe the intermolecular interactions, using a technique such as DFT to capture the full electronic structure of the system. DFT calculations have previously been performed on NBR [114, 115] to calculate the interaction energies between various hydrocarbons and chains up to

three monomers long. Extending such a calculation to, e.g., compute a density under ambient conditions, would prove impractical not least because of the computational costs but also because DFT struggles to describe the van der Waals interactions that hold the polymer together.*

Instead, an approximation to the quantum-mechanical interactions must be made, in the form of a force-field. Such a force-field can either describe the full atomic system, or use a level of coarse-graining to group atoms into 'super atoms', thereby reducing the computational cost of the simulation. Examples of coarse-graining used for polymers include the united-atom model that coarse-grains CH_n ($n = 1$ to 4) groups into single beads [116], and the Kremer-Grest bead-spring model which coarse-grains entire monomers, connecting them with non-Hookean springs [50, 117]. The latter of these two models is intrinsically accompanied by a complete loss in chemical specificity, rendering it difficult to compare computed properties of a given polymer that depend on an atomistic level of detail, such as gas permeabilities, to those found in experiment. The united-atom model, for example, has been shown to overestimate diffusivities with respect to fully atomistic models, which in turn overestimate diffusivities with respect to experiment [118]. Since transport properties are ultimately of interest in this work, a fully atomistic model is chosen.

The choice of precisely which fully atomistic force-field to use, i.e., the functional forms and parameters of the intermolecular interactions, is an important one. To the best of my knowledge, all previous MD simulations on NBR in the literature [19–22] have used the COMPASS force-field [23] as implemented in the commercial package, BIOVIA Materials Studio [24], widely used due to its vast range of parameterised molecules. However, this force-field is a proprietary one in that, while the functional forms used are freely available, the parameters are hidden, held in an encrypted database inaccessible to the end-user of the software.†‡ Using COMPASS therefore means being tied to using Materials Studio for all simulations, and while the documentation for the software cites the literature, the

*Although there has been much recent progress in the area, see, e.g., Refs. [13, 14] for a full discussion.

†There are multiple versions of the COMPASS force-field, and some of the oldest ones are, in fact, freely available in the literature. The latest and most parametrically complete versions are not, however.

‡It might be fair to ask if — setting aside the obvious licensing issues — such a force-field could be "reverse-engineered", e.g., by computing the energy required to stretch a given bond and fitting the parameters. However, the presence of cross-terms in the functional form, coupling different degrees of freedom, such as those between bonds and angles, and bonds and torsions, renders such an approach impractical.

precise algorithms it uses to, e.g., compute solubilities and diffusivities, are not detailed, which makes debugging any problem that might arise difficult. Similarly, it is not possible to modify the algorithms to tailor them to study a particular problem. Instead my preference was to use freely-available force-fields and open-source software wherever possible, leading to the choice of the OPLS-AA force-field of Jorgensen *et al.* [26]. Initially developed in the 1990s, this is a widely used force-field in the polymer simulation community due to its simplicity and parameter coverage for simple organic molecules.

While full details of the functional forms and parameters are provided in appendix A, in summary, the terms included in the OPLS force-field may be split into those governing the bonded and non-bonded interactions:

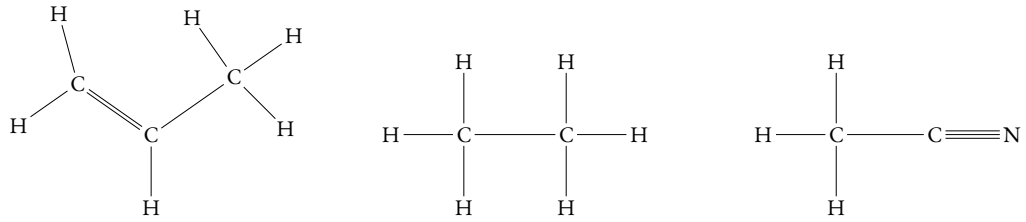
$$E = E_{\text{bonded}} + E_{\text{non-bonded}} \,, \tag{4.1}$$

$$E_{\text{bonded}} = E_{\text{bond}} + E_{\text{angle}} + E_{\text{dihedrals}} + E_{\text{impropers}} \,, \tag{4.2}$$

$$E_{\text{non-bonded}} = E_{\text{Lennard-Jones}} + E_{\text{Coulomb}} \,. \tag{4.3}$$

The bonded interactions are parameterised through DFT calculations on small molecules, i.e., for NBR, the parameters for butadiene come from propene and ethane, and for ACN they come from acetonitrile (shown in Figure 4.1). Small distortions are performed to these molecules to alter their bond lengths, bond angles and torsional angles, and the energy landscape is mapped. A simple harmonic form is used to describe the bond lengths and angles, while a fourth-order harmonic is used for the dihedral angles, and the parameters are fitted accordingly. The non-bonded terms — the Lennard-Jones (LJ) well depth and width, and the partial charges — are fitted by performing MD calculations of the molecule in the bulk, seeking to match experimental values for properties such as density and heat of vaporisation [26].

Since the bonded parameters used for NBR come from parameters generated by fitting to small molecules, certain dihedral parameters are not available in OPLS, namely a subset of those that describe the twist of three bonds spanning two monomers. The missing dihedral parameters, in terms of the bonded atom types as determined by their hybridisation, are shown in Table 4.1. Ideally, these parameters would be calculated by fitting to *ab initio* simulations, taking care to repeat the exact parameterisation process used in the



(a) Propene **(b)** Ethane **(c)** Acetonitrile

Figure 4.1: The small molecules that are parameterised in OPLS, from which the parameters for NBR are derived. Propene and ethane parameters are used for butadiene, ethane and acetonitrile parameters are used for ACN.

original work — the same DFT code with the same basis set etc. — to ensure consistency. This would be a lengthy procedure. The alternative is to perform a sensitivity analysis by varying the parameters and investigating the effect on, e.g., the density, to examine their importance. This is the approach used, and it was found that these missing parameters had a limited effect on the density. For example, a difference in density of less than 1 % was found when setting the missing $C(sp^2)-C(sp^3)-C(sp^3)-C(sp^2)$ dihedral parameters to be the same as the $C(sp^3)-C(sp^3)-C(sp^3)-C(sp^3)$ dihedral parameters, versus setting them to zero. Therefore the torsional twists were allowed to be free, i.e., the energy was set to zero for all angles.

4.1.2 Initial structure generation

Chains

To mimic the true microscopic structure of the polymer, the simulation cell should be filled with an array of chains whose lengths span the experimentally observed molecular-weight distribution for NBR, which is experimentally known to be 400 monomers to 20 000 monomers [2]. In practice, this is too computationally demanding. Previous NBR simulation studies [19–22] have not gone beyond 164 monomers. In this work a single chain of 1000 monomers was used, corresponding to approximately 9000 atoms (the precise number depends on the specified ACN content).*

*This was the maximum number of atoms it was possible to equilibrate within approximately 48 h on a dual socket Intel Xeon E5-2640 v2 workstation, using the procedure described in section 4.1.3.

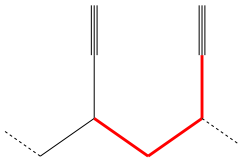
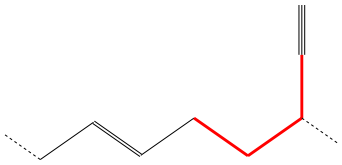
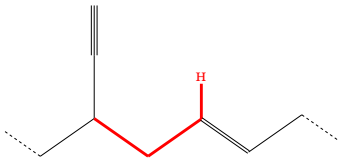
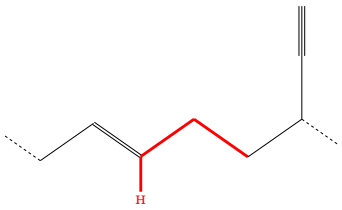
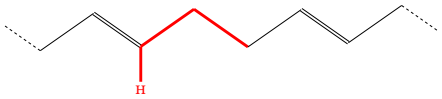
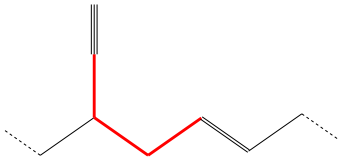
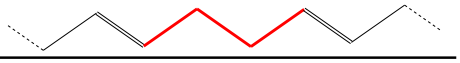
Dihedral	Monomers spanned	Chemical formula
$C(sp^3)-C(sp^3)-C(sp^3)-C(sp)$	ACN-ACN	
	BUT-ACN	
$C(sp^3)-C(sp^3)-C(sp^2)-H$	ACN-BUT	
	BUT-ACN	
	BUT-BUT	
$C(sp)-C(sp^3)-C(sp^3)-C(sp^2)$	ACN-BUT	
$C(sp^2)-C(sp^3)-C(sp^3)-C(sp^2)$	BUT-BUT	

Table 4.1: Missing NBR dihedral parameters in OPLS. Since OPLS was parameterised for the small molecules shown in Figure 4.1, the missing dihedrals span the two monomers, ACN and butadiene (BUT). In total, at most 5 % of the dihedral parameters for any given system are missing, and so it is unsurprising that they have a limited effect on the bulk properties.

As a statistical co-polymer of ACN and butadiene, the reactivity ratios were specified to stochastically generate the ordering of the monomers. Given a chain that is terminated (as denoted by *) in either A (ACN) or B (butadiene), the possible reactions, occurring at rates k, are [119]

$$A^* \xrightarrow{k_{AA}} AA^* \,, \tag{4.4}$$

$$A^* \xrightarrow{k_{AB}} AB^* \,, \tag{4.5}$$

$$B^* \xrightarrow{k_{BA}} BA^* \,, \tag{4.6}$$

$$B^* \xrightarrow{k_{BB}} BB^* \,, \tag{4.7}$$

where the reactivity ratios, r, may be defined as

$$r_A = \frac{k_{AA}}{k_{AB}} \,, \tag{4.8}$$

$$r_B = \frac{k_{BA}}{k_{BB}} \,. \tag{4.9}$$

In this study, values of 0.02 and 0.28 were used for r_A and r_B, respectively [17]. Given these reactivity ratios, and initial mole fractions of the monomers f_A and f_B pre-polymerisation, the mole fractions of the respective monomers in the structure generated post-polymerisation, F_A and F_B, can be estimated from the Mayo-Lewis equation [119]:

$$F_A = \frac{r_A f_A^2 + f_A f_B}{r_A f_A^2 + 2 f_A f_B + r_B f_B^2} \,, \tag{4.10}$$

$$= 1 - F_B \,. \tag{4.11}$$

Figure 4.2 shows the variation in ACN content in the polymer as a function of the initial ACN content, $F_A(f_a)$. With the sensitivity required in choosing the initial ACN content to generate NBR with higher than 50 % ACN content in the resultant polymer, this data suggests one reason such grades of NBR do not exist. The other issue is that with increasing ACN content, the elastic modulus of NBR increases, eventually ceasing to be useful as an elastomer at around 50 % ACN content [120].

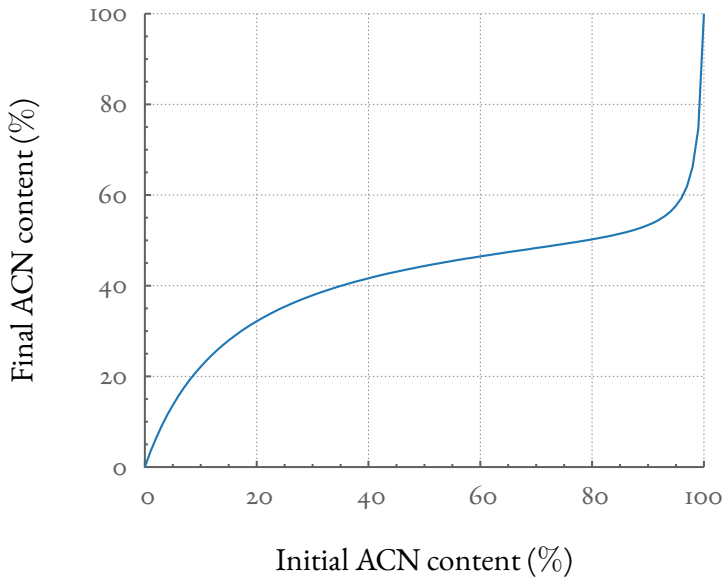
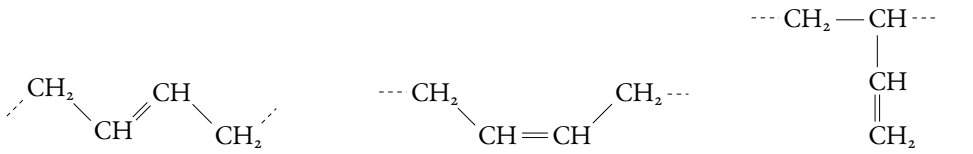


Figure 4.2: ACN monomer fraction pre- and post-polymerisation, based on the reactivity ratios of butadiene and ACN.

While NBR is composed of *vinyl*-butadiene, *cis*-butadiene and *trans*-butadiene, as shown in Figure 4.3, since the mole fractions of the *vinyl* and *cis* components are relatively small, they are ignored in this work.

Amorphous cell packing

When performing a MD simulation, one of the first steps is to choose the initial co-ordinates for the particles in the system. For simulations of liquids or short-chain polymers, this choice is relatively inconsequential as the fast relaxation times for these systems mean that



(a) *trans*-butadiene (90 %) **(b)** *cis*-butadiene (8 %) **(c)** *vinyl*-butadiene (2 %)

Figure 4.3: The different butadiene components that make up NBR and their relative mole fractions in NBR of 39 % ACN content [17]. With increasing ACN content the *cis* component becomes smaller, whilst the *vinyl* component is approximately constant [121].

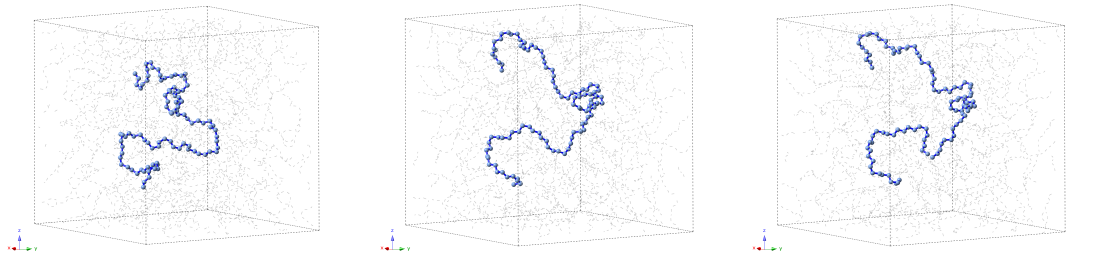
'memory' of the initial positions is quickly lost during a dynamical simulation, especially at high temperatures, which is why equilibration recipes often contain some form of annealing [122]. If there are no hard-sphere interactions the particles can be placed randomly as avoiding overlap is unnecessary, otherwise the simplest choice is to place them on a lattice [122]. For a long amorphous polymer such as NBR this choice is less trivial, partly because there is no obvious place to put every atom such that the resulting polymer is entangled.

A further issue is that the relaxation of long, entangled, polymers proceeds by reptation [123] — the snake like movement of the polymer along its own contour — which is a slow process that relies on the degrees of freedom at the chain ends, since the rest of the chain is entangled [47]. Subsequently, the polymer conformation is unlikely to substantially deviate from whatever initial configuration is chosen, through dynamics alone. An example demonstrating this may be found in Figure 4.4, in which a 100 bond segment of the backbone of an NBR chain is highlighted, showing its net movement after a 4 ns equilibration consisting of cycles of minimisation, annealing, compression and relaxation, and after a further 6.25 ns of fixed NPT dynamics at standard ambient temperature and pressure (SATP).* While the equilibration procedure does seem to accelerate the movement of the chain as compared with the fixed NPT dynamics, overall, the entangled nature of the polymer inhibits large conformational changes over the timescales studied, therefore any inhomogeneities such as voids present in the structure during the initial structure generation will typically not dissipate over an MD simulation. Hence, when using these structures to measure properties of the elastomer that are compared with experiment, it is important to use average results across an ensemble generated from many different initial configurations, especially for properties such as solubility that are sensitive to free volume [100].

The structures are generated by packing the 1000 monomer chain into a periodic cell, at a target density of 1000 kg m^{-3}, chosen to match the experimental density of NBR. The packing is performed using a procedure based on the rotational isomeric state method of Theodorou and Suter [124], as implemented in the Amorphous Cell routine of BIOVIA Materials Studio [24].† In this Monte Carlo routine, illustrated in Figure 4.5, one bond at

*25 °C and 100 kPa.

†v7.0



(a) Initial structure ($t = 0$) **(b)** Post equilibration ($t = 4$ ns) **(c)** Post NPT dynamics ($t = 10.25$ ns)

Figure 4.4: The movement of a selected fragment of 100 carbon atoms along the backbone of an NBR chain during an MD simulation. The equilibration procedure, described in more detail in section 4.1.3, consists of cycles of minimisation, annealing, compression and relaxation for 2.5 ns, ending with 1.5 ns of dynamics at SATP in an isothermal-isobaric ensemble (until $t = 4$ ns). Another 6.25 ns of NPT dynamics at SATP follows (until $t = 10.25$ ns). The segmental motion is highly inhibited over these timescales, due to the high degree of entanglement.

a time is placed while going along the backbone of the polymer, fixing bond lengths and angles due to their stiffness, but allowing the dihedral angles to vary, as these are responsible for the range of conformations that polymers can take up. At each step the change in interaction energy is computed using the COMPASS force-field,* and used to weight the choice of dihedral angle, resulting in a self-avoiding torsionally-biased random walk. This is repeated to generate different configurations. As an inherently probabilistic method, these configurations are effectively independent from one another on the timescale of an MD simulation. Each configuration is equilibrated (as described in the following section) before the morphological and transport properties of interest are computed.

*The OPLS force-field is not used since it is not included in Materials Studio, and it is not possible to implement it manually, since there is no option in the software to specify a force-field that weights the non-bonded interactions between atoms separated by 3 bonds by a factor of 0.5, as required by OPLS. Therefore a different force-field is used for the structure generation and for the dynamics. Care is required when switching between force-fields, since different force-fields may be parameterised differently and/or have different functional forms for the energy. Since the only degrees of freedom in the initial structure generation are the dihedral angles, whose parameters, in both OPLS and COMPASS, are derived through *ab initio* simulations from which qualitatively the same torsional energy landscape should be obtained for the same molecule, similar structures should be obtained independent of the precise force-field used.

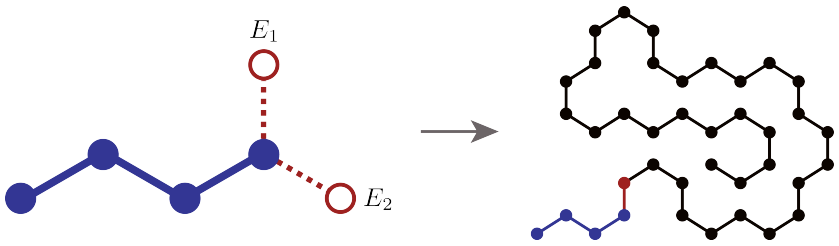


Figure 4.5: Packing of an amorphous polymer. The full polymer is mapped to a grid with only its backbone atoms. The first three bonds are placed randomly, and then the chain is grown one bond at a time by varying the dihedral angles while maintaining fixed bond lengths and angles. The energy cost of each configuration is computed using the COMPASS force-field, and then one is picked using a standard Metropolis-Hastings Monte Carlo selection criterion. Unlike a deterministic process, this means that the less energetically favourable configuration could be chosen. Once the chain is grown to the required length, it is mapped back to the fully atomistic picture.

4.1.3 Equilibration

While the Monte Carlo chain packing routine described previously provides a fast method for exploring the vast phase space of the possible polymer configurations, generating configurations that are far from each other on this hyper-dimensional energy-conformation landscape, equilibration is a way to explore the local phase space about each initial configuration. For each structure a combination of compression, relaxation, heating and cooling are used to overcome local energy barriers in search of lower energy minima, and, ultimately, more representative structures.

The equilibration procedure used is based on that of Kucukpinar and Doruker [19, 125] and their simulations on 164 monomer-long NBR, and is shown in Table 4.2. I have increased the duration of the equilibration as compared to the original method by over a factor of ten to reduce the spread of densities. All dynamical simulations in this work are performed in LAMMPS [126].*

4.1.4 Assumptions

Absence of cross-links

In practice, NBR chains are usually cross-linked either through an intermediary sulfur group using vulcanisation [3], or directly from one butadiene monomer to another through

*Version September 2014.

Time (ns)	Method	Temperature (°C)	Pressure (MPa)
-	Energy minimisation*	-	-
0–0.25	NPT compression	25	0.1–500
0.25–0.5	NPT relaxation	25	500–0.1
-	Energy minimisation*	-	-
0.5–1.0	NPT heating	25–525	0.1
1.0–1.5	NPT cooling	525–25	0.1
1.5–1.75	NPT compression	25	0.1–500
1.75–2.0	NPT relaxation	25	500–0.1
2.0–2.5	NVT	25	-
2.5–4	NPT	25	0.1

Table 4.2: Procedure used to equilibrate NBR configurations generated in Materials Studio. Any heating, cooling, compression or relaxation performed was done so at a constant rate: 1000 °C ns^{-1} and approximately 2000 MPa ns^{-1} for changes in temperature and pressure, respectively.

peroxide curing [64]. Such intermolecular (and intramolecular) bridges act to limit the long-range motion of the polymer chain segments, raising the glass transition temperature and increasing the stiffness of the material.

Cross-linking can be replicated through molecular simulation [128], by subjecting an uncrosslinked structure to a series of cross-linking steps, during which atoms of a type eligible for cross-linking based on their bonding are cross-linked using a distance criterion and the probability of cross-linking (i.e., the total cross-link fraction expected). In between each cross-linking step, an energy minimisation is performed followed by a short dynamical equilibration, in order to allow the polymer to relax and accommodate the new bonds. This method was used by, e.g., Arab *et al.* [129], who were able to reproduce the correct experimental glass transition temperature of thermoset epoxy polymers.

While a static variant of this model, in which all cross-linking is performed in one step before any relaxation occurs, was used by Molinari *et al.* [25] to model HNBR (discussed in more detail in chapter 7), for this NBR model no cross-linking was performed, since the exact cross-linking procedure used in NBR varies from one formulation to the other, e.g., vulcanisation versus peroxide curing, the speed of the process, the concentration of cross-

*Performed using the FIRE algorithm [127], until the energy of the system remained fixed to within 10^{-4} %, or after 50 000 steps, whichever occurs first.

links etc. Examining the effect of all of these variables was deemed to be beyond the scope of this work and thus the simplest approach was to use no cross-linking.

Absence of fillers

Filler particles such as carbon black and silica are used to tune the material properties of the polymer, such as the elastic and bulk moduli [2–4], and are a vital component of any commercial elastomer formulation. They typically come in different grades based on the tensile strength and abrasion resistance required for the specific application, which vary by particle size. Carbon black, for instance, consists of agglomerates of amorphous carbon that range in size from 20–350 nm.* This makes it difficult to study fillers using fully atomistic simulation. For example, to study a distribution of smaller filler particles interspersed with polymer might require a cubic simulation cell of length 100 nm, i.e., 20^3 times larger than my current system, corresponding to a simulation at least 20^3 times longer.†

An alternative is to use a coarse-grained model such as the bead-spring model of Kremer and Grest [50], which discretises multiple monomers into beads connected with finitely extensible non-linear springs, with an LJ potential between all beads. Filler particles can then be treated as single beads with larger masses and LJ radii than the polymer beads, and the filler-polymer interaction can be tuned to understand the effect of the chemical coupling between filler and rubber. This approach has been widely used to explore the effect of fillers on the material properties of polymers, e.g., to find the optimum filler fraction for reinforcement of elastomers [130].

However, such an approach intrinsically involves a complete loss in chemical specificity. Therefore, since the morphological and transport properties of NBR are of particular interest in this work, and there is a high degree of variation in the shapes, sizes and chemistry of filler particles, and a fully atomistic description of the filler particles and polymer would be too computationally demanding, they are not included in this model.

*Designations ASTM N110 and N990, respectively.

†A very generous estimate that assumes perfect scaling, and would lead to a simulation that would take about 3 years per nanosecond.

MD simulations face a constant battle to access longer time- and length-scales in order to improve their efficacy. Technological advancements in processing hardware have enabled the decomposition of particles across an increasing number of cores per node and an increasing number of nodes, leading to increasingly larger systems being studied.* These improvements typically hit a limit in the form of a minimum number of particles per core, before the communication between cores for particles crossing from the domain of one core to another negates the speed-up from dividing up the calculations of energies and forces amongst the cores. An example of this is shown in Figure 4.6, which shows the parallel efficiency, E_N, for an NBR simulation of 8763 atoms over N cores, defined as

$$E_N = \frac{1}{N}\frac{T_1}{T_N}\,, \tag{4.12}$$

where T_i is the time taken for a simulation over i cores. Beyond eight cores — approximately 1000 atoms per core — the efficiency drops off rapidly, with simulations using 128 cores being only about ten times shorter than those using a single core. To maximise throughput while completing each simulation within a reasonable time-frame, dynamics are performed using eight cores in this work.

Aside from increasing the clock speed of the processor to complete calculations faster, improvements to hardware have a limited effect on increasing accessible timescales. Instead, different underlying algorithms for the dynamics may be used. One option is to use an algorithm to constrain the fastest modes in the system — in this case the stretching of the C−H bond. The SHAKE algorithm [132] is widely used to remove this degree of freedom by first calculating the unconstrained velocities of the atoms in the bond, and then iteratively modifying them to meet the constraint. A longer timestep can therefore be used.

Another common choice is the rRESPA† method [133, 134], which takes advantage of the fact that not every term in the force-field needs to be computed at every timestep of the simulation. For example, the high frequency bond vibrations are calculated at every

*The record changes hands frequently, but currently stands at 10^{12} particles [131].

†Reversible reference system propagator algorithm.

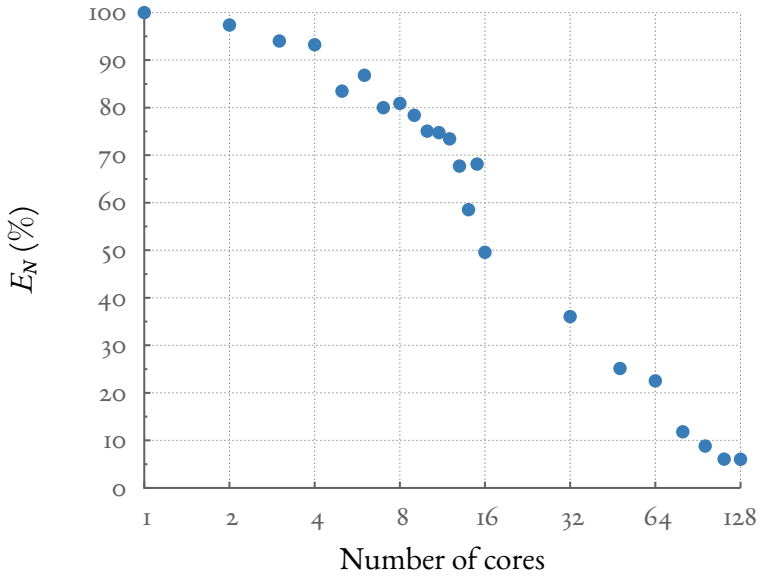


Figure 4.6: Parallel efficiency, E_N, of NBR simulations, as a function of the number of cores, N. For each N, three different equilibrated NBR structures of 41.3 % ACN content with 8763 atoms are simulated for 1 ps, using a timestep of 1 fs, and the CPU times are averaged before the efficiency is calculated. There are 16 cores per node, with an InfiniBand interconnect to minimise inter-node communication time.

timestep, but non-bonded terms do not change so rapidly and are expensive to calculate,* so can be computed every few timesteps.

Table 4.3 shows the relative speed-up obtained when using no optimisations, SHAKE, or rRESPA, as well as the percentage energy drift in each case. The best balance of minimising energy drift while maximising speed-up was obtained when using SHAKE and a timestep of 2.5 fs, therefore this combination was used in all simulations.†

4.3 Bulk property results

To demonstrate the transferability of the OPLS force-field and its applicability to NBR, a series of bulk properties are computed and compared to experiment.

4.3.1 Density

The average density as a function of ACN content, at SATP, over eight independently generated and equilibrated configurations per sample of NBR at a given ACN content, is shown in Figure 4.7. For each configuration, the equilibrated structure was evolved for 1 ns at SATP using an NPT ensemble, and the instantaneous density recorded every 0.25 ps. The average density for each trajectory was then computed, and an average over all trajectories performed. The typical standard deviation was 0.5 %, showing close agreement between the structures.

The experimental trend of increasing density with increasing ACN content is reproduced. The qualitative agreement is also reasonable — the largest difference is the underestimation of the density of amorphous polyacrylonitrile by 5 %. It is worth noting that

*There are a number of reasons for this computational expense. One factor is that there are simply more non-bonded interactions to compute than bonded ones. Keeping track of atoms within the neighbourhood of one another is also computationally expensive. This is done so that short-ranged interactions (e.g., LJ) are not computed between atoms that are far apart, for which the interaction energy would be negligible. Another issue is the time required to compute the long-ranged part of the Coulombic interaction, which is commonly calculated with an Ewald summation [135], requiring the extensive use of computationally intensive Fourier transforms. On average in my simulations, the non-bonded part of the dynamics represents approximately 80 % of the computation time.

†Except for during the annealing, where a timestep of 1 fs was used and no constraints were applied, as the system was otherwise unstable.

Modification	Timestep (fs)	Energy drift (% ns^{-1})	Relative speed-up
None	1.0	0.0009	-
	1.5	0.02	1.4
	2.0	0.03	1.9
	2.5	20	2.3
SHAKE	1.0	0.002	1.0
	1.5	0.01	1.4
	2.0	0.007	1.8
	2.5	0.006	2.3
	3.0	0.6	2.7
rRESPA	1.0	0.001	0.3
	1.5	0.007	0.5
	2.0	0.004	0.6
	2.5	0.02	0.8
	3.0	0.002	0.9
	3.5	0.003	1.0

Table 4.3: Comparison between different attempts to increase the speed of simulations, in terms of the absolute percentage energy drift per nanosecond and the relative speed-up compared to using no constraints and a timestep of 1.0 fs in terms of CPU time per nanosecond of simulation time. All values are averaged from three dynamics runs over different, equilibrated, starting configurations, performed over 1 ns. The SHAKE simulations became unstable for timesteps $\geq$ 3.5 fs, but up to 2.5 fs an acceptable energy drift and speed-up was obtained. The relative speed-up is lower than the relative increase in timestep, due to the overhead required in solving the SHAKE constraint equations. The rRESPA calculations were split up into two levels based on the timestep Δt — bonded forces (bonds, angles, dihedrals) were calculated every $\Delta t/8$, whereas non-bonded forces (LJ and electrostatics) were computed every Δt. The overhead in computing the former terms prevented any speed-up, and it was not possible to test a timestep of 4.0 fs or higher without the system becoming unstable. System instability also prevented the use of a larger interval for computing bonded terms, e.g., $\Delta t/4$, as well as the use of a combination of SHAKE and rRESPA.

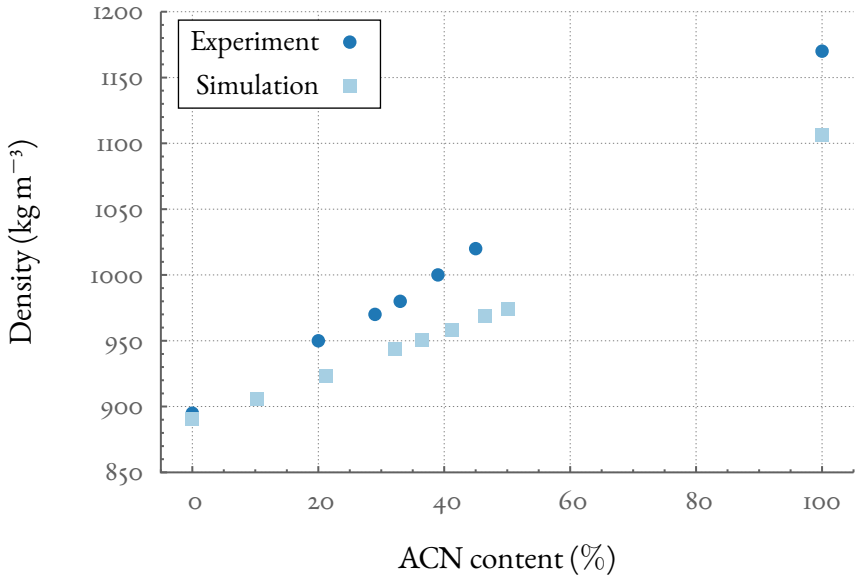


Figure 4.7: Density as a function of ACN content from simulation and experiment. Standard deviation of average densities is less than 0.5 %. Experimental data from Roff and Scott [2] and Klingender *et al.* [1].

the discrepancy between the simulated and experimental density grows larger with increasing ACN content. This may be due to the fact that the OPLS force-field parameters used for the ACN monomers were in fact parameterised for acetonitrile — a small molecule that forms a liquid at ambient conditions. To test this, a simulation of bulk acetonitrile was performed over 2 ns, including cycles of minimisation, compression, relaxation and annealing, to establish its bulk density, and the simulated value was found to agree with the experimental one to within 1 %. Despite this close agreement for acetonitrile, these results suggest that simply using acetonitrile as a building block for ACN, and ultimately polyacrylonitrile, does not guarantee agreement with the experimental density of polyacrylonitrile. Ideally, parameters would be derived for polyacrylonitrile, but such an effort might not even result in a unique set of coefficients* and was deemed to be beyond the scope of this work. Instead, a sensitivity analysis was performed to understand the source of the error, varying different parameters such as the partial charges of certain sites, the strength and range

*For example, the crystalline and amorphous forms of polyacrylonitrile would likely require different sets of parameters.

of the LJ interactions, or the dihedral parameters, before performing an equilibration and computing the density. The biggest reduction in the discrepancy was observed when using the dihedral parameters from the PCFF+ force-field as implemented in Materials Design's MedeA [136, 137],* which reduced the underestimation of the density to 3.5 %.†

It is also possible to compare to other force-fields used in the literature; Kucukpinar and Doruker [19] previously studied 168 monomer-long NBR of 39 % ACN content through simulation using COMPASS, and obtained a density of 977 kg m^{-3}, 2 % higher than the simulated density of NBR of 41.3 % ACN content using OPLS, suggesting that the COMPASS parameters for NBR are slightly better tuned than the OPLS ones.

Another factor in the discrepancy in the density might be cross-linking, as it is unclear whether the experimental data is derived from samples that were cured. Vulcanisation of the simulated structures should increase the density, as the intra-chain separation would decrease. The intra-chain separation of the uncured structures can be estimated from the minimum of the LJ potential between backbone carbon atoms on adjacent chains, which in OPLS is approximately 0.39 nm [26]. In contrast, the experimentally measured length of the carbon-sulfur bond found in vulcanised rubber is 0.1759 nm [138], resulting in a chain separation of two C—S bonds of approximately 0.35 nm for cross-linked NBR (a difference of approximately 10 %).

4.3.2 Bulk modulus

The bulk modulus, or isothermal compressibility, of a material is a measure of its volumetric response to pressure. Elastomers are often treated as incompressible, with a Poisson's ratio of 0.5 [139], which is a good approximation at atmospheric pressures and temperatures.‡ However, especially at the high pressures found down-hole, their compressibility can become a factor, e.g., when a seal needs to sit in a metallic groove of fixed volume.

To compute the bulk modulus through simulation, equilibrated structures were taken and squeezed in an NPT ensemble from 0–1000 MPa. This was done by raising the pres-

*v2.16

†Incidentally, the same reduction was also observed when testing the effect of switching off all dihedrals entirely.

‡With a typical bulk modulus of 2 GPa [139], the density of an elastomer changes by 0.02 % every 0.1 MPa.

sure at a constant rate by 20 MPa over 100 ps, followed by fixing the pressure for 200 ps, using the last 100 ps to record the cell volume every 0.25 ps a total of 400 times, from which an average and standard deviation were extracted. This process was repeated until the maximum pressure was reached, and the entire procedure was performed on a total of eight independently generated and equilibrated configurations to obtain good statistics.

The bulk modulus may be obtained from the resulting $P(V)$ data by the fitting of an equation of state, such as that of Birch-Murnaghan [140, 141], which defines the pressure, P, at volume, V, with a reference volume, V_0, as

$$P(V) = \frac{3B_0}{2}\left[\left(\frac{V_0}{V}\right)^{\frac{7}{3}} - \left(\frac{V_0}{V}\right)^{\frac{5}{3}}\right]\left\{1 + \frac{3}{4}\left(B_0' - 4\right)\left[\left(\frac{V_0}{V}\right)^{\frac{2}{3}} - 1\right]\right\}, \tag{4.13}$$

where B_0 is the bulk modulus and B_0' is its derivative with respect to pressure, both defined at zero pressure:

$$B_0 = -V_0\left(\frac{\partial P}{\partial V}\right)_T, \tag{4.14}$$

$$B_0' = \left(\frac{\partial B}{\partial P}\right)_T. \tag{4.15}$$

An example of a set of $P(V)$ data and the resulting fit is shown in Figure 4.8.

This procedure was repeated for NBR of varying ACN content, and the results are shown in Figure 4.9. With increasing ACN content the bulk modulus increases, which correlates with the experimental observation that the hardness and stiffness of NBR increase with ACN content [120], until it eventually ceases to become useful as an elastomer beyond 50 % ACN content. Furthermore, polyacrylonitrile is known to be a semi-crystalline polymer whilst polybutadiene is not, therefore with increasing ACN content an increasing degree of crystallinity and hence, incompressibility, would be expected.

The bulk modulus of NBR of any ACN content was not found in the literature, therefore a direct comparison to experiment is not possible, however, based on the typical moduli of similar thermoset elastomers, the value is expected to lie in the range of 1000 MPa to 2000 MPa [139]. Hence, the simulation results obtained are overestimated with respect to

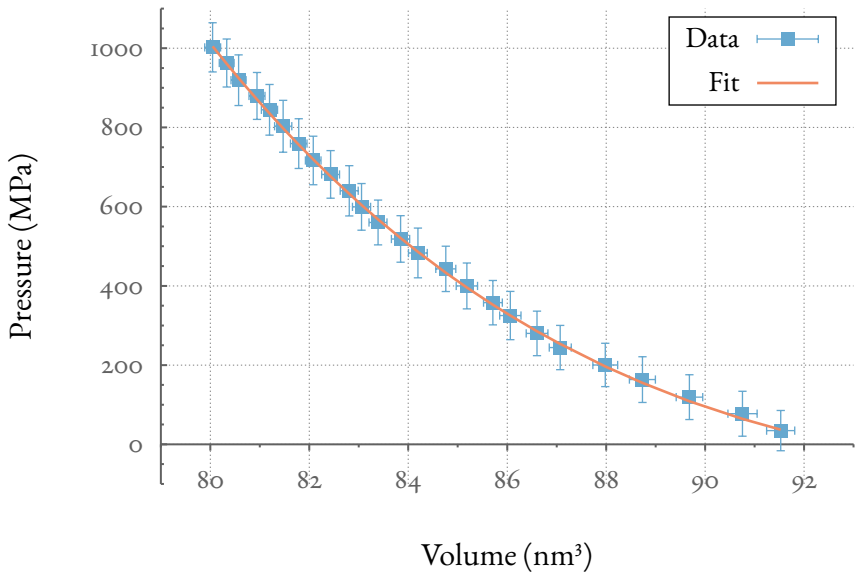


Figure 4.8: A pressure-volume curve obtained from gradually squeezing NBR of 41.3 % ACN content in steps of 20 MPa over 100 ps. The error bars represent the standard deviation in the fluctuating volume and pressure. For the sake of clarity, only 25 of the 50 points are shown. The Birch-Murnaghan equation of state is fitted to the data, and shows close agreement.

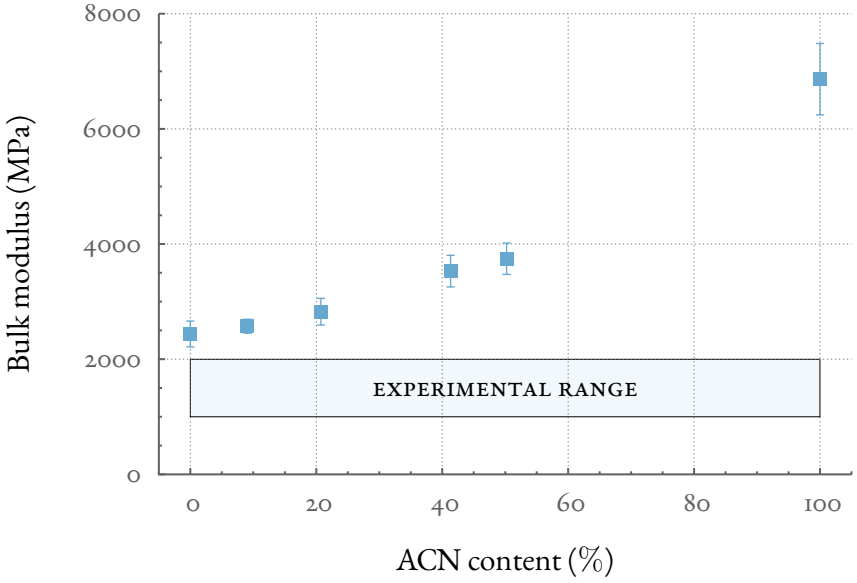


Figure 4.9: Bulk modulus of NBR as a function of ACN content, obtained from fitting $P(V)$ data to the Birch-Murnaghan equation of state. error bars represent the standard deviation in the average modulus, computed over eight independently generated configurations.

experiment. One factor is the dependence of the bulk modulus on the strain-rate. The relaxation of long, amorphous polymers is limited by entanglement, and primarily proceeds through reptation, a relatively slow process in comparison to the nanosecond MD simulations performed in this work [123] Therefore the degree of relaxation possible will depend on the time allowed for relaxation. To test the effect of strain-rate, a 400 % higher strain-rate was used on NBR of 41.3 % ACN content, and found to increase the bulk modulus by 40 %. In contrast, using a 50 % lower strain-rate reduced the bulk modulus by 3 % — a statistically insignificant difference. While these results do not rule out the possibility of strain-rate related issues, they do suggest that moving towards a more realistic strain-rate while still bound by the computational limitations of molecular simulation will yield diminishing returns. Instead, it is better to focus on the qualitative trends in these results, rather than to seek precise quantitative agreement with experiment.

4.3.3 Glass transition temperature

An important property of polymers is their glass transition temperature, T_g, defined as the temperature above which the material softens due to the beginning of long-range co-ordinated motion of molecules. Below T_g, an amorphous polymer will be hard and brittle, as the molecular motion is restricted to short range thermal vibrations. Above T_g, the polymer chains are able to flow along their own contours via reptation. It is subsequently a key property, as for most industrial applications it is necessary to ensure the polymer remains rubbery over the range of service conditions, and thus a wealth of experimental data exists for the purposes of validating the model developed in this chapter.

In simulation, T_g can be identified as a discontinuity in the gradient of the cell volume as a function of temperature. The procedure used to compute it in this work is as follows. Starting with an equilibrated structure at 140 °C,* the temperature is gradually lowered, the system is allowed to relax, and the average volume is computed as a function of temperature. During each step, 0.25 ns is spent lowering the temperature at a constant rate by 15 °C, 0.25 ns is spent at the lower temperature to allow the polymer to relax, followed by a production run of 1.5 ns during which the volume is recorded every 0.25 ps before being averaged. This process continues until the temperature reaches −130 °C, and is repeated for eight independently generated and equilibrated structures of NBR with 41.3 % ACN content. The volume fluctuations obtained at a particular temperature (20 °C) for the eight structures are shown as an example in Figure 4.10, and generally exhibit a sharp drop off in the volume upon cooling, followed by a fluctuating volume for the remaining dynamics. This is consistent with other T_g simulations in the literature [142]. During the production run, the standard deviation of the volume fluctuations is less than 4 %.

*A structure generated and equilibrated at SATP following the procedure described earlier is heated from 25–140 °C over 2 ns at a constant rate, before being held at a fixed temperature of 140 °C for 0.25 ns. An NPT ensemble is used in both steps, with the pressure maintained at ambient levels, i.e., 0.1 MPa.

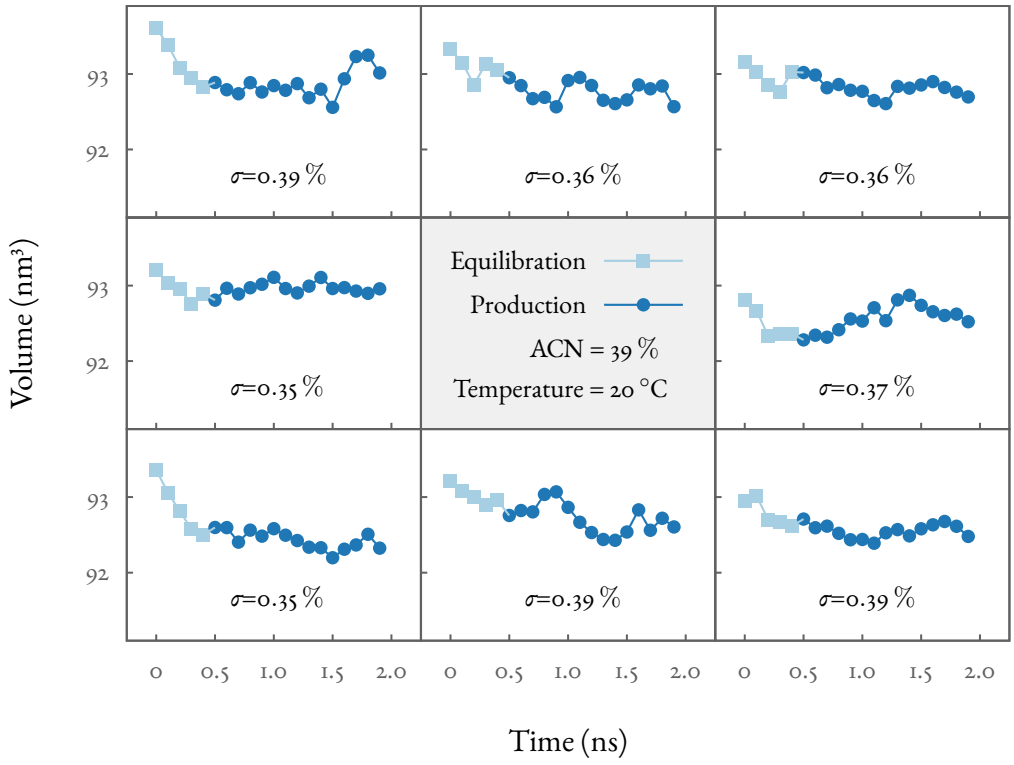


Figure 4.10: Fluctuations in the volume during equilibration and production runs, used to measure the average volume at 20 °C for eight independently generated and equilibrated NBR structures of 41.3 % ACN content. During the first 0.25 ns the systems are cooled from 35–20 °C at a constant rate, followed by a 0.25 ns equilibration and a 1.5 ns production run.

To extract the glass transition temperature from the $V(T)$ curves produced, the method of Simperler *et al.* [143] is followed, in which the data is divided into points representing either the glassy or rubbery polymer:

1. Starting from the average volume $V(T_i)$ at N different temperatures T_i, henceforth referred to as V_i, assume a points belong to the glassy region and $N-a$ to the rubbery region.

2. Calculate linear fits for both regions, with model values f_i^{g} for integer $i \in [1, a]$, and f_i^{r} for integer $i \in [a+1, N]$, where $a \in [3, N-3]$

3. Calculate the means in each region, $\overline{V}_{\mathrm{g}} = \frac{1}{a}\sum_{i=1}^{a} V_i$ and $\overline{V}_{\mathrm{r}} = \frac{1}{N-a}\sum_{i=a+1}^{N} V_i$.

4. Compute the associated R^2 values:

$$R^2_{\mathrm{g}} = 1 - \frac{\sum_{i=1}^{a}(V_i - f_i^{\mathrm{g}})^2}{\sum_{i=1}^{a}(V_i - \overline{V}_{\mathrm{g}})^2}, \tag{4.16}$$

$$R^2_{\mathrm{r}} = 1 - \frac{\sum_{i=a+1}^{N}(V_i - f_i^{\mathrm{r}})^2}{\sum_{i=a+1}^{N}(V_i - \overline{V}_{\mathrm{r}})^2} \tag{4.17}$$

5. Repeat the procedure for different values of a.

6. Pick the value of a that maximises $\sum R_i^2 = R^2_{\mathrm{g}} + R^2_{\mathrm{r}}$.*

The intersection of the two fits for the optimal choice of a then yields the glass transition temperature. Figure 4.11 shows an example of this procedure applied to a given set of $V(T)$

*A perfect fit would correspond to $\sum R_i^2 = 2.0$

data from NBR of 41.3 % ACN content, and the variation in $\sum R_i^2$ as a function of the maximum temperature of the glassy region.*

To investigate the effect of thermal hysteresis, the entire set of T_g simulations was repeated, this time *increasing* the temperature from −130 °C to 140 °C (rather than decreasing from 140 °C to −130 °C). Figure 4.12 shows that no sizeable hysteresis was observed.

The procedure outlined to calculate T_g was repeated for eight independently generated and equilibrated configurations, at each of seven different ACN percentages ranging from polybutadiene to polyacrylonitrile, to obtain the average glass transition temperature as a function of ACN content.† The experimental trend of increasing T_g with increasing ACN content was reproduced, however, there is a systematic overestimation in the precise values. For example, the simulated average T_g and its standard deviation at 41.3 % ACN content was (31 ± 19) °C, whereas the experimental value at 40 % ACN content is −29 °C [2, 104].

To investigate whether the large spread of T_g values was an artefact of sampling due to the use of only eight configurations, a benchmark investigation with eighty independently generated and equilibrated configurations was also performed to calculate T_g for NBR of 41.3 % ACN content, constituting a factor of ten increase in the sample size. The resulting distribution in temperatures is shown in Figure 4.14. The average T_g and standard deviation found are (18 ± 26) °C, i.e., the value is closer to the experimental value but the spread is larger. This suggests that sampling alone is not responsible for the disparity between simulation and experiment.

One reason for the difference might be that discrepancies in the measured T_g exist even amongst experiments. For example, an order of magnitude change in the cooling rate in experiment can lead to a 3–5 °C change in T_g [144]. Furthermore, the cooling rates used in experiment are much lower than those used in these simulations, e.g., typically 0.1–1 °C s^{-1} in experiment, compared with 10–100 °C ns^{-1} in simulation [142, 145]. Hence, there is a fundamental mismatch of timescales, with the large conformational changes that can take place in experiment not captured in an MD simulation. Additionally, different experimen-

*It is worth noting that the $V(T)$ and $\sum R_i^2$ profiles shown are not necessarily this smooth for all configurations — this example was chosen for the sake of clarity. Additional $V(T)$ curves and the associated $\sum R_i^2$ values are provided in appendix B.

†For high ACN content (50 % or above), an initial temperature of 230 °C instead of 140 °C was required to capture the glass transition.

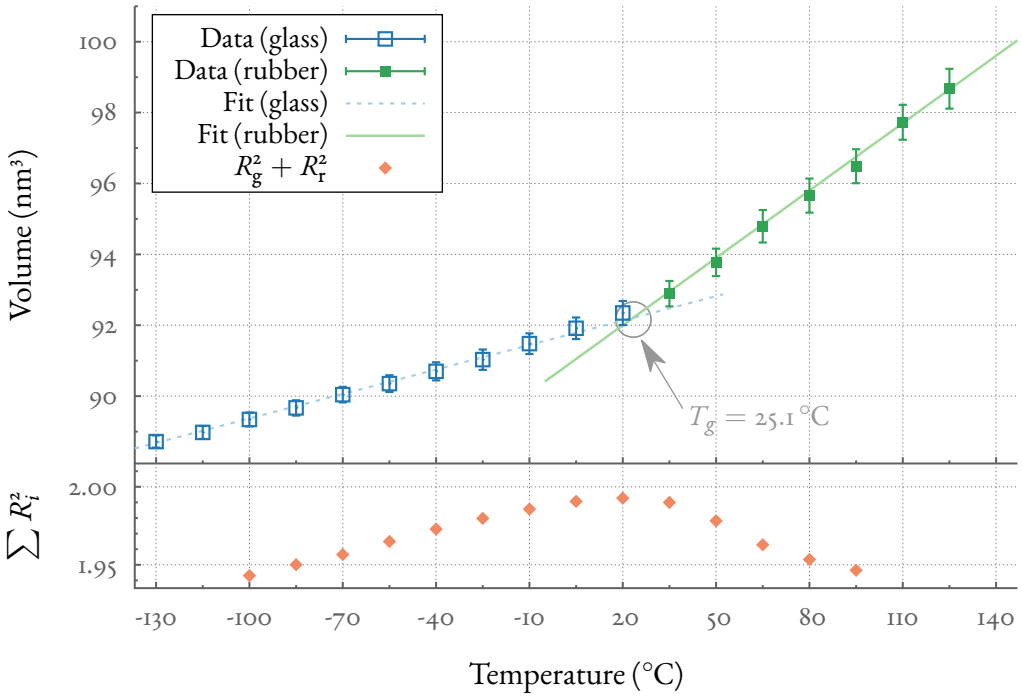


Figure 4.11: A set of volume-temperature data from a series of simulations on NBR of 41.3 % ACN content, which is cooled and allowed to relax gradually in steps of 15 °C over 2 ns. The data is divided into two contiguous regions — representing either the glassy or rubbery states — and a straight line fit is performed on each region, resulting in an R_i^2 value for each. Below, $R_g^2 + R_r^2$ are plotted as a function of the maximum temperature of the glassy region. The last point belonging to this region is chosen to maximise the sum of the residues, and the intersection of the two fits subsequently defines the glass transition temperature, T_g.

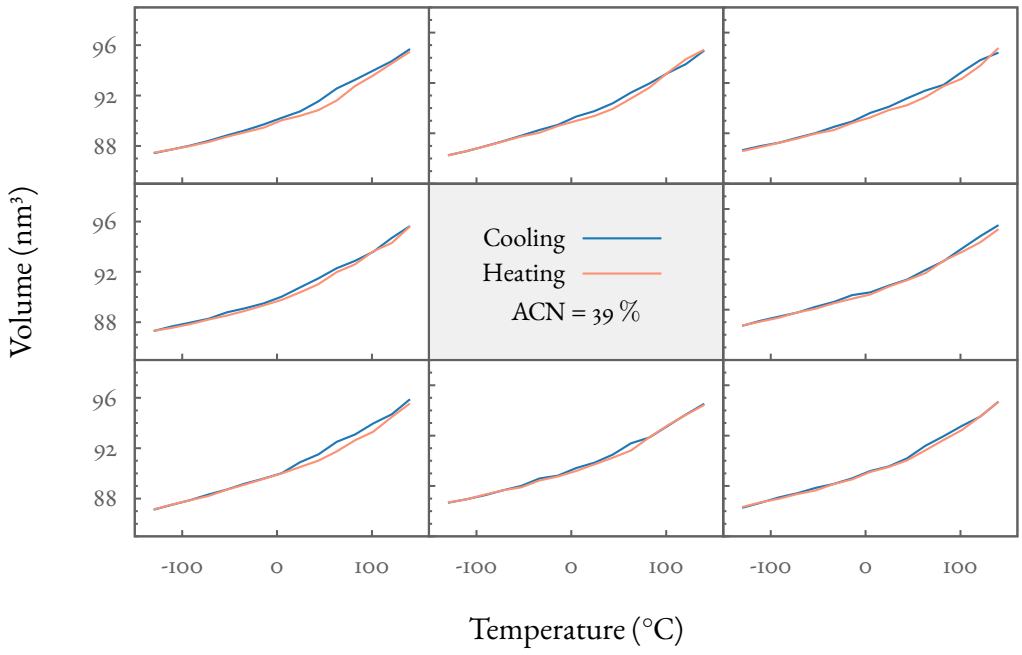


Figure 4.12: Thermal hysteresis during glass transition temperature simulations. The average volume as a function of temperature is computed by either heating or cooling, between −130 °C to 140 °C, over eight independently generated and equilibrated structures of NBR with 41.3 % ACN content. The difference between the two sets of measurements is small.

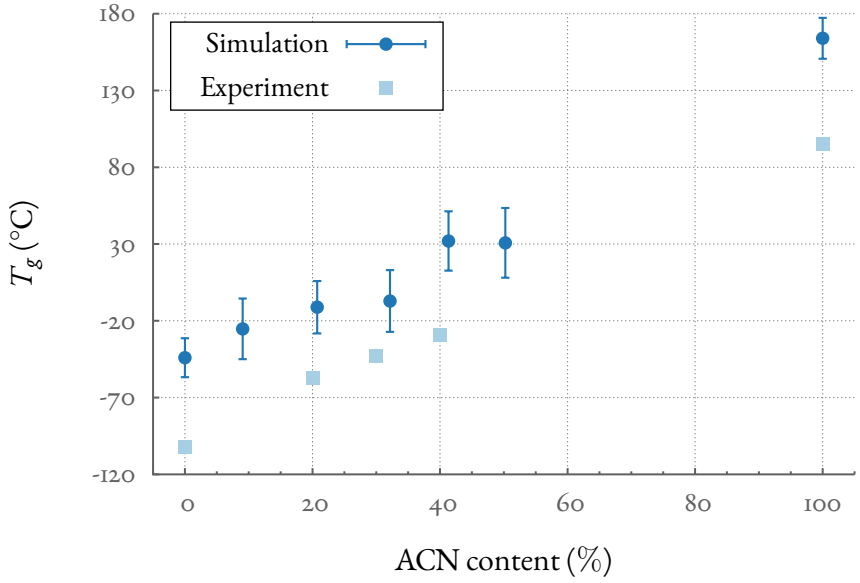


Figure 4.13: Average glass transition temperature, T_g, as a function of ACN content of the elastomer. Each data point is the average over eight simulations, and the error bars represent the standard deviation. Experimental data for raw gum elastomers from Roff and Scott [2] and Brandrup *et al.* [104].

tal techniques are known to give yield different values of T_g [146]. In light of these issues, it is stressed that such simulations should be used more for qualitative predictions than quantitative ones.

4.3.4 Thermal expansion coefficient

The volumetric thermal expansion coefficient, α_V, measures how the volume of a material, V, changes as a function of temperature, T:

$$\alpha_V = \frac{1}{V}\left(\frac{\partial V}{\partial T}\right) . \tag{4.18}$$

This quantity can be calculated from the same procedure employed to compute T_g, described in section 4.3.3, except instead of looking for the intercept between the straight line fits over the glassy and rubbery regions of the $V(T)$ data, the gradients of the fits are extracted and averaged. Experimental data in the literature is in terms of a linear thermal

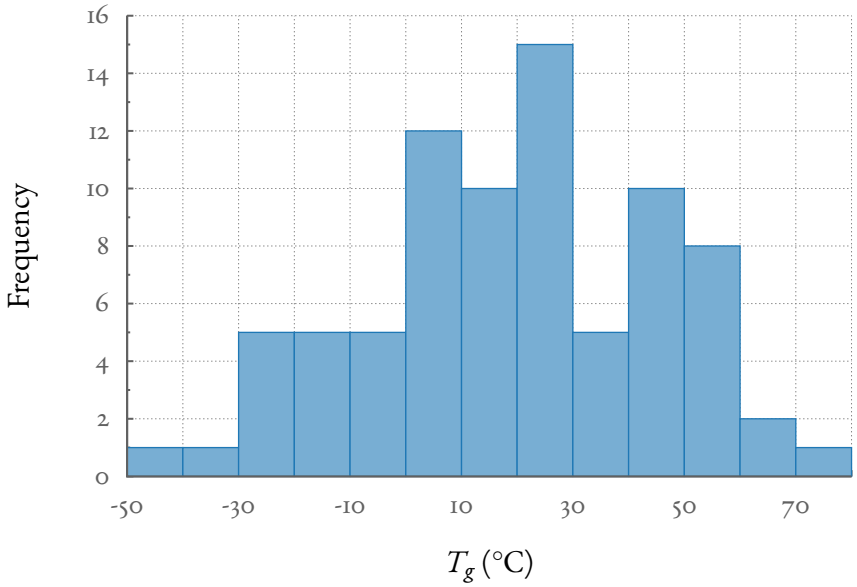


Figure 4.14: Distribution of glass transition temperatures, T_g, computed for eighty independently generated and equilibrated NBR configurations of 41.3 % ACN content. Given the large spread in T_g that is found for a large number of structures, the problem does not appear to be purely a sampling one.

expansion coefficient, α_L, which, for an isotropic material such as an amorphous elastomer, is directly related to α_V by

$$\alpha_L = \frac{1}{3}\alpha_V \,. \tag{4.19}$$

The simulated values of α_L as a function of ACN content, for both the glassy and rubbery states, are shown in Figure 4.15, and are obtained over eight independently generated and equilibrated configurations for each ACN content. There is little variation as a function of ACN content, and the rubbery polymers are more responsive to temperature than the glassy ones. It was not possible to find α_L as a function of ACN content in the experimental literature — the only reported value found was for 'vulcanised NBR' of unspecified ACN content — and was $1.12 \times 10^{-4}\,°\mathrm{C}^{-1}$ [139]. This was presumably measured for NBR at temperatures above room temperature, i.e., above T_g, and therefore the simulated values of α_L are overestimated with respect to experiment. This could explain why T_g was overestimated; a shallower gradient in the $V(T)$ data in the rubbery region would lead to a lower

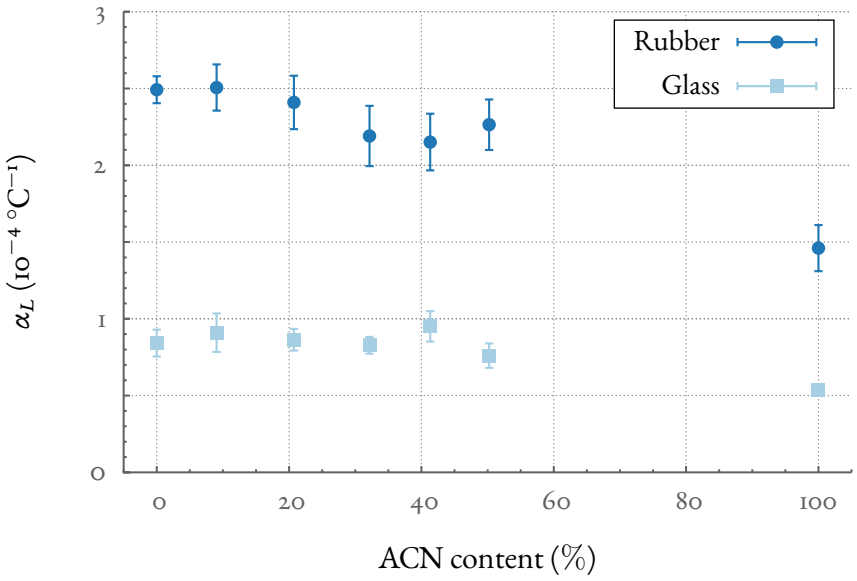


Figure 4.15: Average linear thermal expansion coefficient as a function of ACN content, measured for the glassy and rubbery states of NBR. The error bars represent the standard deviation over the eight independently generated and equilibrated structures used for each data point.

T_g. This effect would not be expected to extend to the glassy region, where polymer relaxation via reptation is less of a factor, due to the temperature being too low for the chain to exhibit long-range co-ordinated motion [45]. Thus the agreement between the computed and experimental values of α_L should be better for glassy NBR.

4.4 Summary

A fully atomistic model for simulating NBR is presented, based on the OPLS potential of Jorgensen *et al.* [26] — the first time, to my knowledge, that a freely-available force-field has been used to describe this polymer. Since OPLS is parameterised for small molecules such as propene, ethane and acetonitrile — not NBR directly — I sought to demonstrate its transferability by computing several bulk properties, comparing to experimental data wherever possible.

Good agreement was found with the experimental density, and the trend of increasing density as a function of ACN content was reproduced. While the trend of increasing glass

transition temperature with ACN content was also reproduced, the numerical discrepancies were large. This was attributed to the multiple orders of magnitude difference in cooling rates between atomistic simulation and experiment, such that the amorphous, entangled polymer was unable to undergo large conformational relaxation via reptation in the timescales studied. From the limited experimental data found for the bulk modulus and thermal expansion coefficient, both exhibited reasonable agreement.

Having developed the model and verified its ability to reproduce trends in bulk properties, I am now in a position to investigate the key issue at the heart of this work; the drivers of permeation through nitrile rubber.

5

Solubility in NBR

In this chapter I build upon my previous work on modelling bulk properties of NBR through atomistic simulation, to identify the key factors influencing the solubility of small gases in NBR — focusing on helium, CO_2 and H_2O — as a function of both base polymer composition and of environmental conditions that reflect those found in an oil and gas exploration context. I demonstrate the importance of careful sampling of the polymer phase-space when performing Widom insertion, both in terms of the size of the ensemble upon which insertions are performed, and the number of insertions required for convergence. I probe the effect of increasing the ACN content in NBR, demonstrating that electrostatics is vital to the solution process in this elastomer, and obtaining good agreement with experimental trends. Using a Voronoi cell approach, the total solubilities are broken down into contributions from particular atomic environments, explicitly illustrating the preference of inserted molecules to sit near nitrogen sites in the elastomer. Temperature and pressure are independently varied and shown to suppress the solubility of polar solutes relative to nonpolar ones, suggesting that the behaviour in oil and gas well conditions may be very different to what has been observed to-date in simulations and experiments conducted under atmospheric conditions.

5.1 Method

5.1.1 NBR model

To generate representative NBR samples at SATP, the method described in chapter 4 was used. In brief, the initial 1000 monomer-long chain of NBR generated at the required ACN content was packed into simulation cell at the experimental density (1000 kg m^{-3} [2]), and equilibrated using LAMMPS over 4 ns. This process is repeated multiple times to generate an ensemble of $n = 24$ conformations sampling the configurational phase space.

For the elevated temperature systems required in section 5.2.3, the same protocol described above was used, after which the structures were heated to the required temperature at a constant rate of 10 °C ns^{-1}, followed by to a 1.5 ns simulation at constant temperature and pressure.

A different approach was used to generate configurations at elevated pressures, also required in section 5.2.3, because it is not possible in MD to simulate the reptation processes that occur in a real polymer subjected to compression. Rather than attempting to simulate compression of the polymer, initial polymer configurations were generated at different densities directly using the the Monte Carlo procedure described in section 4.1.2, subjected to an energy minimisation, and equilibrated in an NVT ensemble to maintain their density, for a total of 4 ns. At constant mass, M, the density, ϱ, is related to the pressure, P, through the bulk modulus, B:

$$B = \varrho \left(\frac{dP}{d\varrho} \right)_M . \tag{5.1}$$

For most elastomers the bulk modulus, i.e., the pressure required to double the density, is approximately 1 GPa [104]. The solubility as a function of pressure/density can then be computed.

Following equilibrations at either SATP or elevated conditions, each structure was evolved dynamically and $m = 250$ snapshots were taken, one every 25 ps for 6.25 ns, to improve sampling for the calculation of solubility.

5.1.2 Solubility

Overview

Solubilities were computed by performing Widom insertion [95] using GROMACS [147] and its "Test Particle Insertion" routine. Random (unbiased) insertions and insertions biased by the free volume were performed.

Parameters for helium were taken from the OPLS force-field, while H_2O and CO_2 were described using the SPC [148] and EPM2 [149] force-fields, respectively. Geometric mixing rules were used to combine the LJ parameters, such that:

$$\sigma_{ij} = \sqrt{\sigma_i \sigma_j} \tag{5.2}$$

$$\varepsilon_{ij} = \sqrt{\varepsilon_i \varepsilon_j}\,, \tag{5.3}$$

where σ and ε describe the width and depth of the LJ potential U_{ij}^{LJ} for an atom of type i and one of type j separated by a distance r_{ij}:

$$U_{ij}^{\mathrm{LJ}} = 4\varepsilon_{ij}\left[\left(\frac{\sigma_{ij}}{r_{ij}}\right)^{12} - \left(\frac{\sigma_{ij}}{r_{ij}}\right)^{6}\right]. \tag{5.4}$$

A full list of parameters is provided in appendix A. For all simulations performed in the NPT ensemble the excess chemical potential given in Eqn. (3.37) is corrected for volume fluctuations [150]:

$$\mu_{\mathrm{ex}} = -k_{\mathrm{B}}T \ln \frac{\langle V_i \exp(-\Delta U_i / k_{\mathrm{B}}T)\rangle}{\langle V_i \rangle}\,, \tag{5.5}$$

where V_i is the instantaneous volume of the simulation cell. This correction is typically small, as the standard deviation in the cell-volumes of the equilibrated structures is less than 0.5 %.

Unbiased Widom insertion

N insertions are performed at random positions, and, if applicable, with random molecular orientations, within a snapshot of the polymer generated using MD. No relaxation is

performed to accommodate the inserted species. The change in the total potential energy ΔU_i upon insertion is computed, the Boltzmann factor is calculated, and these factors are averaged to obtain the solubility according to Eqns. (3.37) and (5.5).

The implementation of this method in GROMACS proceeds as follows: for a given snapshot of a frozen polymer, an initial insertion position is randomly chosen anywhere inside the simulation cell, the atom or molecule inserted, treated as a rigid body and rotated if possible, and the initial neighbour list and long-range electrostatic energies are computed. The remaining short-range terms in the energy are then also calculated, to yield ΔU_i. For the next $a - 1$ insertions (where a is a user-defined parameter), the gas molecule is shifted randomly about its initial position within a sphere of radius r (and a further random rotation applied if applicable), whose value is small such that the neighbour list and long-range electrostatic energies can be assumed to remain unchanged, before the other terms in the energy are computed to obtain ΔU_i at each step. A new initial position is then chosen randomly in the simulation cell, and this process is repeated until N insertions in total have been performed. The insertions are subsequently computationally inexpensive and easily parallelisable.* The parameters a and r were set to 10 and 0.05 nm, respectively.

To obtain solubilities within a standard error of 5 %, $N = 10^8$ insertions are required for all gas molecules, with the exception of helium for which $N = 10^6$ insertions are found to be sufficient,† on $m = 250$ equilibrated snapshots from each of $n = 24$ independent configurations generated with the Monte Carlo procedure described in section 4.1.2.

Biased Widom insertion

Since insertions into regions already occupied by atoms contribute a negligible amount to the solubility, biased insertions are performed only where there is free volume. A map of the free volume is defined for a given snapshot, insertions are performed at random positions (and orientations) within such regions, and the total solubility is calculated after accounting for the bias that has been introduced.

*For example, I am able to run 10^8 insertions on a 8763 atom system in under 6 min on 16 cores using two Intel Xeon E5-2640 v2 processors on a dual-socket motherboard.

†The fact that fewer insertions are required for helium is unsurprising, given that it is smaller than CO_2 and H_2O, and is nonpolar. Furthermore, since it is just a single particle, there is not the added complication of sampling multiple orientations for the same centre-of-mass position.

To generate a map of the free volume the cubic simulation cell is divided into a cubic grid of N_{grid} points, with a helium probe atom placed at each grid point. Using the distance r_{ij} from a probe at point i to a polymer atom j, the number density at that point f_i is computed in terms of a distance d_{ij}:

$$f_i = \sum_{j=1}^{N_{\text{atoms}}} H(d_{ij}) \,, \tag{5.6}$$

$$d_{ij} = (1 - \alpha)\sqrt{\sigma_{\text{He}}\sigma_j} - |r_{ij}| \,, \tag{5.7}$$

where H is the Heaviside step function, σ_{He} and σ_j are the LJ widths of the helium probe and the polymer atom, respectively, α is a free parameter used to tune the definition of the free volume, and the sum is performed over the N_{atoms} in the polymer.* The free volume sites are defined as those for which $f_i = 0$.

The set of free volume sites for a given snapshot are then passed into a modified version of GROMACS' particle insertion routine, `tpi.c`, in which insertions are performed in each of the voxels centred on the grid points. Since they are small, no larger than 0.1 nm, within a given voxel it is assumed that the neighbour list and long-range electrostatic energy remain unchanged, therefore additional positions and orientations after the first one may be sampled while only recomputing the short-range terms in the energy. The effect of changing the number of insertions per grid point is examined in the results section, along with the sensitivity of the solubility to the free volume. The final values chosen are $\alpha = 0.2$, $N_{\text{grid}} = 10^6$ and 100 insertions per grid point defined as free volume. For a fractional free volume of 1 % this corresponds to 10^6 insertions in total — 100 times fewer than the full Widom insertion method. While it takes time to generate a free volume map, this is required only once per snapshot as it is independent of the molecule being inserted, and therefore the speed-up is close to a factor of 100.†

The bias introduced by sampling insertions only in regions of free volume is accounted

*In practice the sum is terminated as soon as a non-zero term is found, as the precise number density of the excluded-volume is not required, merely the sites corresponding to free volume.

†Without using any optimisation techniques such as constructing cell lists to limit the domain of potential atomic neighbours, the free volume map generation over 10^6 grid points takes only 30 s on a single core of an Intel Xeon E5-2640 v2.

for by multiplying the solubility by the probability of insertion in free volume, i.e., the fractional free volume:

$$s = \frac{N_{\text{fv}}}{N_{\text{grid}}} \exp\left(-\mu_{\text{ex}}/k_{\text{B}}T\right) \ , \tag{5.8}$$

where N_{fv} is the number of free volume sites, i.e., those where $f_i = 0$.

Spatially resolved solubilities

To illustrate the inhomogeneity of 'successful' insertions in the polymer, i.e., those that contribute to the solubility, insertions were performed using unbiased Widom insertion and the resulting positions and accompanying Boltzmann factors were binned along one side of the cubic simulation cell, which was chosen to be along the y-direction, without loss of generality. I define the fractional co-ordinate in the y direction, $y' = y/L$, where L is the length of the cubic simulation cell, and y' is in the range $[0, 1)$. The solubility in a bin of width w centred at y' is

$$s(y') = \frac{\sum_{i=1}^{N} \exp\left(-\Delta U_i/k_{\text{B}}T\right) g\left(L(Y'_i - y')/w\right)}{\sum_{i=1}^{N} g\left(L(Y'_i - y')/w\right)} \ , \tag{5.9}$$

where insertion i is at fractional co-ordinate Y'_i, with corresponding insertion energy ΔU_i, N insertions are performed in total and $g(x)$ is a top hat function given by

$$g(x) = \begin{cases} 0 & |x| \geq \frac{1}{2} \\ 1 & |x| < \frac{1}{2} \end{cases} \ . \tag{5.10}$$

The effect of varying the number of snapshots, m, taken from a long MD run from each of n independent initial configurations can then be investigated by averaging $s(y')$ over different combinations of $n \times m$.

Owing to the demands on processor, memory and storage of writing and sorting the $N = 10^8$ insertions performed on up to $n \times m = 24 \times 250 = 6000$ configurations, most of which contribute a negligible amount to the solubility, only the subset of inser-

tions whose insertion energies were less than $5k_B T (T = 25\,^\circ\mathrm{C})$ were used. For CO_2 this approach reduced the number of insertions written per snapshot from 10^8 to approximately 8×10^4, i.e., a factor 1000 fewer insertions to process, while maintaining the precision of the solubility at better than one part in 10^6 as compared to the case where all insertions are used. This requires changing the normalisation factor in Eqn. (5.9) from the actual number of insertions per bin to the expected number of insertions per bin:

$$s(y') = \frac{\sum_{i=1}^{N} \exp\left(-\Delta U_i / k_B T\right) g\left(L(Y'_i - y')/w\right)}{Nw/L} \,. \tag{5.11}$$

Localised solubility

To identify the atomic environments in NBR where polar gases have lower energies, the total solubility of each gas in NBR of fixed ACN content (41.3 %) at SATP was decomposed into contributions according to the type of atom in the polymer closest to the inserted molecule. Voronoi cells were constructed around each atomic site in the polymer (Figure 5.1), ignoring hydrogen atoms, using the Voro++ library [151], and unbiased Widom insertions were sorted into the Voronoi cells according to the positions of the centres of mass of the inserted molecules, together with the corresponding Boltzmann factors. Sorted insertions belonging to atoms of the same orbital hybridisation state — sp^1, sp^2, sp^3 carbons, nitrogen — are grouped and the Boltzmann factors summed and normalised by the total Boltzmann factor across all groups, so that the relative contribution of different atomic sites can be compared across different inserted molecules, while the solubilities per group sum to the total solubility. As with the spatially resolved solubilities, only insertions whose energies were less than $5k_B T$ were used in this procedure.

Errors

Standard error In determining the standard error, it would be incorrect to treat all $n \times m$ snapshots as independent, since snapshots generated from the same starting configuration will be correlated with one another because the relaxation time of the polymer exceeds the duration of the simulations. Instead, for initial configuration i, where $i = 1, 2, \ldots, n$, the solubilities s_{ij} computed for the m snapshots, where $j = 1, 2, \ldots, m$,

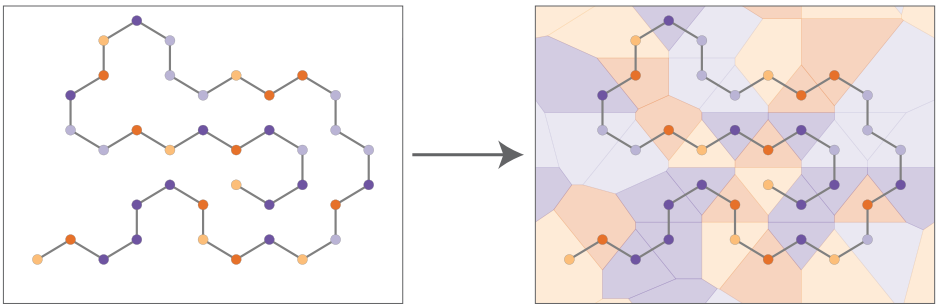


Figure 5.1: Schematic illustrating Voronoi decomposition of a polymer by atom type, where any point in the cell around a given atom is closest to that particular atom. Periodic boundary conditions are respected in the decomposition.

are used to calculate an average solubility s_i. The set of values of s_i is then averaged over the n independent starting configurations to obtain $\bar{s}$, and the standard error, SE, may be calculated using the standard deviation σ of the n values of s_i:

$$s_i = \frac{1}{m} \sum_{j=1}^{m} s_{ij} \,, \tag{5.12}$$

$$\bar{s} = \frac{1}{n} \sum_{i=1}^{n} s_i \,, \tag{5.13}$$

$$\sigma^2 = \frac{1}{n} \sum_{i=1}^{n} (s_i - \bar{s})^2 \,, \tag{5.14}$$

$$\mathrm{SE} = \frac{\sigma}{\sqrt{n}} \,. \tag{5.15}$$

The standard error in the solubility is reduced by using n independent starting configurations because the spread in the average solubilities s_i for each starting configuration is smaller.

Resampling The convergence of the standard error in the solubility with n, $\mathrm{SE}(n)$, becomes poor when n is small. For example, the standard error for $n = 2$ depends on which two initial configurations were chosen. These fluctuations eventually become negligible for sufficiently large n. Randomised subsampling can be used to dampen the fluctuations [152–154], by sampling subsets of the data, computing the statistical quantity of interest for each

subset, and averaging all the quantities. This enables the computation of, e.g., the average standard error as a function of the number of independent configurations, $\overline{\mathrm{SE}}(a)$, which is useful for determining how many configurations are needed to obtain the solubility to within a desired level of precision. The method to compute $\overline{\mathrm{SE}}(a)$ is as follows: given n average solubilities in total, randomly select a of them, compute the standard error as previously described over the a solubilities, and repeat this process until $\overline{\mathrm{SE}}(a)$ has converged (10^3 attempts were found to be sufficient).

5.2 Results and discussion

5.2.1 Convergence

First, I present a study of the convergence of the solubilities computed with the unbiased and biased Widom insertion techniques with respect to the number of independent initial configurations, n, the number of snapshots, m, taken from MD simulations after equilibrating each initial configuration, and the number of insertions per snapshot, N. I justify the choice of $n = 24$ and $m = 250$ based on the convergence of the standard error in the solubility of CO_2, and the significant inhomogeneity of CO_2 insertions for small n, m. Then I justify the choice of $N = 10^8$ for the unbiased Widom insertion technique, and highlight the advantages that biased insertion offers over unbiased insertion by reducing N for the same precision in the solubility.

For biased Widom insertions, the sensitivity of the solubility to the free volume is evaluated in terms of the number of grid points and the free volume tuning parameter, α, set at 10^6 and 0.2, respectively. All convergence simulations are performed at SATP for NBR of 41.3 % ACN content.

Number of starting configurations and number of snapshots

Figure 5.2 shows the standard error in the solubility of CO_2 as a percentage of its average solubility, as a function of the number of starting configurations, n, and the number of snapshots for each, m, for the unbiased and biased Widom insertion techniques. Random resampling is performed using 10^3 steps to smooth out the fluctuations that would other-

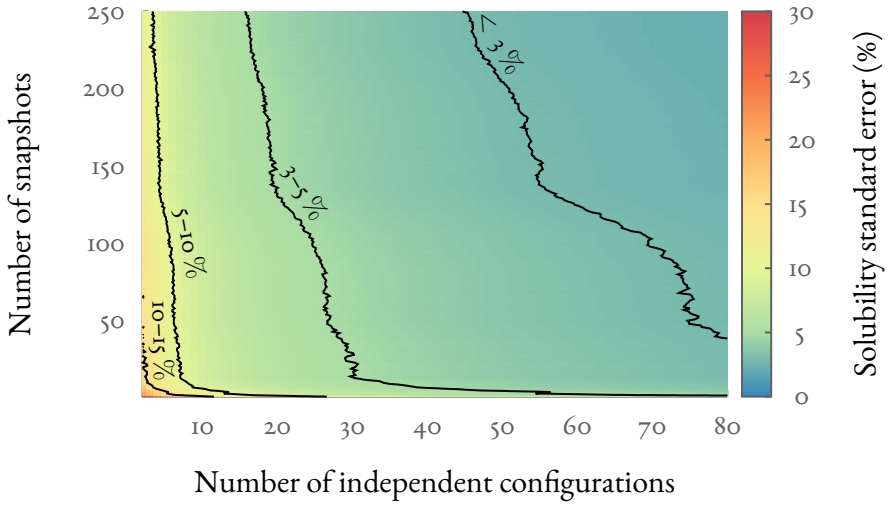
wise arise for small n. Increasing n brings about the most rapid reduction in the standard error. However, this has to be balanced against computational cost because to equilibrate an independent configuration requires a 4 ns simulation, whereas generating an additional snapshot takes only 25 ps. Balancing these considerations while minimising the standard error in the solubility led to the choice of $n = 24$ and $m = 250$. The convergence is almost identical for unbiased and biased Widom insertion techniques.

In Figure 5.3a, CO_2 insertions are performed using the unbiased Widom insertion technique and are binned along one side of the cubic simulation cell to create a continuous distribution, using the approach described in section 5.1.2. This averaging is performed over the $n \times m$ snapshots. The standard deviation in this solubility distribution is calculated as a percentage of the average solubility, as a function of n and m, and is shown in Figure 5.3b. Figures 5.3a and 5.3b show that the distribution becomes more homogeneous when n and m are increased. The bin size was 5 % of the length of the simulation cell, 0.23 nm wide on average.

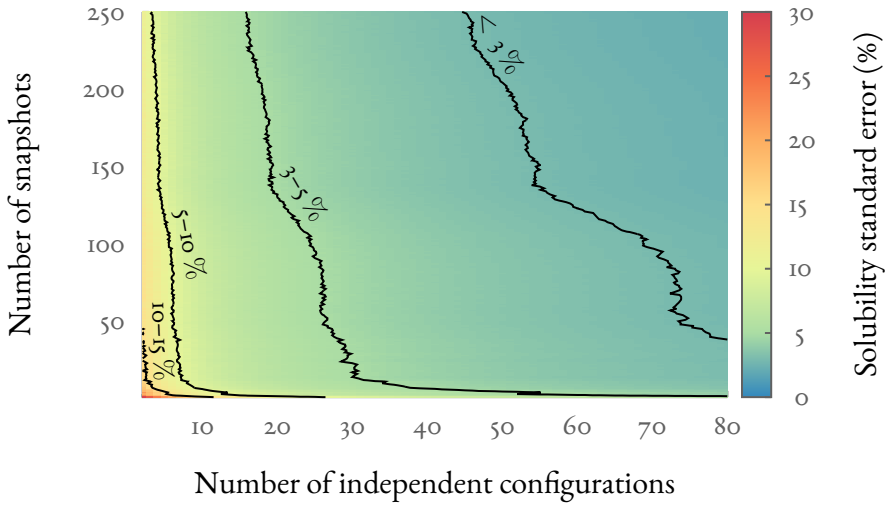
Whilst Figure 5.3a shows that even with 24 independent configurations, and 250 snapshots for each of them, the solubility distribution is not entirely homogeneous, Figure 5.3b shows that increasing n, m, beyond these values yields diminishing returns.

Number of insertions

Figure 5.4 shows regions within a single snapshot of an equilibrated simulation cell of NBR where the solubilities of CO_2, H_2O and helium are relatively high. Insertions are performed using the unbiased Widom insertion technique, and the associated Boltzmann factors are sorted into a 3D grid of $100 \times 100 \times 100$ voxels based on the position of the centre-of-mass of the inserted molecule. Summing over the Boltzmann factors within a voxel and dividing by the total number of insertions performed gives the local solubility. Regions where the local solubility is less than 10^{-8} are not shown. As CO_2 is the largest molecule of the three there are relatively few regions where its solubility is significant, whereas helium is more homogeneously distributed. Water is more homogeneously distributed in the snapshot and its local solubilities are greater than those of CO_2. I would speculate that the former is due to the smaller van der Waals volume of water and the latter is due to the electrostatic interac-

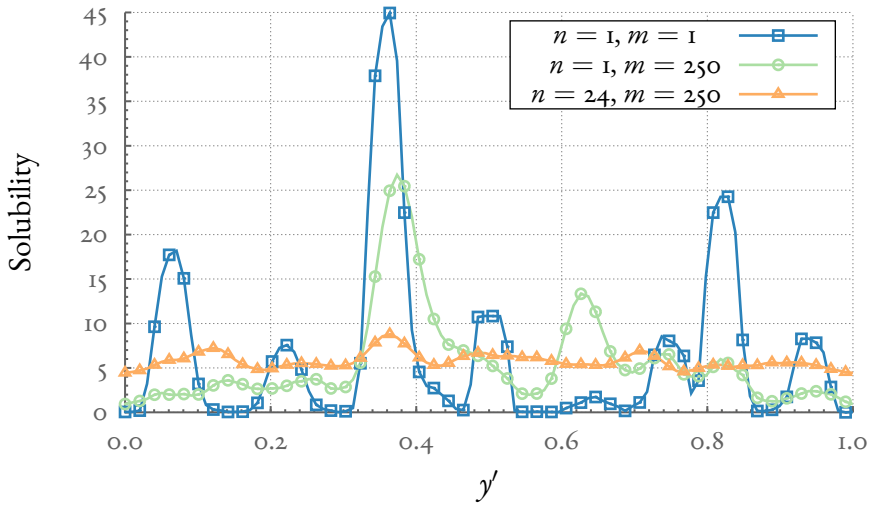


(a) Unbiased Widom insertions

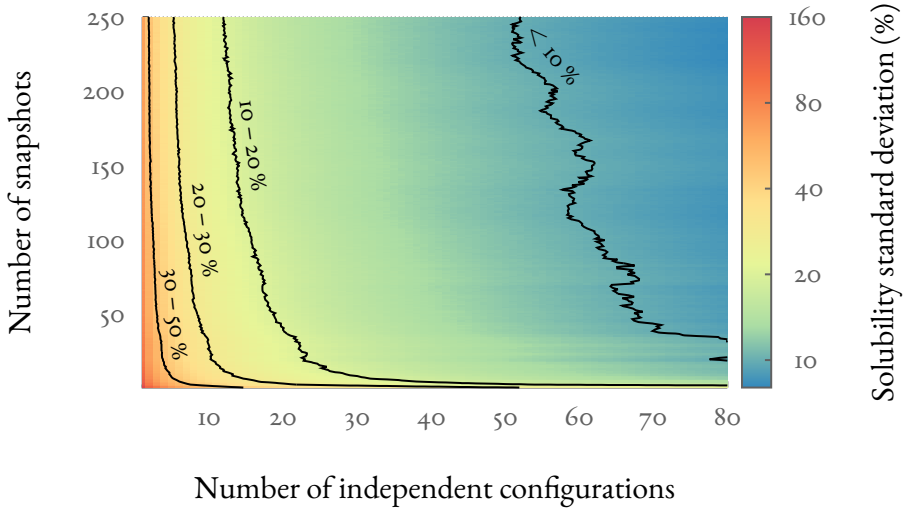


(b) Biased Widom insertions

Figure 5.2: Convergence of CO_2 solubility with number of independently generated configurations and number of dynamically evolved snapshots, in terms of the standard error as a percentage of the solubility. The unbiased Widom insertion technique uses 10^8 insertions per snapshot. The biased Widom insertion technique uses 10^6 grid points, 100 insertions per grid point identified as free volume and $\alpha = 0.2$.



(a) Continuous histogram



(b) Standard deviation

Figure 5.3: (a) Distributions of computed solubility of CO_2 as a function of the normalised position y' along one side of the simulation cell, plotted for different numbers of independently generated configurations (n) and dynamically evolved snapshots (m). (b) Percentage standard deviation in the solubility distributions from their average values, as a function of n and m, where randomised resampling has been used to smooth the fluctuations that would otherwise dominate for small n. Insertions performed using the unbiased Widom insertion technique with $N = 10^8$.

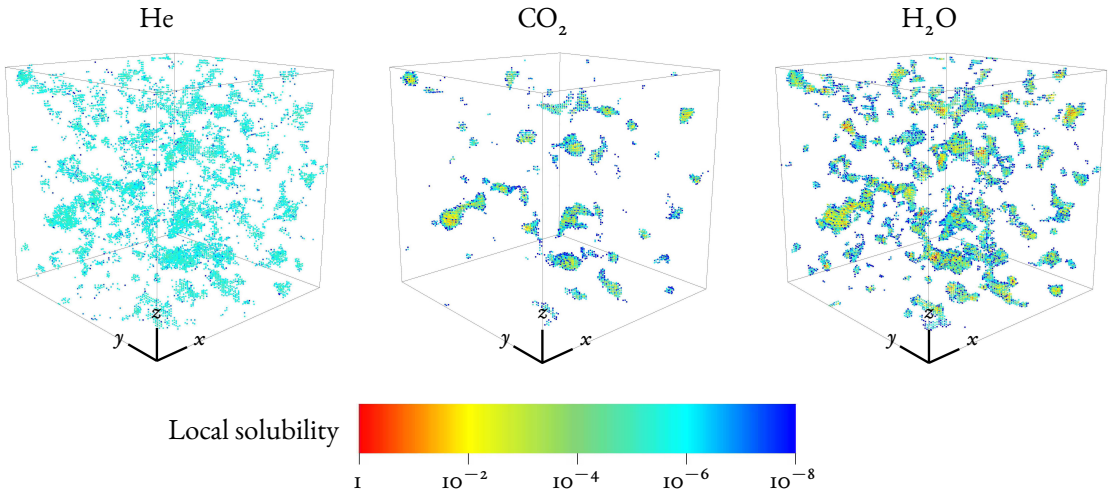


Figure 5.4: Local solubilities of CO_2, H_2O and helium in the same snapshot of NBR. Only cells with local solubility higher than 10^{-8} are shown. Insertions performed using unbiased Widom insertion technique with $N = 10^8$. Image generated using VisIt [155].

tion between its dipole and dipoles in the elastomer, such as the C≡N bond in ACN, which is a stronger and longer-ranged interaction than CO_2 can achieve through its quadrupole. For all three molecular species successful insertions are very localised, indicating that the biased Widom insertion technique would be more efficient.

Figure 5.5 shows the convergence of the solubility of CO_2 as a function of the number of insertions, for both the unbiased and biased Widom insertion techniques. For the former, 10^{10} insertions were performed on each snapshot, corresponding to a sampling density of approximately 10^8 nm^{-3}, and this defined the limiting solubility s_{lim}. A subset N of these insertions were randomly selected and averaged to obtain a solubility s_N, and the relative root-mean-square deviation of s_N from s_{lim} was computed, i.e., $|s_N - s_{\text{lim}}|/s_{\text{lim}}$. Due to the noise in the data, random resampling was performed as described in section 5.1.2. This procedure was repeated over a single snapshot generated from each of $n = 24$ independent configurations, and the fractional error averaged as a function of number of insertions. With every increase in the number of insertions, the difference in the fractional error drops, suggesting that it is asymptotically approaching the $N \to \infty$ solubility limit. In practice it was found that using 10^8 insertions over $n \times m = 24 \times 250 = 6000$ snapshots was sufficient to ensure a standard error in the solubility of no more than 5 %.

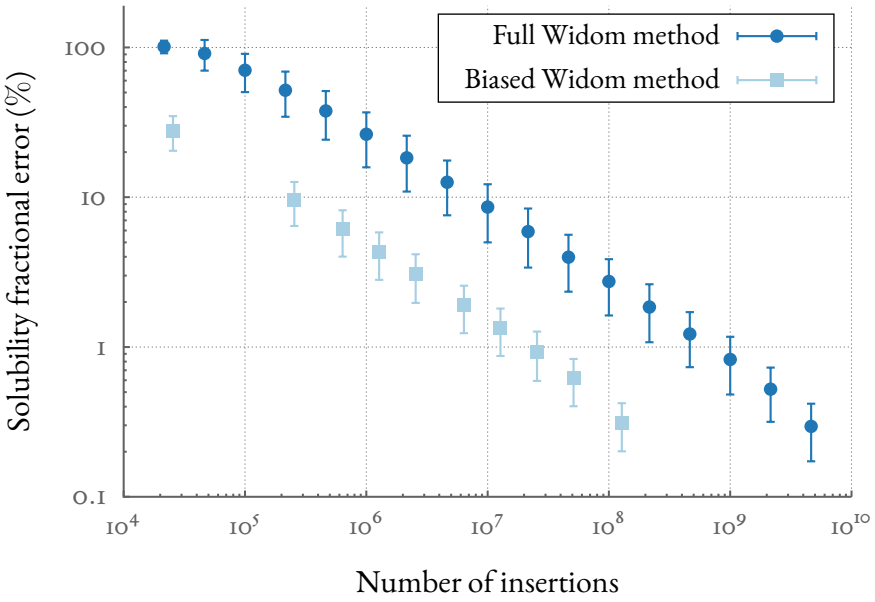


Figure 5.5: Convergence of CO_2 solubility with number of insertions is shown for both the unbiased Widom and biased Widom insertion techniques, in terms of the fractional error of the solubility $|s_N - s_{\text{lim}}|/s_{\text{lim}}$, where s_N is the solubility after N insertions. For the unbiased Widom insertion technique, s_{lim} corresponds to the solubility after a total of 10^{10} insertions. For the biased Widom insertion technique, s_{lim} corresponds to the the solubility obtained after performing 10^4 insertions per grid point defined as free volume. The number of grid points is 10^6, the free volume tuning parameter, α, is 0.2, and the average fractional free volume is $(2.55 \pm 0.07)\,\%$. The fractional error is averaged over one snapshot obtained from each of 24 initial configurations. The error bars represent the standard deviation in the fractional error.

For biased Widom insertion, the approach to calculating s_{lim} is similar except that the total number of insertions is not a user-definable parameter as it depends on the fractional free volume of the system. Instead I define the number of grid points (10^6) and the number of insertions per grid point (10^4), and the total number of insertions is then inferred as the fractional free volume times the product of these two quantities. The biased Widom insertion technique converges significantly faster than the unbiased Widom insertion technique, reaching a fractional error of less than 5 % with approximately 100 times fewer insertions, corresponding to 50 insertions per grid point. To account for possible variations between different inserted molecular species and NBR of differing ACN content, a conservative value of 100 insertions per grid point was chosen.

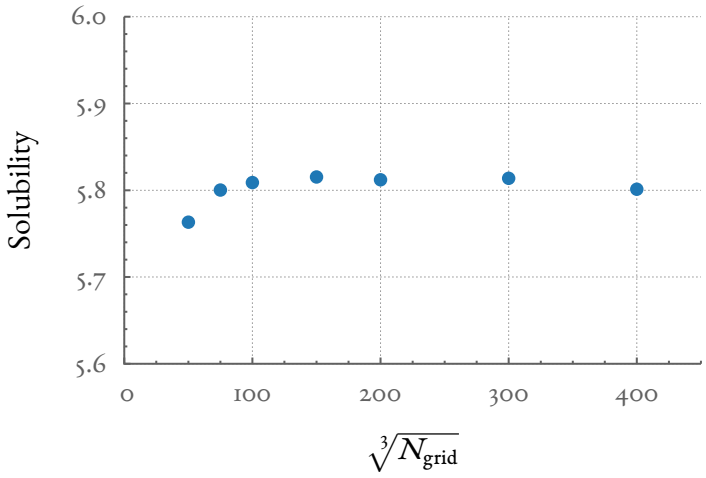


Figure 5.6: Convergence of CO_2 solubility with number of grid points per dimension, $\sqrt[3]{N_{\text{grid}}}$. 100 insertions per grid point defined as free volume, $\alpha = 0.2$.

Free volume

Figure 5.6 shows the solubility of CO_2 as a function of the number of grid points per dimension, $\sqrt[3]{N_{\text{grid}}}$. The number of insertions per voxel centred on each grid point of width $L/\sqrt[3]{N_{\text{grid}}}$ for a cubic simulation cell of length L, is fixed at 100, and $\alpha = 0.2$. The error bars represent the standard error, and are approximately 3 % of the solubility. From this data it is inferred that 10^6 grid points is sufficient to achieve reasonable convergence.

Figure 5.7 shows the effect of the free volume tuning parameter, α, on the solubility of CO_2 as well as the fractional free volume (FFV). For large, negative values of α, the lack of free volume sites in which to perform insertions means that the solubility is far from its converged value. For values above approximately 0.15, the solubility becomes independent of α, and, since the computational cost of particle insertion scales approximately linearly with the number of insertions, which in this case is proportional to the FFV, a conservative value of $\alpha = 0.2$ is chosen, corresponding to an average FFV and standard deviation of (2.55 ± 0.07) %, i.e., approximately 40 times faster than the random insertions for the same number of insertions per unit volume.

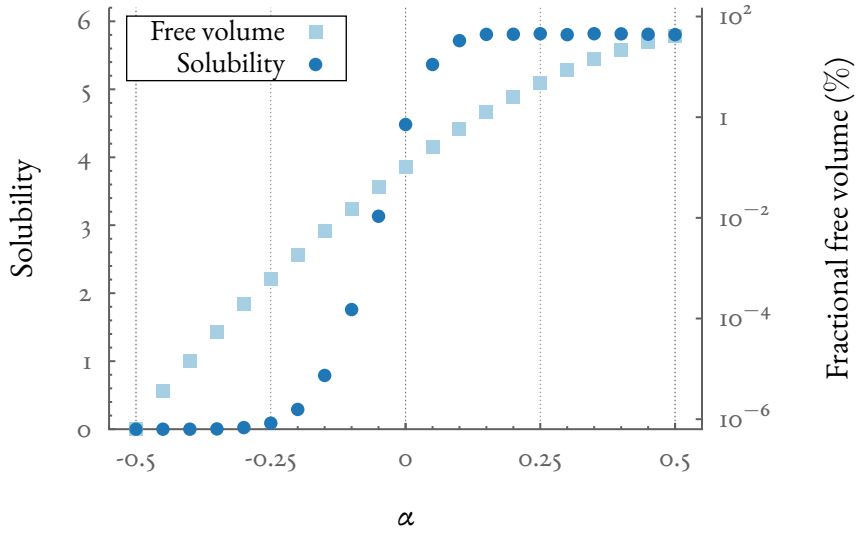


Figure 5.7: Convergence of CO_2 solubility and polymer free volume with α, a parameter used to tune the radius, $r = (1 - \alpha)\sqrt{\sigma_{He}\sigma_j}$, used to define the free volume, where σ_{He} and σ_j are the LJ radii of helium (0.2556 nm) and atom j of the polymer, in the OPLS-AA force-field. 100 insertions per grid point, 10^6 grid points.

5.2.2 Solubility at standard conditions

When studying permeation of small gas molecules through NBR, Van Amerongen [71, 92] found that CO_2 demonstrated higher gas permeability compared with nonpolar gases, due to its higher solubility. For example, the permeability of CO_2 in NBR (32 % ACN content) is almost double that of helium, despite its diffusivity being approximately an order of magnitude smaller. Here I seek a quantitative understanding of the enhanced solubility of CO_2.

One of the main parameters that may be varied when creating a commercial formulation of NBR is the ACN content. As the ACN content is increased, the glass transition temperature of the polymer is raised, it becomes stiffer, and its resistance to swelling from fuels improves [2]. In Figure 5.8 the computed solubilities for CO_2 and helium as a function of ACN content are compared with the limited experimental data available, taken from Van Amerongen [71]. Consistent with other Widom insertion simulations in the polymer literature [100], the solubilities are overestimated with respect to experiment by a factor of between two to five.

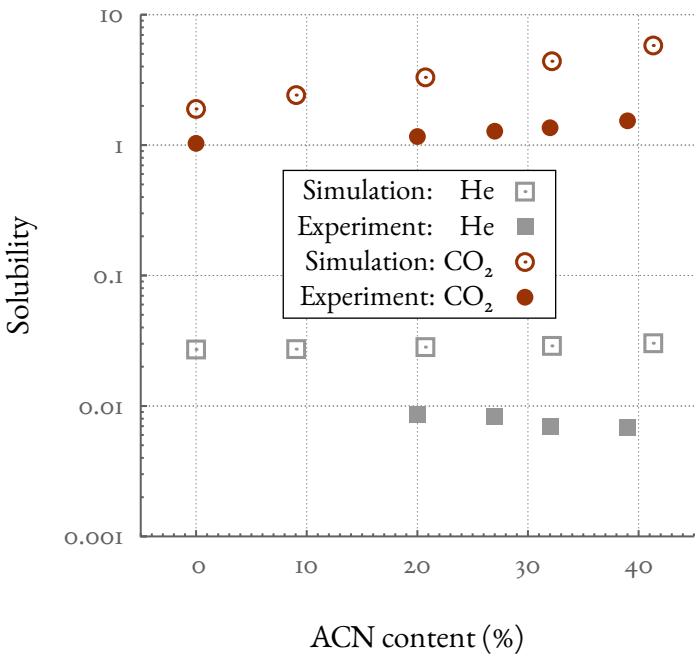


Figure 5.8: Solubility of helium and CO_2 as a function of ACN content from simulation and experiment. Experimental data from Van Amerongen [71] for NBR at SATP. Insertions performed using biased Widom insertion technique with 100 insertions per grid point identified as free volume, 10^6 grid points and $\alpha = 0.2$. NBR snapshots generated at SATP.

Despite the comprehensive convergence tests performed in this work, it is not possible to rule out the possibility of sampling issues in these simulations. It may be the case that in reality the length-scale over which the polymer is homogeneous is longer than the typical dimensions of a molecular simulation, e.g., due to the presence of submicroscopic voids [8].

Another factor is the force-field, to which the solubility is sensitive as a result of the exponential dependence on the energy, shown in Eqns. (3.37) and (3.38). The non-bonded parameters in force-fields such as OPLS are parameterised using bulk static properties such as density and heat of vaporisation, and it is unlikely that this will ensure a correct treatment of properties dependent on local atomic environments such as solubility of gases and transport properties.

Nevertheless the experimental trends with ACN content are reproduced. In particular, the solubility of CO_2 is found to be higher than that of helium, despite CO_2 being larger. This could be attributed to electrostatics, since CO_2 is a quadrupolar molecule, but may also be related to van der Waals effects, since the LJ interaction is both stronger and longer-ranged for CO_2. To investigate the contribution of electrostatics, in Figure 5.9 the solubility of nonpolar CO_2, i.e., with its partial charges set to zero, was studied, and compared to the solubility of normal CO_2, helium, H_2O and nonpolar H_2O.

The solubilities of all gases increased with increasing ACN content, but the increase is most pronounced with polar gases. This suggests that the electrostatic interaction between the ACN monomer and the molecules is responsible, which seems reasonable given that the ACN monomer contains the largest dipole in the polymer, in the C≡N functional group, and H_2O and CO_2 contain a dipole and a quadrupole, respectively.

The nonpolar CO_2 and H_2O molecules exhibit higher solubilities than that of helium, suggesting that the stronger and longer-ranged van der Waals interactions in these molecules are able to overcome their larger molecular volumes. Indeed this also appears to be the case for nonpolar CO_2 versus nonpolar H_2O, since CO_2 has the higher solubility despite being larger (nonpolar SPC H_2O is effectively just an oxygen atom* since the hydrogen atoms are only virtual charge sites with zero LJ interactions).

It is perhaps surprising that the solubility is increasing even though the density of NBR is known to increase with ACN content both in experiment [1] and in simulation (sec-

*Albeit one with a slightly larger σ than oxygen would usually have.

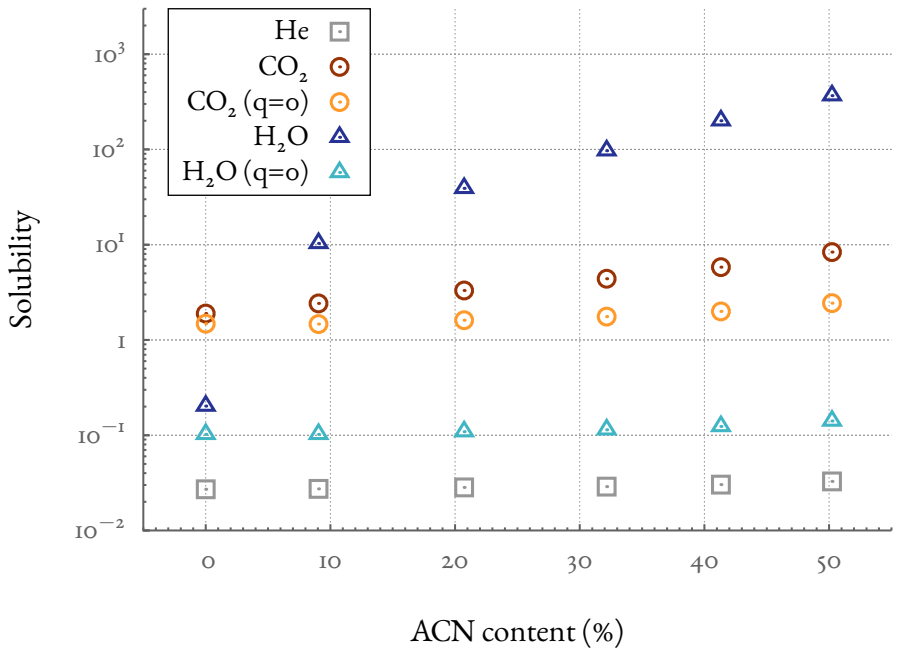


Figure 5.9: Calculated solubilities of CO_2, H_2O and helium as a function of ACN content. For CO_2 and H_2O solubilities are also shown for the cases where the atomic charges are turned off ($q = 0$). Insertions performed using biased Widom insertion technique with 100 insertions per grid point identified as free volume, 10^6 grid points and $\alpha = 0.2$. NBR snapshots generated at SATP.

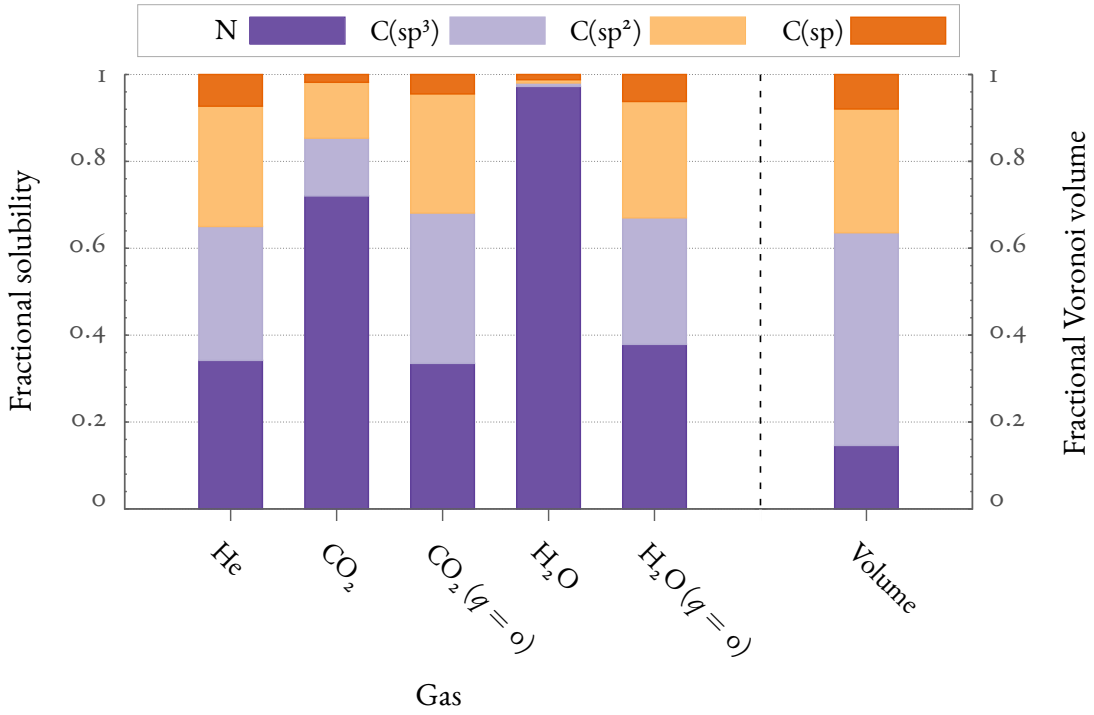


Figure 5.10: The total solubility for each gas decomposed into fractional contributions according to the atomic environment where the gas is located. The fractional volumes associated with each atomic environment are shown on the right for comparison. Insertions performed using the unbiased Widom insertion technique with $N = 10^8$. NBR of 41.3 % ACN content generated at SATP.

tion 4.3.1). However, in my simulations the total free volume increases with ACN content too, by approximately 11 % when going from 0 % ACN (i.e., amorphous polybutadiene) to NBR of 50.2 % ACN content. This could be attributed to the increasing number of side-chains in the system, randomly distributed along the chain, hindering efficient packing of the polymer and therefore increasing the available volume for insertions, the number of successful insertions and the solubility.

To investigate further the reasons for the increasing solubility with ACN content, in Figure 5.10 a break-down is shown of the total solubility of various gases in NBR into localised contributions from each atom type in the polymer (excluding hydrogen), where the hybridisation states of carbon atoms are distinguished. The fractional volume associated with each atomic environment is calculated using the Voronoi cell construction described ear-

lier and is also shown in Figure 5.10. Given that there is only one nitrogen atom per ACN monomer, it is unsurprising that nitrogen and the sp carbon it is bonded to take up the least volume in the system. However, in spite of this, a disproportionate fraction of the solubility of all gases comes from insertions that fall closest to nitrogen atoms. This is especially noticeable for gases with electrostatic interactions, such as CO_2 and H_2O, with almost all of the solubility of water being attributed to nitrogen environments.

For helium, since its interaction with the polymer is almost entirely repulsive ($\varepsilon = 0.02\,\mathrm{kcal\,mol^{-1}}$), its distribution of solubilities will effectively be the same as that of a hard sphere, i.e., it will largely reflect the free volume in the system. Other gases with no electrostatic interactions with the polymer exhibit similar distributions in their solubilities to that of helium.

5.2.3 Solubility at elevated temperature and pressure

Temperature

As shown in Figure 5.11, raising the temperature affects the solubility of different gas species in different ways, suppressing the solubility of CO_2, nonpolar CO_2 and H_2O, but enhancing that of helium and nonpolar H_2O. The computed and experimental [71] solubilities for CO_2 and helium are also compared, showing that my simulations on CO_2 agree with the trend found in experiment, while the slight increase in the solubility of helium between 25 °C and 50 °C found experimentally seems to be too subtle to be seen in my simulations.

Pressure

As reported widely in the literature, care has to be taken when performing any type of Widom insertion on dense systems when fewer attempted insertions are successful, owing to the increased probability of atomic overlap between solute and host. The CO_2 convergence tests performed at atmospheric pressure and 25 °C were repeated at two higher pressures to test the effect of independently varying the free volume tuning parameter, α, from 0.2 to 0.5, the number of grid points per dimension, $\sqrt[3]{N_{\mathrm{grid}}}$, from 100 to 400, and the number of insertions per grid point from 100 to 2000. For $P \approx \frac{1}{4}B = 250\,\mathrm{MPa}$ or $\varrho = 1200\,\mathrm{kg\,m^{-3}}$, it was found that in all cases the average solubility was within 5 % of the

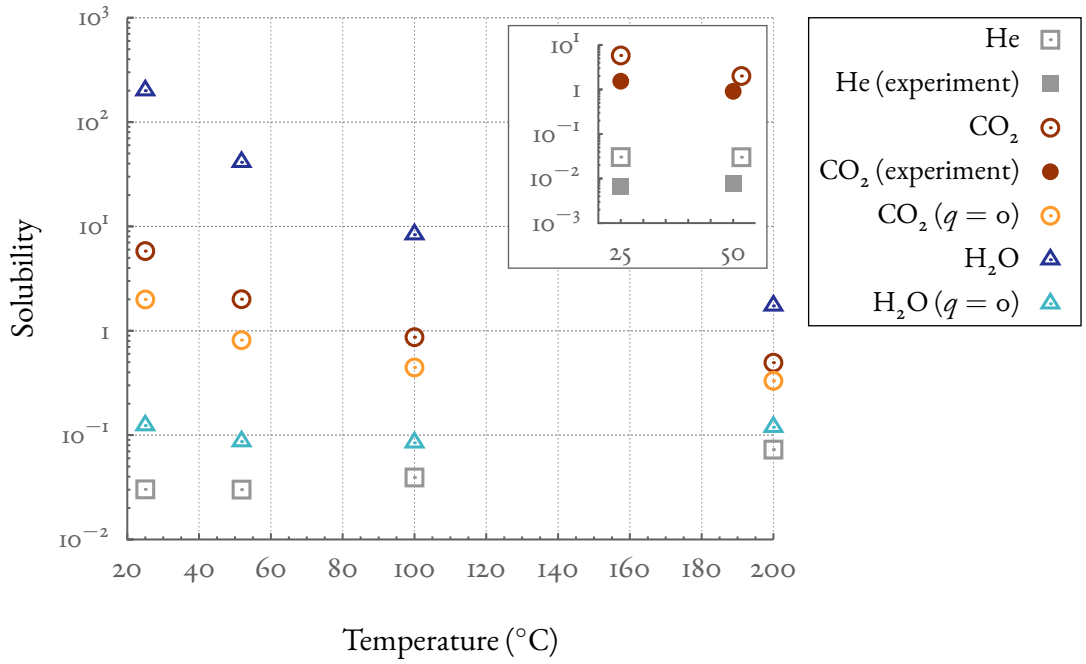


Figure 5.11: Solubilities of various gases in NBR as a function of temperature. Inset: comparison of simulated and experimental solubilities for CO_2 and helium. Simulations performed at standard pressure for NBR of 41.3 % ACN content. Insertions performed using biased Widom insertion technique with 100 insertions per grid point defined as free volume, 10^6 grid points and $\alpha = 0.2$. Experimental data from Van Amerongen [71] for NBR of 39 % ACN.

original value of 0.027. For $P \approx \frac{1}{2}B = 500$ MPa or $\varrho = 1440\,\mathrm{kg\,m^{-3}}$, the solubility was within an order of magnitude of the original value of 10^{-15}, i.e., effectively zero. Therefore I returned to using the original parameters.

The solubility as a function of density is shown in Figure 5.12, where the density of NBR at SATP in simulation is $\varrho \approx 960\,\mathrm{kg\,m^{-3}}$ (from section 4.3.1). Whilst all gases exhibit a decrease in their solubilities with increasing density, the rates at which they decrease vary. As the larger of the two molecules, the solubility of CO_2 falls below that of helium at a density of $1250\,\mathrm{kg\,m^{-3}}$, equating to a pressure of approximately 300 MPa. Given their behaviour with increasing temperatures shown in Figure 5.11, this cross-over point could occur even sooner if both temperatures and pressures were raised concurrently, as they might be in an oil and gas drilling context.

The solubility of H_2O reaches zero at a density of $1600\,\mathrm{kg\,m^{-3}}$, or pressure of approximately 670 MPa, far beyond the conditions found in oil and gas wells where typically pressures reach 200 MPa and temperatures reach 225 °C [4–6]. This can be attributed to the virtual charges present in the SPC model of water on the hydrogen sites, and the lack of any LJ repulsion from these sites, with overlap being prevented largely by the central oxygen atom. The electrostatic attraction from the virtual charges appears to overcome the LJ repulsion up to large densities. This is supported by the observation that the solubility of H_2O without any partial charges is significantly lower. Electrostatics does not seem to be as big a factor for CO_2, suggesting that steric effects dominate in this case.

5.3 Summary

In this chapter, molecular simulation was used to investigate the solubilities of small molecules in NBR. The need for careful sampling when performing Widom insertion was demonstrated, for insertions performed randomly using the unbiased Widom insertion technique, as well as those performed in regions of free volume using the biased Widom insertion technique. Following examination of the various parameters, it was found that the biased Widom insertion technique provides a speed-up of a factor of 40 when compared to the unbiased Widom insertion technique, with no loss of precision in the calculated solubility to within the 5 % standard error found in both cases. These sampling tests were repeated in

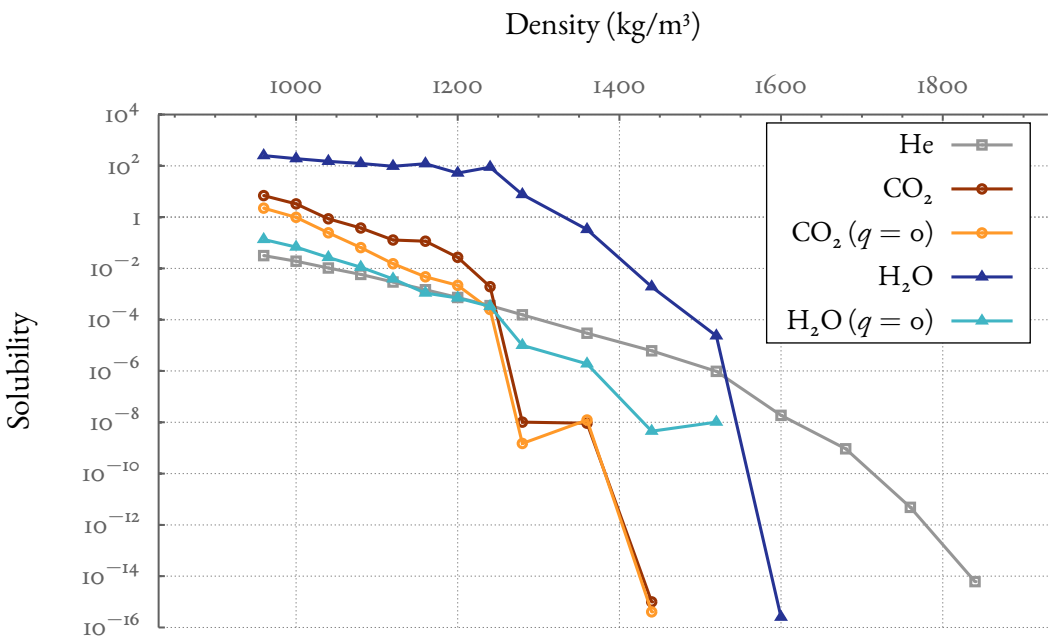


Figure 5.12: Solubilities of various gases as a function of density. Lines are shown to guide the eye, and are terminated when the solubility reaches 0 or the density reaches 1840 $\mathrm{kg\,m^{-3}}$, whichever comes first. Simulations performed at 25 °C for NBR of 41.3 % ACN content. Insertions performed using biased Widom insertion technique with 100 insertions per grid point defined as free volume, 10^6 grid points and $\alpha = 0.2$.

two systems at higher pressures (approximately 250 MPa and 500 MPa) to ensure convergence was maintained in cases where fewer successful insertions contribute to the solubility. No significant change in the solubility was observed.

As a co-polymer of ACN and butadiene, the monomer composition of NBR is often varied in industrial applications, e.g., increasing ACN content to increase mechanical stiffness. Gaining an understanding of how the solubilities of different gases are affected by these changes is of interest. In the 1940s Van Amerongen [71, 92] was the first to investigate through experiment the solubility of a few gases as a function of ACN content.

In this chapter I utilised molecular simulation to understand the possible causes of some of the trends observed in experiment. The effect of varying the ACN content was studied, and the trends of increasing solubility of CO_2 and helium were reproduced in qualitative agreement with experiment, while H_2O, for which no experimental data was available for comparison, demonstrated the highest solubility of all owing to its dipole moment. Precise values of the solubilities were systematically overestimated by a factor of 2 to 5, consistent with other Widom insertion simulations in the literature [100], a result often attributed to a combination of length-scale issues, e.g., due to the presence of voids in the real polymer that are on a length-scale larger than that studied in a typical molecular simulation, and deficiencies in the force-field, which the solubility is sensitive to.

To probe the enhanced absorption of polar gases in NBR, solubilities were computed according to the local atomic environment of sites selected by the gases. It was found that nonpolar gases followed a similar pattern, mirroring fairly closely the free volume distribution. Polar gases showed a clear bias towards being situated near the nitrogen sites of the elastomer, suggesting that electrostatics is the key reason for their enhanced solubilities.

Since NBR is commonly used in elastomer seals that are subjected to high pressures and temperatures, e.g., in an oil and gas exploration context, the solubility of gases at elevated temperatures and pressures was examined. It was found that raising the temperature affected different gases in different ways, increasing the solubility of helium but suppressing that of H_2O and CO_2. Increasing the pressure reduced the solubility of all gases, but did so at different rates, with the solubility of CO_2, for example, dropping below that of helium, but under pressures far exceeding those an elastomer might face in an oil and gas context. These results suggest that if both temperature and pressure were raised concurrently, how-

ever, as they typically would be in an industrial setting, this cross-over would occur even sooner.

This work is a first step towards understanding the trends in the solubility of small gases in NBR through molecular simulation. Since the cyano-group was shown to be a vital contributor to the enhanced solubility of polar gases, it is evidently a potential candidate for chemical modification in order to reduce the costly problems of elastomer seal swelling and explosive decompression.

6

Diffusivity in NBR

This chapter explores the diffusivity of small gases in NBR as a function of the chemical composition of the polymer, i.e., the ACN content. Van Amerongen [71, 92] was the first to investigate diffusivity in NBR through experiment, and found that with increasing ACN content the diffusivities of all gases studied were suppressed. Kucukpinar and Doruker [19] were the first to study diffusion of NBR through simulation, doing so at a fixed ACN content using a fluctuating polymer TST approach (described in section 3.3.2).

This chapter builds on the work of Kucukpinar and Doruker [19], extending their simulations to NBR of varying ACN content while using a dynamics approach instead of a Monte Carlo one. An overview of the MD method used is presented, in which the MSD of the gas molecules is tracked and used to compute the diffusivity. The computed diffusivity of all gases is found to decrease with increasing ACN content, agreeing with the experiments of Van Amerongen [71], while precise values are generally overestimated. The diffusivities are combined with the solubilities from chapter 5, to generate permeabilities that are also overestimated as compared with experiment. After some simplifying assumptions, an analytical solution to the diffusion equation is presented, and, combined with the computed permeabilities, used to provide an estimate of gas permeation into the elastomer seal on a macroscopic level.

6.1 Method

A 1000 monomer-long chain of NBR of varying ACN content is generated and equilibrated at SATP, as described in chapter 4. A small number of gas molecules ($N = 6$ in this case) are inserted into separate pockets of free volume, to improve statistics by sampling different regions of the polymer in the same simulation. The insertion positions are computed by performing 10^6 trial insertions with the unbiased Widom method described in section 5.1.2. Only insertions of energy less than $2k_B T$ are recorded, where $T = 25\,°C$. The insertions are then ranked by energy, and the lowest energy trial insertion is accepted.* For every subsequent insertion, if its position is more than 2 nm from all other accepted insertions, it too is accepted. This distance criterion is to ensure limited gas-gas interaction during the dynamics, since the diffusion coefficients of interest are defined in the dilute limit.

After a short 10 ps simulation under an NVT ensemble to equilibrate the temperature of the gas-polymer system, a 2 ns NVE simulation is run to allow the gas molecules to equilibrate, followed by a 16 ns NVE simulation over which the positions†‡ of the gas molecules are recorded every 25 fs. An NVE ensemble was used for dynamics to avoid the risk of the thermostat biasing the diffusion in any way (see Ref. [156] for a discussion). From the trajectories of the molecules the MSD may be computed as a function of time, and is calculated as an average over all molecules and all time origins. To compute over all time origins, the position of a given molecule at times t_o and $t_o + t$ is read from the trajectory, and the distance travelled in this time is computed. This is repeated for different values of t and t_o to obtain the average MSD as a function of t. In principle, this average could be computed

*When computing the solubility, it was found that 10^8 insertions were required with the unbiased Widom method to obtain a converged result. However, for the diffusion simulations, a converged solubility is not of interest — a reasonable insertion position is all that is required. It is not necessary to perform extra insertions to, for example, precisely find the lowest energy orientation of a CO_2 molecule inside the polymer, when, in a dynamical simulation, the molecule will rapidly leave that position.

†Centre of mass positions only.

‡By default, MD packages like LAMMPS operate using 'wrapped' co-ordinates, where if an atom crosses a periodic boundary, e.g., $x = 0$, it is placed back inside the cell through the opposite boundary, e.g., $x = L$ for a cubic supercell of length L. But for the diffusivity, the unwrapped position of the atom has to be used since the net distance travelled is required. This is done by tracking how many times each atom crosses each boundary.

over *all* possible combinations of t_o and t in the trajectory, i.e., as long as $t < 16$ ns. In practice, as $t \to 16$ ns, the number of samples of width t drops off, leading to large fluctuations in the MSD for large t. To resolve this, the maximum value of t is set to half the total trajectory time, i.e., 8 ns.

Once the average MSD as a function of time has been computed, the diffusivity is defined as

$$D = \frac{\langle \mathrm{MSD}(t) \rangle_{N,t_o}}{6t}, \tag{6.1}$$

where the ensemble average is over the $N = 6$ molecules and all time origins, t_o. In practice, the gas molecules exhibit anomalous diffusion over some timescale, where, instead of the MSD being proportional to t, it is described by some power law, i.e., proportional to t^a for diffusive exponent $a \neq 1$. This anomalous behaviour is due to the polymer inhibited motion of the gas molecules when trapped inside cavities, and is described as subdiffusion, i.e., $a < 1$. At longer timescales, with sufficient rare but large jumps between cavities, the trajectory begins to resemble a random walk. This is termed 'normal diffusion' and corresponds to $a = 1$. In the simulations presented in this chapter, the period of anomalous diffusion does not last longer than 1 ns, and so all diffusivities are calculated using the MSD from $t = 1$–8 ns. The entire procedure is repeated over a single snapshot taken from each of $n = 24$ independently generated initial configurations, equilibrated using the procedure described in section 4.1.3.

For helium and H_2O, the interatomic interactions were described using the OPLS [26] and SPC [148] force-fields, respectively. For CO_2, the EPM2 model [149] previously used to compute solubilities with a static Widom insertion technique could not be used for MD simulations as it has no bond-stretching or bond-bending terms.* Furthermore, constraint algorithms such as SHAKE [132] or RATTLE [157] cannot be applied to linear molecules such as CO_2, as their solutions become degenerate. The solution was to use a different force-field for CO_2 diffusivity simulations, from Myshakin *et al.* [158], which contains bond

*It was designed for Monte Carlo simulations in which CO_2 is treated as a rigid molecule.

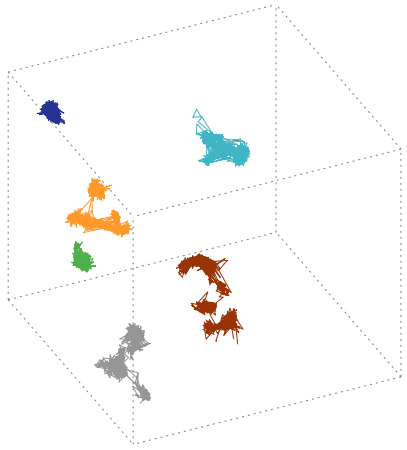


Figure 6.1: Diffusion of six molecules of H_2O through an NBR snapshot of 41.3 % ACN content over 16 ns. Each colour represents a different molecule, and only the centre-of-mass diffusion is shown.

distortion terms in its parameterisation.*

6.2 Results and discussion

6.2.1 Homogeneity and isotropy of diffusion

Figure 6.1 shows the motion of six H_2O molecules over 16 ns in a snapshot of NBR. There are visible differences in the distances traversed by different molecules, some of which do not appear to escape their initial cavities, while others clearly undergo multiple jump events. This sensitivity of the simulations to the initial positions of the gas molecules is due to inhomogeneity in the polymer, and highlights both the importance of using multiple gas molecules to properly sample the environment, as well as the need to perform an ensemble average over multiple independent configurations.

Figure 6.2 shows the diffusivity of H_2O in the x, y and z directions as a running average over the number of independent configurations,† It indicates the local anisotropy in the

*The rest of the parameters are very similar to EPM2 — partial charges remain the same, LJ terms are the same to within 5 %, and the bond length is the same to within 1 %. The full list of parameters is available in appendix A.

†The factor of 6 in Eqn. (6.1) is actually a factor of two times the number of dimensions, thus $D_x = \langle \mathrm{MSD_x} \rangle / 2t$, where $\mathrm{MSD_x} = |x_i(t) - x_i(0)|^2$ for molecule i, and equivalent relations apply to the y and z directions.

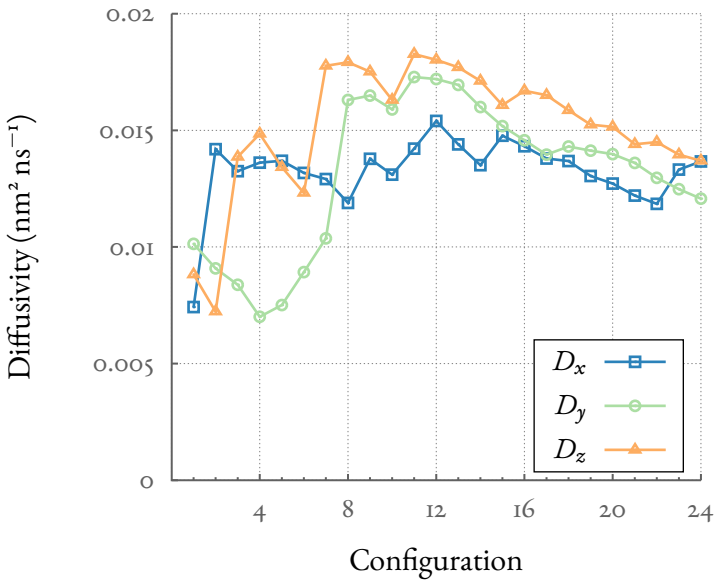


Figure 6.2: Diffusivity in x, y and z directions for H_2O in NBR of 41.3 % ACN content, at SATP, as a running average over $n \leq 24$ independent configurations. As a point of reference, the self-diffusion coefficient of H_2O (in 3D) is 2.57 $nm^2\ s^{-1}$ [159]. In terms of more commonly used units, 1 $nm^2\ s^{-1} = 10^{-5}\ cm^2\ s^{-1}$.

polymer,* particularly noticeable for small numbers of configurations, where the diffusivity in the x direction can be as much as three times the diffusivity in the y direction. After $n = 24$ configurations the anisotropy has been largely smoothed out, emphasising the need to sample multiple independent configurations.

6.2.2 Importance of polymer relaxation

Figure 6.3 shows the MSD of H_2O and helium in a particular snapshot of NBR, in both a normal snapshot where the polymer is able to relax, and a frozen snapshot, in which no polymer motion is allowed whatsoever. For both gases, when polymer motion is allowed, a rattle and jump type motion is evident. The rattling occurs when the molecule is trapped in cavities inside the polymer, and is visible as oscillations around a particular MSD value. The jumps occur when, due to a fluctuation in the polymer, a channel opens up between one cavity and the next, sufficiently wide for the gas molecule to hop through. They are

*Over large length-scales, the properties of an amorphous polymer should be isotropic.

noticeable as sudden shifts in the MSD value to a new value about which the MSD then fluctuates (albeit sometimes briefly), which corresponds to a switch back to the rattling type motion. For helium, jumps occur at noticeably shorter timescales as compared with H_2O, due to both its size advantage and its weaker interaction with the polymer.

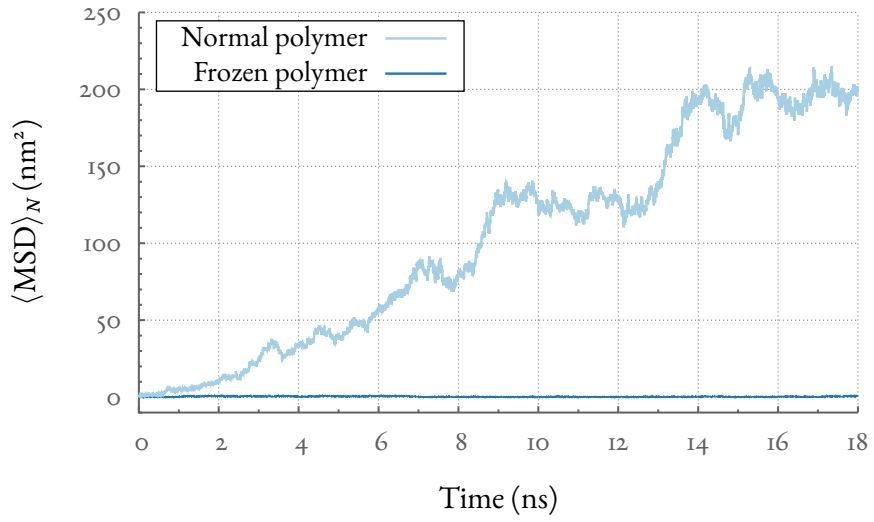
When the polymer is frozen, the MSD of both gases is dramatically lower, illustrating the importance of polymer relaxation to diffusion in NBR. These simulations are effectively a dynamical version of the frozen polymer TST simulations described in section 3.3.2, and serve to highlight the need for, at the very least, a fluctuating polymer TST method, if not a full dynamical model.*

6.2.3 Anomalous diffusion

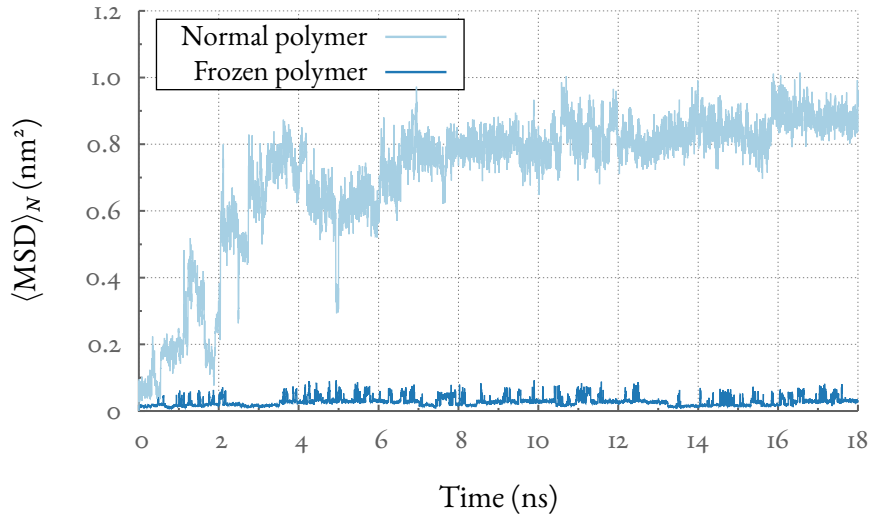
Figure 6.4 shows the MSD of CO_2 in a snapshot of NBR, averaged over all molecules and time origins, in which two distinct diffusive regimes are apparent. The diffusive exponent, a_i, is obtained for both regions by fitting to the MSD as a function of time using the relationship $\langle \text{MSD} \rangle \sim t^{a_i}$, where region $i = 1$ is from 0–1 ns and region $i = 2$ is from 1–8 ns. Over short timescales there is subdiffusion ($a_1 = 0.30$), corresponding to the rattling type motion that occurs due to the molecules being trapped in cavities in the polymer, followed by approximately normal diffusion ($a_2 = 0.95$) at longer timescales, once a sufficient number of jump events have been sampled.

The type of diffusion and the degree to which it is anomalous depends on the gas. This is shown in Table 6.1, in which the diffusive exponents have been calculated for a range of gases and averaged over multiple independent configurations. Due to its small size and weak interaction with the polymer, helium is able to make large jumps frequently, reaching the normal diffusion regime faster than other gases. CO_2 is the largest molecule out of those investigated, and clearly exhibits subdiffusion over short timescales. The limited difference between polar and nonpolar CO_2, i.e., with all partial charges set to zero, suggests that this is largely a steric effect, not an electrostatic one. H_2O is more anomalous than

*One advantage that the frozen polymer TST simulations have over the dynamical ones, however, is that, since they are Monte Carlo simulations that are performed on a discretised grid of atoms, it is substantially faster to generate trajectories in such simulations than it is when using MD. Although this just means that the ultimately underestimated diffusivity will have a smaller statistical error — it will still describe a system that is unphysical in the sense that it neglects polymer relaxation.



(a) He



(b) H_2O

Figure 6.3: Importance of polymer relaxation to diffusion for helium and H_2O. Either the polymer is allowed to move or it is frozen in place, while the MSD of the inserted gas molecules is tracked. MSD is computed as an average over all $N = 6$ molecules with one time origin, $t_o = 0$, to illustrate the rattle and jump motion.

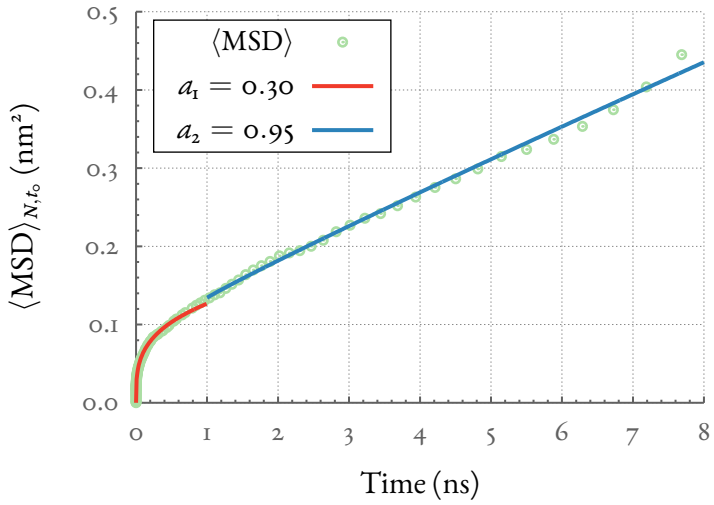


Figure 6.4: MSD for CO_2 in NBR of 32.2 % ACN content, averaged over all molecules and time origins. The fitted a_i exponents for the two diffusive regimes are shown.

Gas	a_1	a_2
He	0.91 ± 0.03	1.00 ± 0.10
CO_2	0.43 ± 0.06	0.95 ± 0.15
CO_2 $(q = 0)$	0.45 ± 0.06	0.97 ± 0.13
H_2O	0.40 ± 0.07	0.89 ± 0.13
H_2O $(q = 0)$	0.56 ± 0.05	0.95 ± 0.09

Table 6.1: Exponents for anomalous (a_1) and normal (a_2) diffusion in NBR for different gases. Averaged over 24 independent configurations. Uncertainties in a are expressed as standard deviations.

CO_2, but in this case electrostatics appears to be responsible, judging by the pronounced difference in exponents between polar H_2O and nonpolar H_2O, which is more normal. This can be rationalised by referring back to the solubility simulations (section 5.2.2), in which it was found that polar H_2O had by far the highest solubility of the five gases, due to its strong preference to sit near nitrogen sites in the elastomer. This affinity results in H_2O becoming physically bonded to the polymer,* and its diffusion being less random and more anomalous than, e.g., CO_2.

*No chemical change is possible during these simulations.

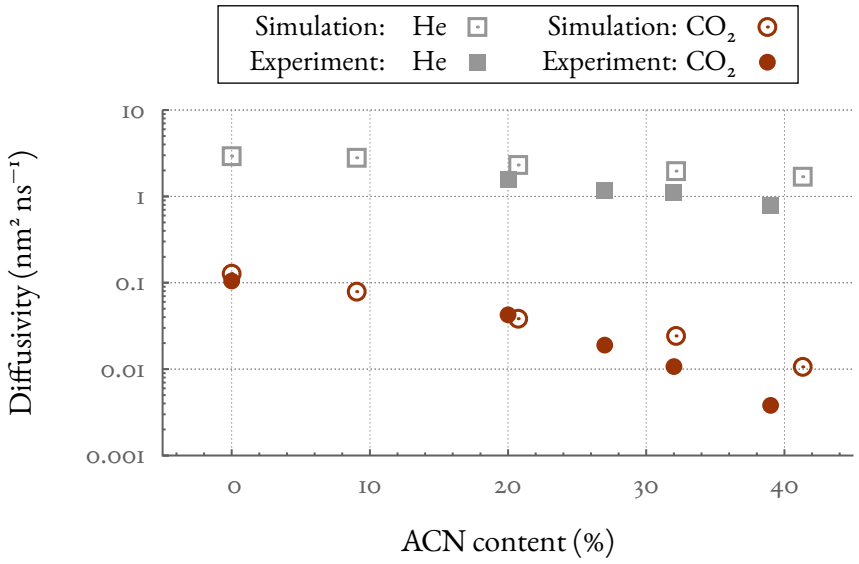


Figure 6.5: Diffusivity of helium and CO_2 as a function of ACN content from simulation and experiment. Experimental data from Van Amerongen [71] for NBR at SATP.

6.2.4 Effect of acrylonitrile content on diffusivity

Figure 6.5 shows a comparison between computed and experimental diffusivities as a function of ACN content.* Error bars are not shown for the computed values, but the maximum standard error was 13 % for CO_2 and 5 % for helium. Overall, both in experiment and in these simulations, there is a general trend towards decreasing diffusivity with increasing ACN content. Van Amerongen [71] attributes this to the increased number of polar cyano groups increasing the cohesive energy of the polymer. This would make it harder for channels to open up between cavities, to enable gas molecules to jump from one to another. The fact that the larger molecule, CO_2, exhibits a greater drop off in diffusivity with increasing ACN content and therefore increasing cohesive energy, further supports this conjecture.

Unsurprisingly, given the vast difference in size, the relative ordering between the diffusivities of helium and CO_2 is reproduced, i.e., $D(\mathrm{He}) > D(\mathrm{CO_2})$ for NBR of any ACN content. Qualitatively, the simulated diffusivities range from a factor of 0.9 to 2.8 times the

*Among the gases studied, only helium and CO_2 have experimental data to compare to.

Gas	This work	Kucukpinar and Doruker [19]
He	1.7	1.88
CO_2	0.019	0.013
H_2O	0.0085	0.010
H_2O ($q = 0$)	0.041	0.014

Table 6.2: Comparison between diffusivities in this work and those obtained by Kucukpinar and Doruker [19]. This work: MSD tracked over 16 ns MD simulations, with 24 independent configurations of NBR of 41.3 % ACN content and 1000 monomers. Kucukpinar and Doruker: MSD tracked using fluctuating polymer TST method over 1000 trajectories, with 3 independent configurations of NBR of 39 % ACN content and 164 monomers.

experimental diffusivities, and are generally overestimated. This was also the case with the computed solubilities in chapter 5, and a similar explanation applies here. The accuracy of the force-field is questionable, since the non-bonded terms that govern the interaction between the gas and the polymer have been systematically tuned to reproduce bulk material properties, such as density and heat of vaporisation. There are also questions over whether the time- and length-scales used in these simulations are sufficient to reproduce experimental results.

As with the density (section 4.3.1), the agreement between simulation and experiment worsens with increasing ACN content. For the density this was attributed to issues in the OPLS force field, which is parameterised for acetonitrile but not ACN, and therefore as the ACN content increases this becomes increasingly noticeable. This could equally affect the diffusivity.

Table 6.2 shows a comparison between the diffusivities computed in this work and those obtained by Kucukpinar and Doruker [19] in their simulations. While the agreement is broadly reasonable, the most noticeable difference is in the diffusivity of nonpolar H_2O, which in my simulations has a diffusivity nearly five times higher than that of polar H_2O, whereas in Kucukpinar and Doruker's simulations the diffusivity of nonpolar H_2O is only 40 % higher than that of polar H_2O. Since they have used COMPASS, a force-field with hidden parameters, it is not possible to definitively isolate the source of this discrepancy.

One issue could well be the H_2O force-field parameters. In the SPC force-field [148] that I have used, the hydrogen sites in H_2O are only virtual point charges, i.e., they have no mass and no LJ interaction with any atoms. With these charges set to zero in nonpolar H_2O, the

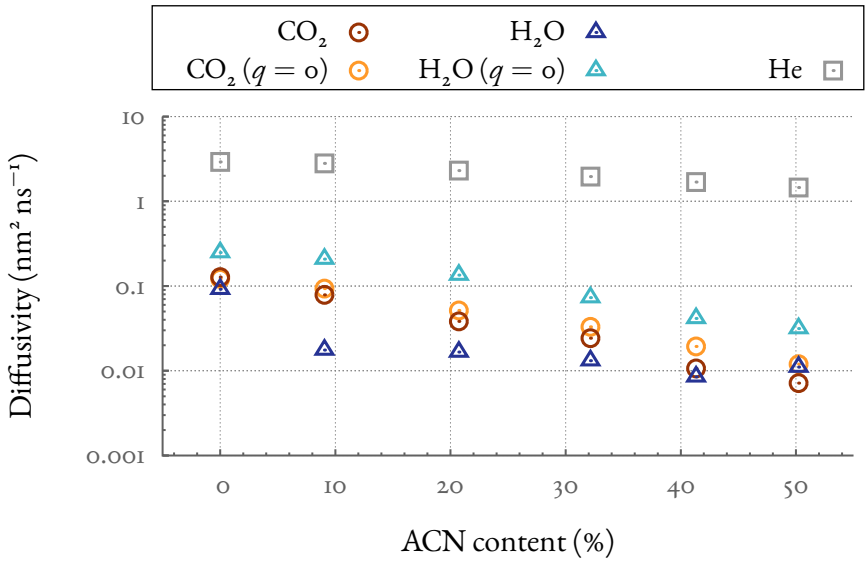


Figure 6.6: Computed diffusivities in NBR as a function of ACN content, at SATP.

molecule is effectively just an oxygen atom. If the hydrogen atoms in H_2O in COMPASS have nonzero LJ parameters, this would alter the van der Waals diameter of the molecule as a whole. Since the diffusivity is sensitive to molecular size, this could explain the reduced diffusivity of nonpolar H_2O in Kucukpinar and Doruker's simulations.

Another issue is that of sampling. The spread in the diffusivities that I have obtained is relatively large, and to improve the precision it was necessary to use 24 independently generated configurations of the 1000 monomer-long chain. In Kucukpinar and Doruker's simulations, although they used a Monte Carlo approach in which they were able to generate 1000 separate trajectories for a given configuration, they used a total of three independent configurations, each consisting of a single chain of 164 monomers. As shown earlier, even at the ensemble sizes that I have been studying the polymer is inhomogeneous and anisotropic, and therefore with an even smaller ensemble size this could potentially be problematic, and result in a large spread in diffusivities. Since uncertainties in the diffusivity were not reported by Kucukpinar and Doruker, however, this cannot be confirmed.

Figure 6.6 shows the computed diffusivity as a function of ACN content for different gases, and includes the results for helium and CO_2 shown in Figure 6.5, as well as nonpolar CO_2, H_2O and nonpolar H_2O. There is once again a general trend of diffusivity decreasing

for all gases with increasing ACN content. The diffusivity of H_2O drops off rapidly once ACN monomers are included in the polymer. Nonpolar gas molecules have higher diffusivities than their polar versions — slightly so for CO_2 but markedly so for H_2O.

To investigate this further, an analogous procedure to the one developed in section 5.2.2 was used to study the local atomic environment of gas molecules diffusing within the polymer. Following a 2 ns equilibration as described previously, the nearest atomic neighbour in the polymer of each each gas molecule is computed every 0.1 ps, for a total of 16 ns. Once more, hydrogen atoms are ignored in this analysis, and the atomic sites are grouped by atomic orbital hybridisation, i.e, sp^1, sp^2, sp^3 carbons and nitrogen. Unlike the method used in section 5.2.2, in this case a Voronoi decomposition was not used owing to reasons of computational expense — instead a distance search was found to be more efficient in locating the nearest neighbour of an inserted gas molecule.* The resulting per-atom-type residence times in fractional form, averaged over eight independently generated and equilibrated configurations, are shown in Figure 6.7, and are similar to the per-atom-type solubilities shown in Figure 5.10. These observations further support the hypothesis that the cyano group of the ACN monomer is acting as a binding site for polar gases, reducing their overall mobility.

6.2.5 Effect of acrylonitrile content on permeability

Having computed diffusivities and solubilities in NBR, permeabilities (P') can be calculated through the solution-diffusion model:

$$P' = Ds\,, \tag{6.2}$$

where, unlike Eqn. (3.28), the permeability here is expressed in terms of the dimensionless solubility, not the experimental solubility ($sT_\circ/P_\circ T$).

*The Voronoi approach requires computing the Voronoi cell of each atom in the polymer. For the solubility, tens of thousands of gas positions were binned using a single Voronoi decomposition. For the diffusivity, however, each decomposition can only be used to bin the positions of the six gas molecules, and has to be recomputed every 0.1 ps. Due to the overhead in computing the Voronoi cell, performing a distance search between each gas molecule and every atom in the polymer was faster.

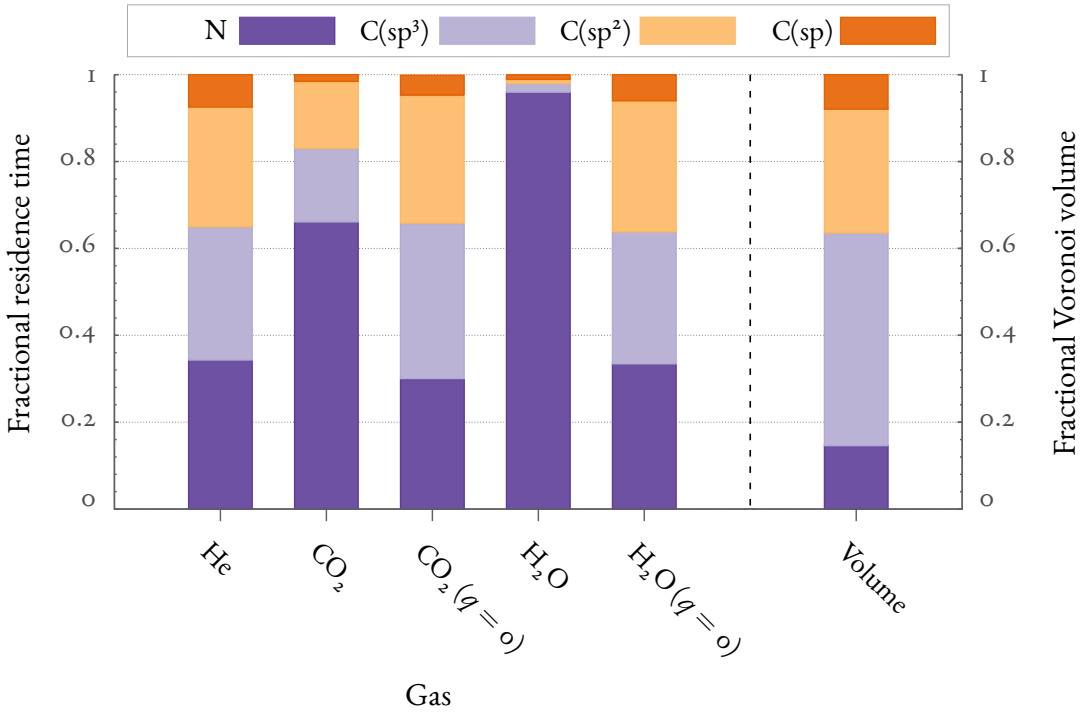


Figure 6.7: The trajectory for each gas decomposed into fractional contributions according to the residence time in a particular atomic environment. The fractional Voronoi volumes associated with each atomic environment, computed in chapter 5, are shown on the right as a point of reference. NBR of 41.3 % ACN content generated at SATP.

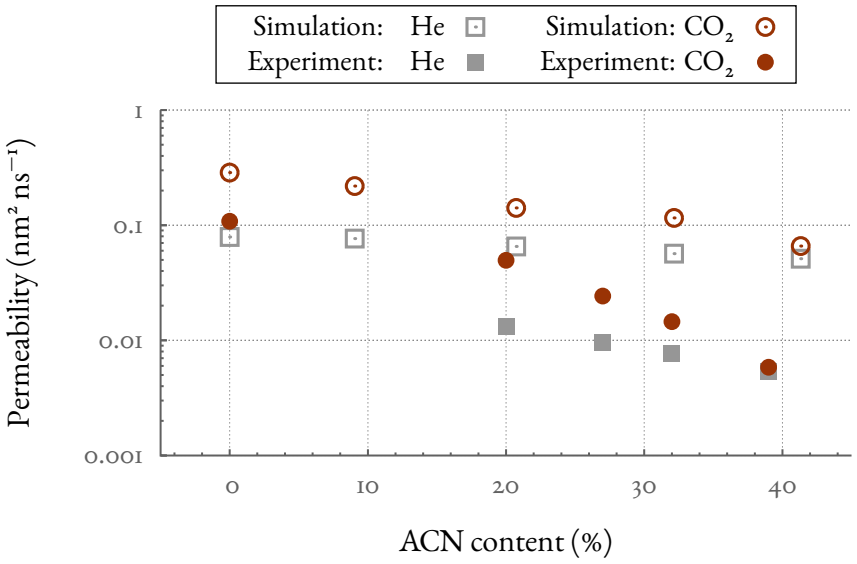


Figure 6.8: Permeability of helium and CO_2 as a function of ACN content from simulation and experiment. Experimental data from Van Amerongen [71] for NBR at SATP.

Figure 6.8 compares computed and experimental permeabilities, as a function of ACN content.* The experimental trend of decreasing permeability with increasing ACN content is reproduced. Precise values are overestimated with respect to experiment, due to the solubilities and diffusivities almost always being overestimated themselves. Figure 6.9 shows the computed permeability across different gases, as a function of ACN content, and includes the results for helium and CO_2 shown in Figure 6.8, as well as nonpolar CO_2, H_2O and nonpolar H_2O. With the exception of H_2O in amorphous polybutadiene (0 % ACN), polar gases have higher permeabilities than nonpolar ones, meaning that their higher solubilities (Figure 5.9) are able to overcome their lower diffusivities. H_2O is the only gas to show consistent increases in permeability with ACN content. Its exponential increase in solubility in NBR is able to overcome the decrease in diffusivity.

*Although previously computed using the EPM2 force-field [149] in chapter 5, CO_2 solubilities (both polar and nonpolar) were re-computed using the force-field of Myshakin *et al.* [158] when inferring permeabilities, to ensure consistency with the parameters used to obtain diffusivities.

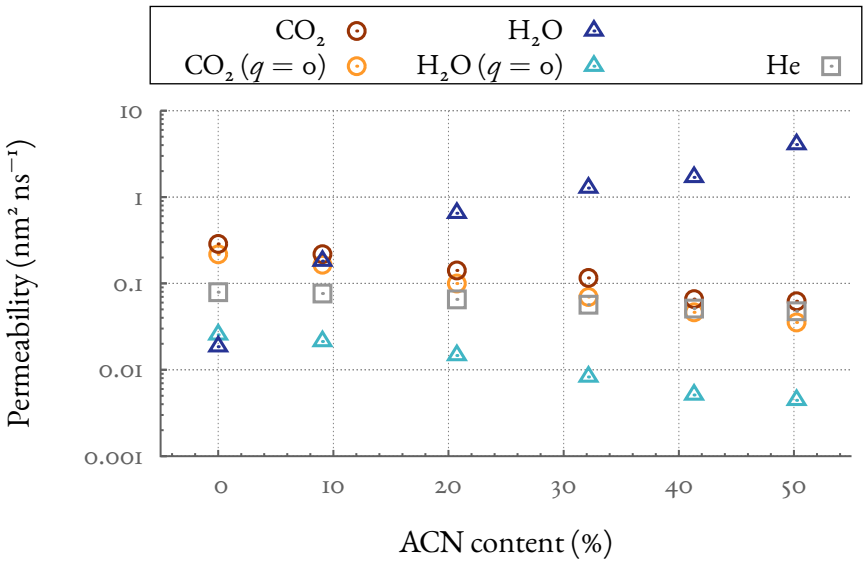


Figure 6.9: Computed permeabilities in NBR as a function of ACN content, at SATP.

6.2.6 Macroscopic picture

It is important to relate the nanoscale computational results obtained in this thesis to the macroscopic picture, to see what can be deduced about gas behaviour in elastomer seals in an oil and gas exploration context. As discussed in chapter 2, Baker Hughes are concerned about two main failure modes — permeation through the entire seal and explosive decompression — which lead to either damage of sensitive electronic components previously under protection by the seal or outright tool failure. There are a number of questions that these permeability results can begin to answer.

How much gas enters the seal during a drilling operation that might last, e.g., a month? The pressure of gas inside the seal is what drives the rupture. Gent and Lindley [160] proposed that the critical pressure, p_c, required to infinitely expand a small spherical cavity in an initially undeformed and isotropic material was related to the Young's modulus of the polymer, E, by

$$p_c \approx \frac{5}{6} E \,. \tag{6.3}$$

Does the internal pressure exceed this value?

How far do gases penetrate? This is important for two reasons. Firstly, since everything is permeable give a long enough timescale, is the seal not as impermeable as has been assumed, when accounting for the duration of the drilling operation? This would mean corrosion damage to components would be almost inevitable. Secondly, the further gases enter the seal over the drilling operation, the further they have to travel to escape when the drill string is raised and the external pressure is relieved. This could result in more internal damage to the elastomer.

To examine these questions, the permeabilities obtained through simulation can be utilised to estimate the concentration of gas in the seal as a function of time. In general, the concentration $c(x, t)$ at position x and time t is described by Fick's second law in one dimension [89]:

$$\frac{\partial c}{\partial t} = D \frac{\partial^2 c}{\partial x^2} \,, \tag{6.4}$$

where D is the diffusivity.* Assuming the seal to be a semi-infinite medium that begins at $x = 0$, with boundary conditions $c(x = 0, t) = c_0$, $c(x, t = 0) = 0$ and $\frac{\partial c}{\partial x}|_{x=\infty,t} = 0$, the concentration at $x \geq 0$ is [161]:

$$c(x, t) = c_0 \operatorname{erfc}\left(\frac{x}{2\sqrt{Dt}}\right) , \tag{6.5}$$

where $\operatorname{erfc}(x)$ is the complementary error function, defined as

$$\operatorname{erfc}(x) = \frac{2}{\sqrt{\pi}} \int_x^\infty \exp(-b^2)\, db\,. \tag{6.6}$$

Using Henry's law, the initial concentration immediately inside the surface of the membrane at c_0 is defined in terms of the vapour concentration outside the membrane, c_v, using the solubility, s, as

$$c_0 = s\, c_v\,, \tag{6.7}$$

as shown in Eqn. (3.18). Therefore Eqn. (6.5) can be written as

$$\frac{c(x, t)}{c_v} = s \operatorname{erfc}\left(\frac{x}{2\sqrt{Dt}}\right) , \tag{6.8}$$

Effectively, diffusion through the seal is determined by the diffusivity and the concentration of gas immediately inside the seal, which itself depends on the diffusivity and the vapour concentration.

For an ideal gas, i.e., one for which $pV = Nk_B T$ or $c = N/V = p/k_B T$, relative pressures and relative concentrations are equivalent. Hence Eqn. (6.8) can also be written in terms of pressure as

$$\frac{p(x, t)}{p_v} = s \operatorname{erfc}\left(\frac{x}{2\sqrt{Dt}}\right) . \tag{6.9}$$

*This can be derived from Fick's first law, Eqn. (3.11), by applying the principle of mass conservation, i.e., $\frac{\partial c}{\partial t} = -\frac{\partial J}{\partial x}$.

Figures 6.10a, 6.10b, 6.10c and 6.10d show the relative pressure in NBR of 41.3 % ACN content at SATP as a function of time and position, for helium, CO_2, H_2O and O_2, respectively. The x axis of each graph has been terminated at 1 cm, a typical width of a seal.

The high permeability of helium leads it to saturating the seal quickly, relative to CO_2 and H_2O. Since $s \ll 1$ for helium, the pressure inside the membrane is strongly suppressed with respect to the vapour pressure.

CO_2 is the slowest of the three, taking over a year to approach the equilibrium pressure.* How much CO_2 diffuses into the seal within 1 day is equivalent to how much CO_2 can escape when the ambient pressure is relieved over approximately 1 day, as the drill string is raised.† However, the seal may be downhole for 30 days, and therefore there is a significant mismatch between the gas absorbed over this period and the gas that can be dissipated within 1 day. Since the Young's modulus determines when rupture begins, as shown in Eqn. (6.3), and the Young's modulus of NBR is approximately eighty times atmospheric pressure [2], for low pressures CO_2 should not cause damage to the seal. When p_v increases as the drill string is lowered, though, this could become an issue. However, as this happens, the permeability will decrease, as shown in Figure 6.9. This trade-off between increasing pressure and decreasing permeability is critical to understanding and predicting swelling damage to elastomers. If the SATP permeability were used to describe gas behaviour at downhole pressures, thousands of times higher than atmospheric pressure, decompression would seem inevitable. As NBR seals are used extensively in oil and gas exploration, and their rate of failure due to decompression is nowhere near 100 %, this clearly is not the case.

H_2O is faster than CO_2, saturating most of the seal within a month. While it would therefore be able to escape faster than CO_2 when the external pressure is relieved, the internal pressure would in fact be higher due to its high solubility. Its high permeability means that corrosion damage is a real possibility, depending on the trade-off between pressure and permeability. The other factor in corrosion is O_2, which has not been simulated in this work, but for which experimental data is available from Van Amerongen [71]. Van

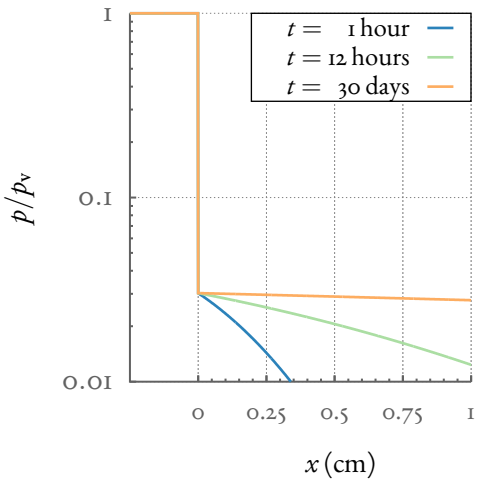
*Since $\operatorname{erfc}(1/t) = 1$ only as $t \to \infty$ it will never reach the equilibrium pressure, $s\,p_v$, of course. However, it is worth highlighting the fact that even after a year there is a noticeable difference between the pressure at $x = 1$ cm and the equilibrium pressure.

†Effectively this equates to switching the initial boundary conditions, such that the pressure at the boundary is now held at zero and the initial pressure inside is p_v, reversing the diffusion.

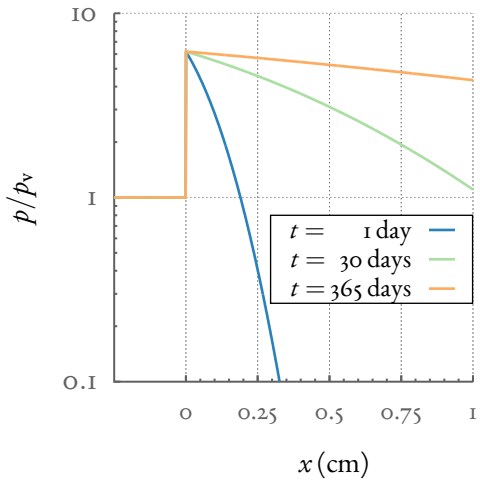
Amerongen found that the permeability of O_2 is approximately ten times lower than that of CO_2, due to the combination of its higher diffusivity and significantly lower solubility. Figure 6.10d shows that this combination leads to a suppressed internal pressure, with a small amount of gas reaching the $x = 1$ cm face of the seal.

As discussed in section 2.3.1, this simplified model has its limitations, since it ignores other factors that would affect diffusion. For example, the presence of gas molecules in the elastomer are known to have a plasticising effect on the material, thereby increasing the local mobility of the gas molecules, causing a plasticising effect elsewhere etc. Thermal gradients may also be present across the seal, as the temperature in the drill string fluctuates during the drilling operation. Meanwhile, the material is constantly subjected to sources of external stress, from the high geostatic pressures found downhole to the frequent shocks resulting from bombardment by rock cuttings. The material is also subject to sources of internal stress in the form of filler particles, which make up a significant proportion of the elastomer. Ideally, a model is required that accounts for all of these effects and the coupling between them.

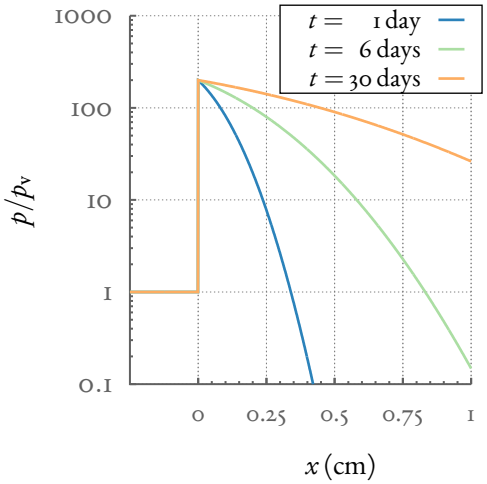
Another issue is that permeabilities at elevated pressures were not used in this work, merely those at SATP. It was not possible to do so since, although solubilities at elevated pressures in NBR were computed, diffusivities were not. These were not computed because, as shown in Figure 6.11, the dynamical approach used thus far is not applicable to systems with high densities. In these cases, free volume is limited, and the time between jumps between cavities is increased. This means a longer simulation is required to observe the normal diffusion mode, and, given the lack of mobility that the gas molecules exhibit over 16 ns, as Figure 6.11 shows, this would be prohibitively long. One approach to resolving this may be to use a TST method in which polymer fluctuations are allowed. Although the results will be sensitive to the parameter controlling the dampening of the fluctuations, it takes substantially less computational expense to generate long trajectories via a Monte Carlo method than via MD. This was deemed to be beyond the scope of this work, but represents a potential avenue for further study.



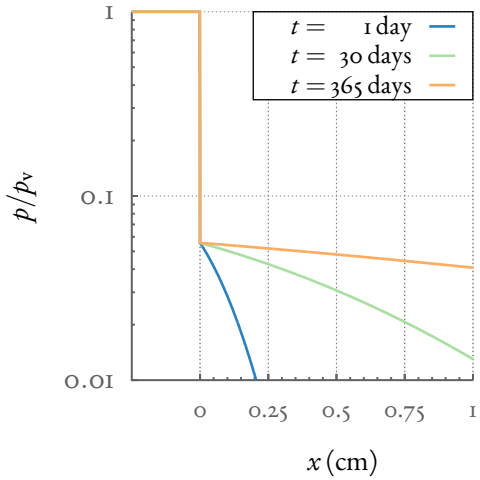
(a) Helium



(b) CO_2



(c) H_2O



(d) O_2

Figure 6.10: Permeation of different gases through semi-infinite NBR of 41.3 % ACN content, between $0 \leq x \leq 1$, using solubilities and diffusivities from simulation for helium, CO_2 and H_2O, and experimental values from Van Amerongen [71] for O_2. Data from both simulation and experiment obtained at SATP. Pressure is expressed relative to the pressure of the vapour phase, $p(x < 0, t) = p_v$.

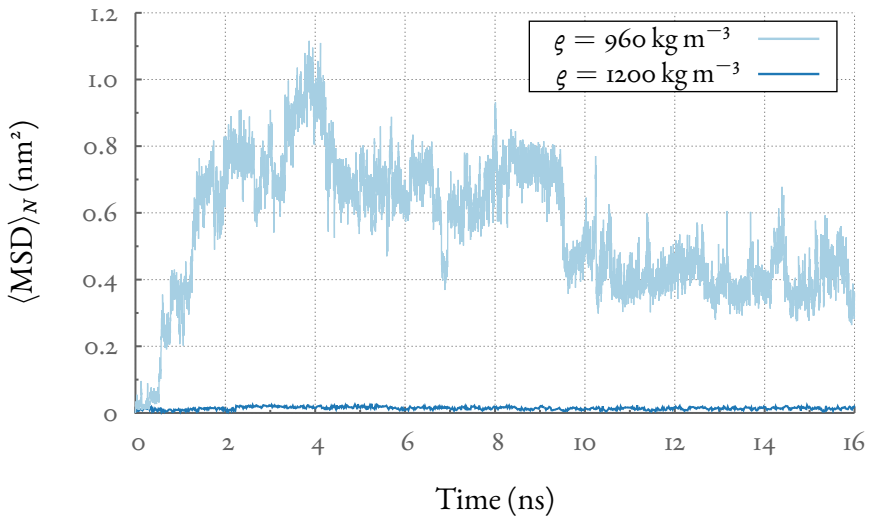


Figure 6.11: MSD in NBR of 41.3 % ACN content, at two different densities, ϱ, where $\varrho = 960\,\mathrm{kg\,m^{-3}}$ corresponds to the density at SATP. At a high density it is not possible to observe diffusion using a dynamical approach, over computationally accessible timescales.

7

Permeability in HNBR

Hydrogenated nitrile butadiene rubber, or HNBR, is a highly saturated form of NBR, formed by selective hydrogenation of the carbon-carbon double bonds present in the butadiene monomers. The main advantage HNBR offers over NBR is its better resistance to thermal degradation. Limited experimental data is available in the literature on the permeability of gases through HNBR. What data is available usually comes in the form of data sheets from manufacturers, where the permeabilities depend on the particular formulation used, e.g., quantity of fillers, degree of cross-linking etc. For intellectual property reasons, manufacturers do not reveal the precise formulations that they use. This renders it difficult to compare results from different manufacturers to one other, and to extract any meaningful trends for the base polymer.

In this chapter I use simulation to predict the solubility and diffusivity of a few small gases in HNBR: helium, CO_2 and H_2O. To generate a molecular representation of HNBR, NBR is selectively hydrogenated and cross-linked based on a user-defined cross-link fraction. This model is verified by examining bulk properties such as density, bulk modulus and glass transition temperature, and is then used to compute solubilities as a function of cross-link fraction. While the diffusivity falls with increasing cross-link fraction, at the same

time, somewhat surprisingly, the solubility of all gases that were tested *increases*. The reasons for this are investigated and a potential explanation is proffered.

7.1 Method

7.1.1 A molecular model for HNBR

A single chain of NBR consisting of 1000 monomers, with 41.3 % ACN content, is generated and equilibrated at SATP, as described in section 4.1.2. Carbon atoms that form part of unsaturated C=C double bonds are then stochastically cross-linked depending on a user-defined cross-link fraction. Candidate carbon atoms that are not selected for cross-linking are hydrogenated, such that the resultant structure is fully saturated. The structure is then passed into the same equilibration routine that was used for NBR, described in section 4.1.3.

This is a static cross-linking method, in which all cross-linking is performed on a frozen snapshot of the polymer, with no relaxation allowed until after the curing is complete. Similar methods have been applied across the simulation literature to cross-link various polymers (e.g., Refs. [128, 129, 162]), but Molinari [25] was the first to apply such a technique to HNBR.*

The details of the procedure are as follows. The cross-link fraction, f_{cl}, is defined by the user. This is a relative number density, defined in terms of the ratio of the number of successfully cross-linked sites desired to the number of potential candidates (i.e., the number of C=C bonds). The potential cross-link candidates, i.e., all sp^2 carbons,† are put into a list and randomly shuffled.‡ A candidate carbon site is chosen, and a random number R_N in the

*As this was a collaborative study between Molinari and myself, it is worth clarifying the attribution of the work in this chapter. The static cross-linking method described in this section was devised by Molinari, and builds upon the model I have developed for NBR, presented in chapter 4. Although Molinari's source code is freely available [163], I have reimplemented the algorithms myself for reasons of computational performance. In section 7.2.1 I have extended Molinari's method to account for dynamic cross-linking. I have obtained all of the results presented in this chapter myself, with the exception of the glass transition temperature as a function of cross-link fraction, shown in Figure 7.4, which was computed by Molinari.

†For a 1000 monomer long chain of NBR of 41.3 % ACN content, this corresponds to 1174 atoms.

‡This shuffling is designed to remove any non-physical bias towards cross-linking neighbouring carbons, that might otherwise be close to one another on the list due to the atom numbering convention following the ordering along the backbone.

range $(0, 1]$ is generated from a uniform distribution.

If $R_N > f_{cl}$, the carbon atom and the sp^2 carbon that it is bonded to are hydrogenated. Hydrogenation is performed by placing a hydrogen atom at a distance of 0.109 nm* from the carbon atom in a randomly chosen direction, with the expectation that the equilibration routine will correct for any steric overlap and choose the optimal position. The pair of carbon atoms are then converted into sp^3 carbons, and all bonding information is amended accordingly (bonds, angles, dihedrals), since the parameters for these interactions depend on the hybridisation of the atomic orbitals.

If $R_N \leq f_{cl}$, cross-linking is attempted by searching for other sp^2 carbon atoms within a radius of 0.5 nm. If any candidates are found, the closest one is then connected via a covalent bond to the original carbon atom, and the remaining pair of carbons from the two corresponding C=C bonds are hydrogenated. All four carbons are converted into the sp^3 type, and the bonding information is updated. If no candidates are found the pair of carbons are hydrogenated as described before. The process is depicted in Figure 7.1, and is repeated until full saturation,† before the structure is equilibrated using the procedure described in section 4.1.3.

Since the cross-linking is performed probabilistically, in practice it is rare for the true cross-link fraction, F_{cl}, to be equal to the target cross-link fraction, f_{cl}, as shown in Figure 7.2. This is particularly noticeable when attempting 100 % cross-linking, since, as more C=C bonds get cross-linked, the chances of finding an uncrosslinked one within 0.5 nm decreases. In my simulations, the upper bound for F_{cl} was found to be approximately 82 %. In practice, such high cross-link densities are not used anyway, since HNBR would effectively be more resin than elastomer. Nevertheless, it is instructive to consider the material and transport properties to high degrees of cross-linking in order to establish trends.

7.1.2 Validation of the model

In this section, the molecular model for HNBR is validated by computing bulk properties. Figure 7.3 shows the density of HNBR as a function of cross-link fraction, and the density

*Corresponding to the $C(sp^3)-H$ bond distance in OPLS.

†The saturation of commercial formulations of HNBR is typically close to 100 % [164] too, and thus this method mimics the peroxide curing technique used to generate HNBR in practice.

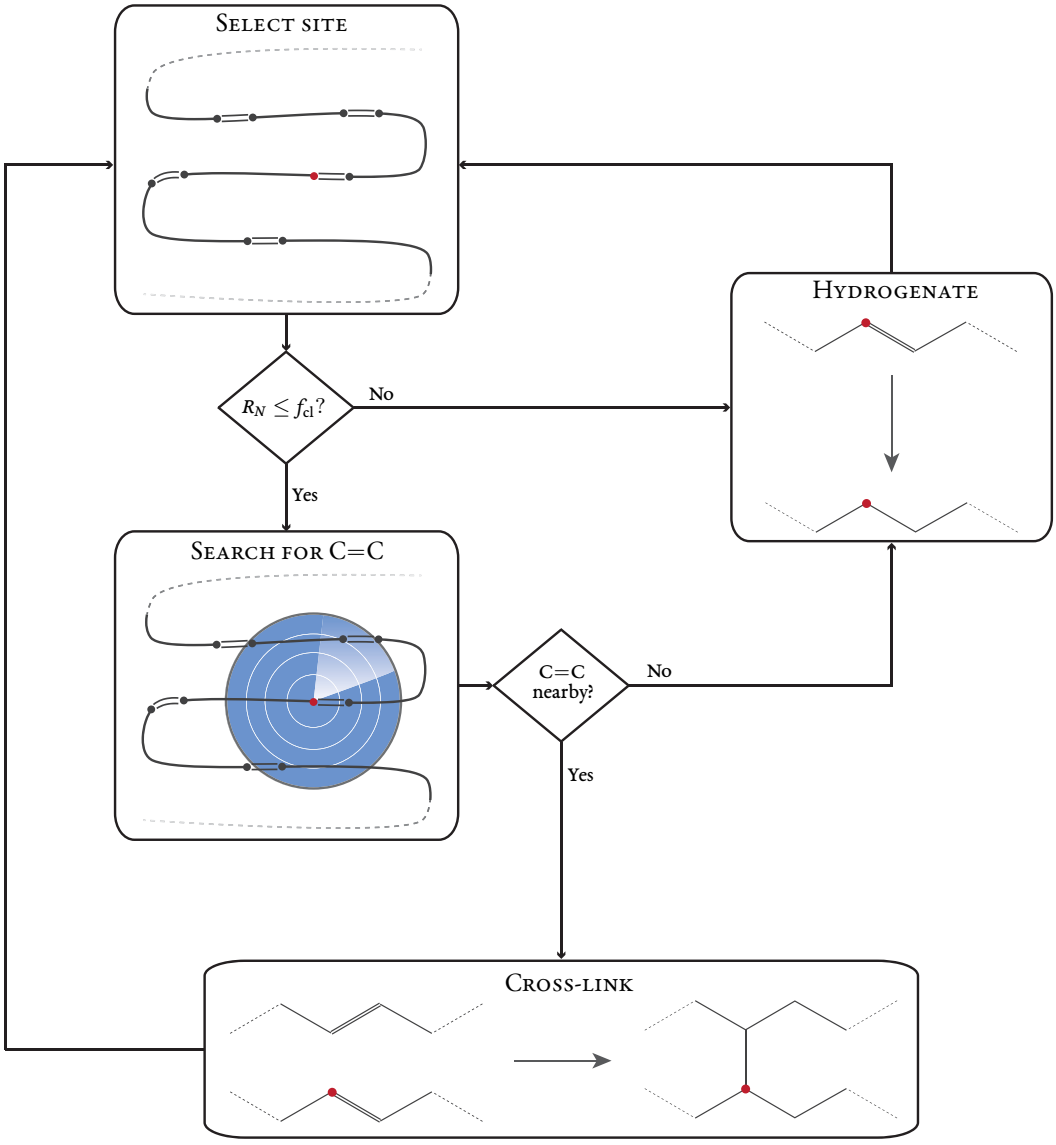


Figure 7.1: Static cross-linking procedure for user specified target cross-link fraction, f_{cl}, to generate HNBR from NBR. Potential cross-linking sites in the polymer are identified (all sp^2 carbon atoms). If a randomly generated number, R_N, is greater than f_{cl}, then both carbon atoms in the C=C bond are hydrogenated. Otherwise, a search is performed for any nearby sp^2 carbon atoms. If the nearest atom is within $0.5\,nm$, then the pair of atoms are cross-linked, and the remaining two carbon atoms from the two C=C bonds are hydrogenated. The cross-linking procedure ends when all sp^2 carbon atoms have been either cross-linked or hydrogenated, i.e., when the polymer is $100\,\%$ saturated.

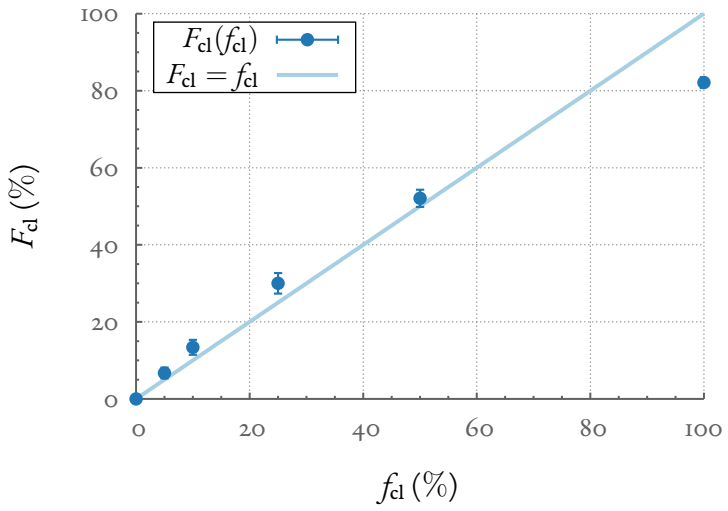


Figure 7.2: True cross-link fraction, F_{cl}, as a function of target cross-link fraction, f_{cl}. Each data point computed over 100 independently generated, equilibrated and cross-linked structures. Error bars represent the standard deviation from the mean. To guide the eye, the $F_{cl} = f_{cl}$ line is also shown. Since f_{cl} is a target cross-link fraction, used to stochastically generate configurations, it is possible to obtain systems with $F_{cl} > f_{cl}$.

of the NBR of 41.3 % ACN content from which the HNBR was generated. The density was computed as described in section 4.3.1, over eight independently generated and equilibrated structures. With the exception of $F_{cl} \approx 82\,\%$, HNBR has a lower density than NBR. One reason for the lower density is the additional hydrogen atoms in HNBR,* whose presence increases the average intra-chain separation. Another factor is that the C−C bonds that replace all the C=C bonds during the cross-linking procedure are longer and less stiff.†

There is a clear trend of increasing density with cross-link fraction, which is due to the fact that the cross-linking process introduces stiff, short and permanent covalent bonds between parts of the chain that previously interacted largely through weak, long-ranged and fluctuating van der Waals forces. Also, with increasing F_{cl}, fewer hydrogen atoms are added to the system.

The available experimental data is limited, except at $F_{cl} = 0\,\%$, for which one manufacturer [18] reports a density of 960 kg m^{-3} for HNBR of 39 % ACN content, compared to

*For example, at $F_{cl} = 0\,\%$, for NBR of 41.3 % ACN content and 1000 monomers, 1174 hydrogen atoms are added to the system, corresponding to an increase of 13 % in the total number of atoms.

†In OPLS, the C−C bond is approximately 14 % longer than the C=C bond and has half the stiffness.

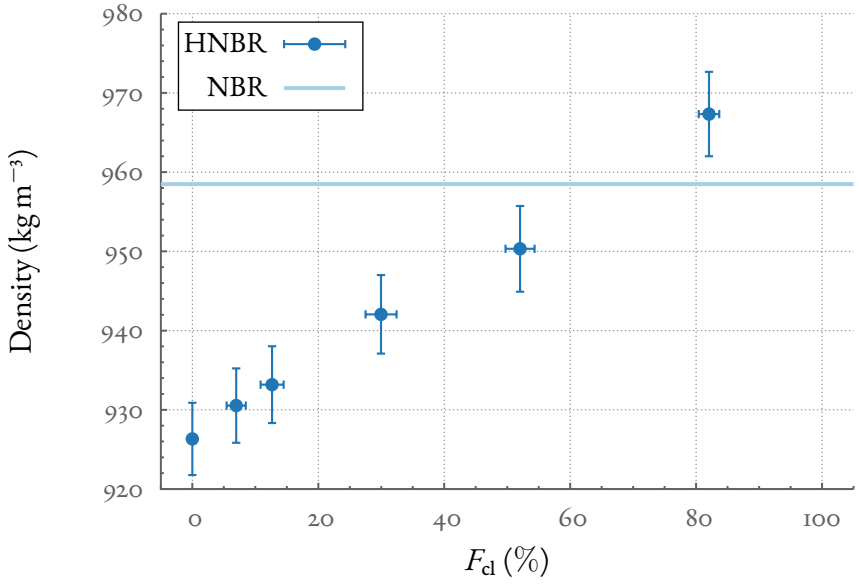


Figure 7.3: Computed densities for HNBR (41.3 % ACN content) and the NBR from which it was generated, at SATP. Error bars represent standard deviation.

the computed density of (926 ± 5) kg m^{-3} for HNBR of 41.3 % ACN content, where the uncertainty is the standard deviation. This slight underestimation of the experimental density (by 3.4 %) was also found for NBR in section 4.3.1, and can be attributed to a combination of the force-field being parameterised for the liquid form of subunits of the monomers (e.g., liquid acetonitrile instead of polyacrylonitrile), and the experimental formulation containing additives not present in these simulations.* The latter issue is particularly pertinent when comparing to manufacturer data sheets, instead of to the academic literature as was possible with NBR, since commercial formulations will typically contain far more additives than those used in the lab. Furthermore, the exact formulation is not available.

Figure 7.4 shows the glass transition temperature, T_g, for HNBR of 39 % ACN content as a function of cross-link fraction, computed by Molinari [25] using the same procedure described in section 4.3.3, and for NBR of 41.3 % ACN content, whose T_g value I computed in section 4.3.3. Below $F_{cl} = 80$ %, T_g of HNBR is higher than that of NBR. This is corre-

*As the density of HNBR increases with ACN content [18], the discrepancy would get marginally larger if the comparison were made at the same ACN content.

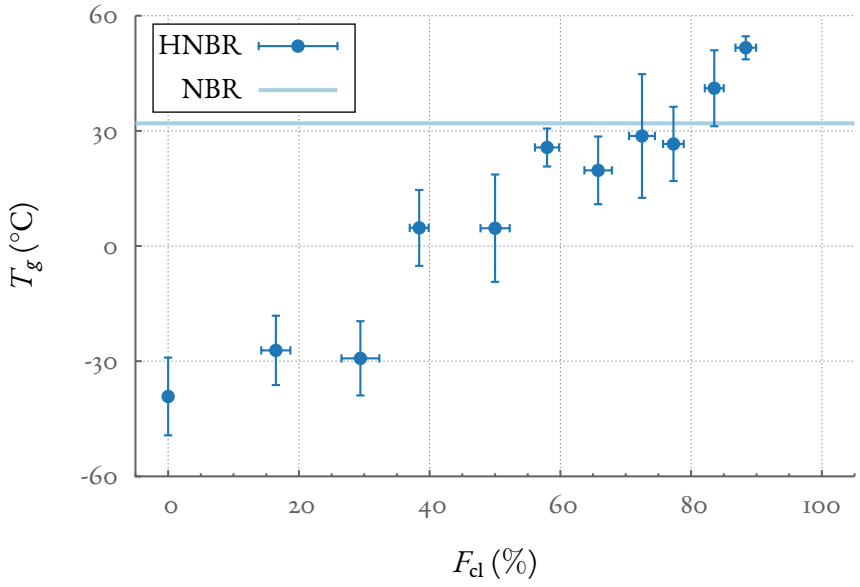


Figure 7.4: Glass transition temperature for HNBR (39 % ACN content), computed by Molinari [25], and for NBR of 41.3 % ACN content. Error bars represent standard deviation.

lated with a drop in density, which would decrease the intra-chain friction, facilitating reptation at a lower temperature. The overall trend of increasing T_g with increasing cross-link fraction is due to both the increasing density as well as the addition of covalent bonds during the cross-linking process that reduce the ability of the polymer to perform long-range co-ordinated molecular motion at a given temperature.

The quoted T_g for a commercial form of HNBR of 34 % ACN content with $F_{\mathrm{cl}} = 0\,\%$ is $-24.8\,^{\circ}\mathrm{C}$ [165], compared to the computed value of $(-39 \pm 10)\,^{\circ}\mathrm{C}$ for 41.3 % ACN content, where the uncertainty is the standard deviation. While this agreement is better than the agreement obtained for NBR in section 4.3.3, this could be coincidental, given the issues involved in calculating T_g over such short time- and length-scales in simulation, as well as the difficulties in measuring T_g in experiment, as previously discussed.*

Figure 7.5 shows the bulk modulus for HNBR as a function of cross-link fraction, and for the NBR of 41.3 % ACN content from which it was generated, calculated using the pro-

*As with NBR, T_g of HNBR increases with ACN content (although unlike NBR, does not do so linearly) [166]. Therefore the discrepancy between simulation and experiment would worsen if T_g values were compared for the same ACN content.

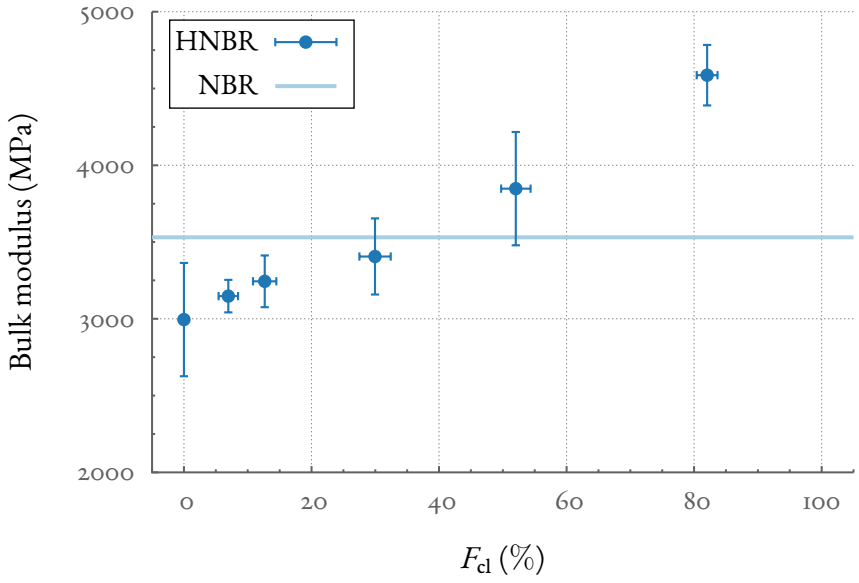


Figure 7.5: Bulk modulus of HNBR (41.3 % ACN content) and the NBR from which it was generated, at SATP. Error bars represent standard deviation.

cedure described in section 4.3.2. HNBR with low cross-link fraction ($F_{cl} < 52\,\%$) is less stiff than NBR, which can be attributed to the replacement of the C=C bonds with longer and less stiff C−C bonds. With increasing cross-link fraction, the material becomes stiffer due to the addition of covalent bonds that constrain the deformation of the network in response to an applied stress.

The model presented for HNBR mimics the real process by which HNBR is generated, by selective hydrogenation and cross-linking of NBR. It has been validated by computing bulk properties, producing physically reasonable trends and comparing directly to experiment wherever possible. It can now be used to explore the permeability in HNBR.

7.2 Transport properties

7.2.1 Solubility

To investigate the effect that cross-linking has on solubility, the biased Widom insertion technique was used to calculate solubility in HNBR using $\alpha = 0.2$, 10^6 grid points, and 100

insertions per grid point defined as free volume, as in chapter 5. Insertions were performed on $m = 250$ snapshots generated from long MD runs from each of $n = 24$ independently generated and equilibrated HNBR structures of 41.3 % ACN content, at SATP, as in chapter 4.

Figure 7.6 shows the solubility in HNBR as a function of cross-link fraction, and includes a comparison to the solubility in the NBR from which the HNBR was generated. For low cross-link fractions, the solubility in NBR and HNBR is similar, suggesting that there is no imperative to choose HNBR over NBR for a particular application based on gas absorption alone. With increasing cross-link fraction, the solubility increases for all gases studied, and does so exponentially. This is perhaps counter-intuitive, given that, as shown in Figure 7.3, the density increases with cross-link fraction. Figure 7.7 reveals that the total free volume is increasing with cross-link fraction too. As shown in Figure 7.8, solubility is correlated to free volume, especially for nonpolar gases (those for which all partial charges were set to zero). But there is still the question of why the free volume is increasing with cross-link fraction to begin with, since, presumably, as the degree of cross-linking increases, the chains become more tightly packed, the density increases, and the free volume should drop off. This trend of increasing free volume with density was also observed for NBR, but in that case was attributed to an increasing number of side chains, randomly distributed along the chain, hindering efficient packing.

One hypothesis is that the static cross-linking routine is responsible, as, by linking multiple parts of the polymer instantaneously through irreversible covalent bonds, the polymer is 'frozen' into an artificially high energy configuration, that the equilibration routine cannot help it to escape from. To investigate this, I developed a dynamic cross-linking routine, in which steps of dynamics under an NVT ensemble at standard ambient temperature (25 °C) were performed between steps of cross-linking. For a given non-zero target cross-link fraction, at each step of the routine, $\frac{100}{f_{cl}}$ % of the initial number of C=C bonds may be either hydrogenated or cross-linked. For example, for $f_{cl} = 25$ %, 25 cross-linking steps were performed, with each step ceasing after 4 % of the initial number of C=C bonds (in the unsaturated structure) were either cross-linked or hydrogenated. In total the cross-linking procedure therefore lasts $\frac{f_{cl}}{10}$ ns. The saturated structures were then equilibrated as before. This was tested at two separate cross-link fractions, and the solubility and fractional free

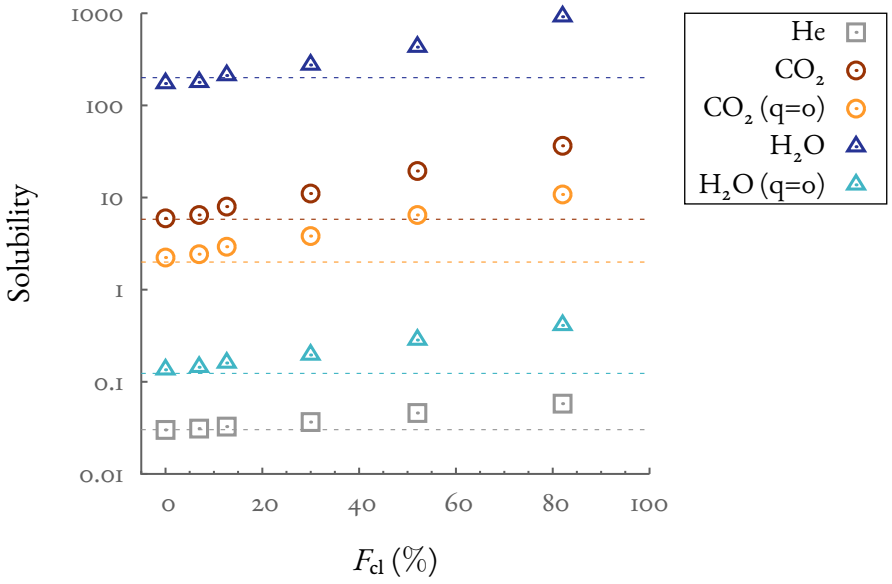


Figure 7.6: Solubility as a function of cross-link fraction in HNBR (41.3 % ACN content). Dashed lines indicate the solubility of the gases in the NBR that the HNBR has been generated from. Standard error in the solubility was less than 5 %.

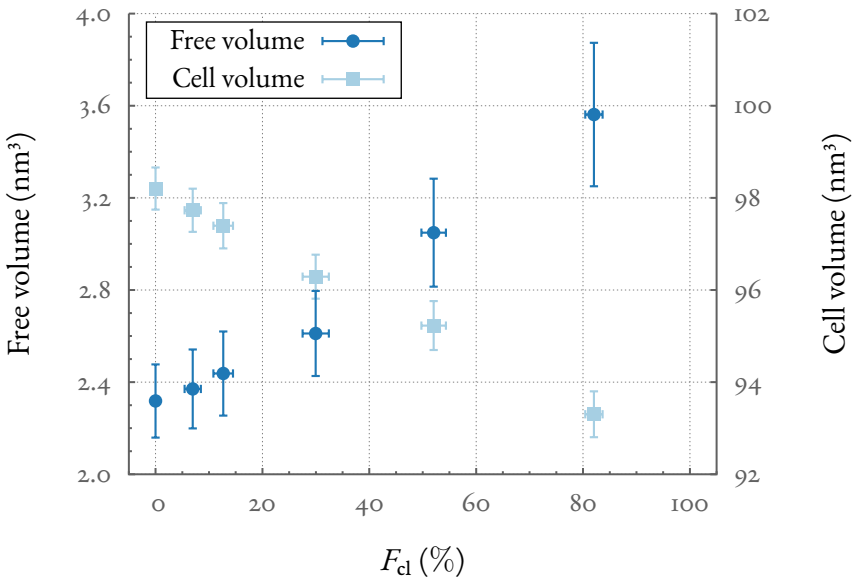


Figure 7.7: Comparison between free volume and simulation cell volume as a function of true cross-link fraction, F_{cl}.

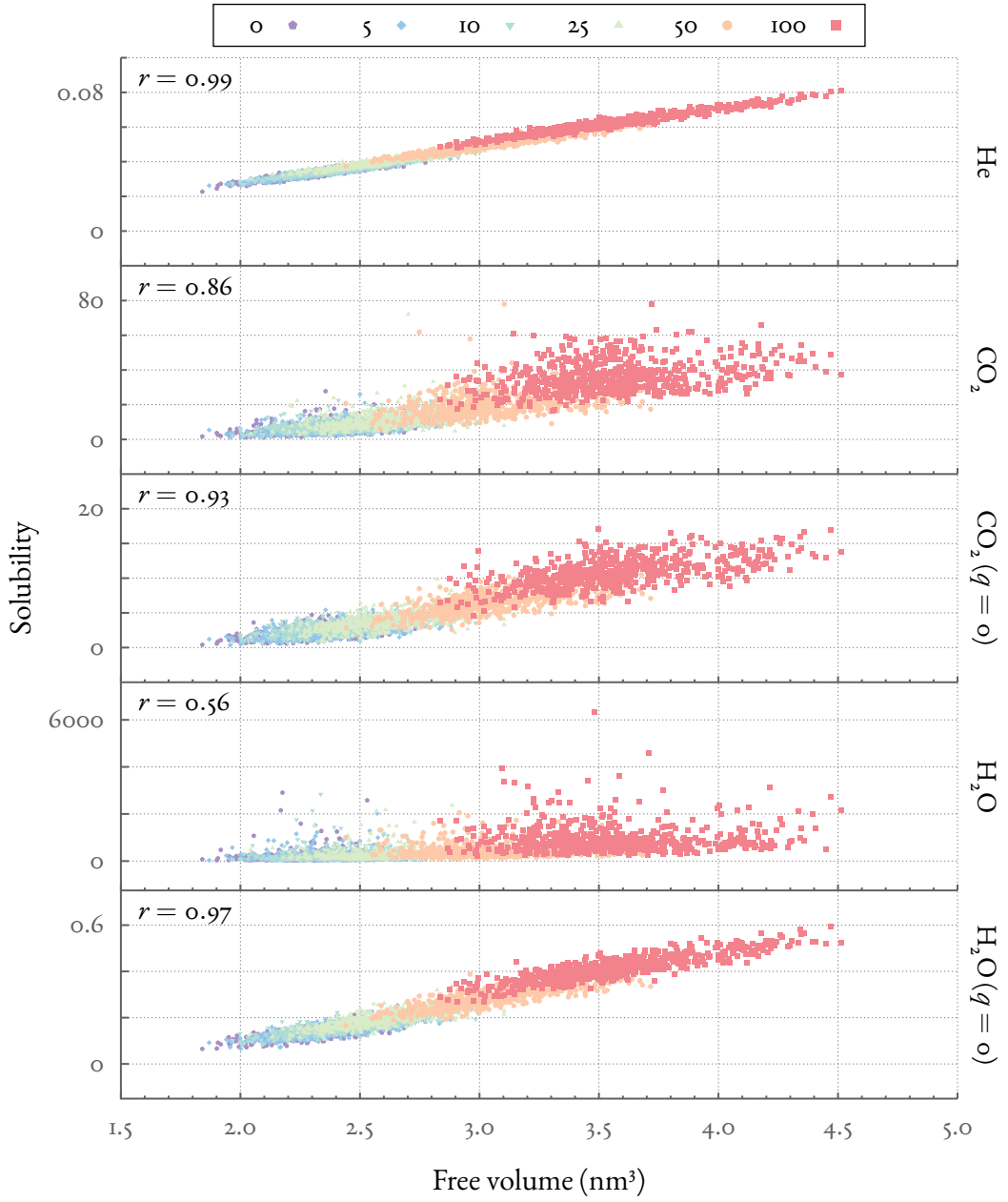


Figure 7.8: Solubility as a function of free volume and target cross-link fraction, f_{cl}, for different gases. The Pearson correlation coefficient, r, is also shown. It is a measure of the degree of linear correlation between the solubility and the free volume, i.e., $r = -1$ corresponds to perfect negative correlation and $r = 1$ corresponds to perfect positive correlation.

volume were unchanged to within 5 %.

Another issue could be the use of a single chain, as, due to the periodic boundary conditions, having a single chain wrapped around itself imposes artificial correlations upon the system. In order to investigate this, the solubility was calculated for dynamically cross-linked and equilibrated structures consisting of 5 chains of 500 monomers packed into a simulation cell.* At the two cross-link fractions tested, for all gases, the solubility did not change by more than 6 %, the free volume did not change by more than 4 %, and the trends of increasing solubility and free volume with cross-link fraction were preserved.

While both of these tests provided null results, they do not rule out the hypotheses altogether. It could be the case that dynamic cross-linking is necessary, but at a much longer timescale than tested. Similarly, it could be that multiple chains are needed to simulate cross-linking properly, but more and/or longer chains are required than were used here. But I would speculate that, if this is the case, a substantial increase in time- and length-scales would be necessary to observe the dramatic reversal of the free volume trend with cross-link fraction that appears necessary to reverse the trend in the solubility.

Another way of investigating the source of the free volume increase is to break down the per-cell free volume into connected clusters, or pores, and examine the variation of these clusters in size with cross-link fraction. This was done for statically cross-linked HNBR of 41.3 % ACN content, each simulation cell consisting of one chain of 1000 monomers, generated and equilibrated at SATP.†

The procedure is as follows. The grid of points corresponding to free volume is turned into a graph of nodes. For every node, if there exists a neighbour on the grid within one move, an edge is added between the pair of nodes. A move is defined as one step in any direction, including across periodic boundary conditions, as well as diagonally, i.e., a single node can have a maximum of $3^3-1 = 26$ neighbours. Once the entire graph has been mapped, it is divided into connected subgraphs or clusters, i.e., such that any node of the cluster is accessible from any other node in the cluster, but from no other nodes in any

*As the resulting system contained 2.5 times as many atoms as before, the number of grid points was increased by a factor of approximately 2.5, to 136^3.

†Out of the $n = 24$ independently generated configurations and $m = 250$ snapshots per configuration, only every tenth snapshot was used in this calculation due to computational expense.

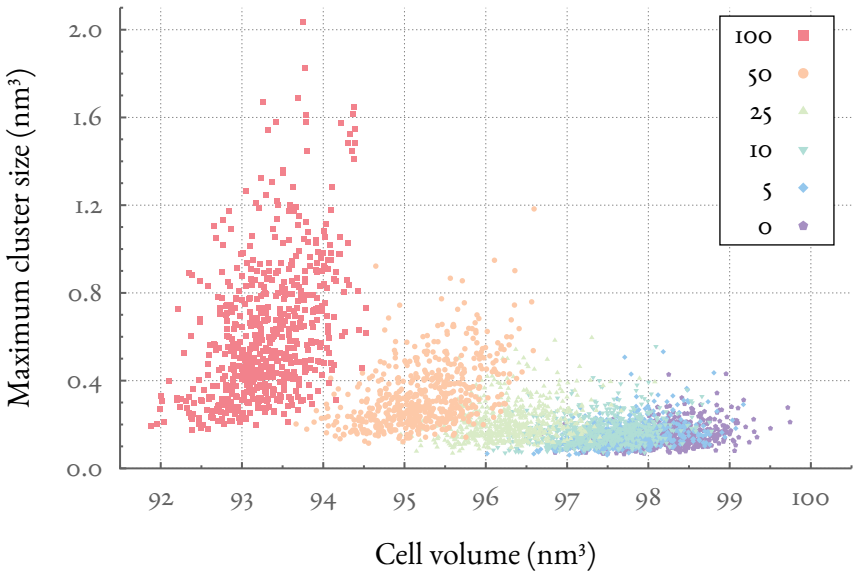


Figure 7.9: Maximum cluster size as a function of cell volume for different target cross-link fractions, f_{cl}.

other cluster. The number of nodes per cluster are computed, and turned into a volume, with each node representing one millionth of the cell volume in this case.

Figure 7.9 shows the maximum cluster size as a function of cell volume and target cross-link fraction. With increasing cross-link fraction, the maximum cluster size increases. This suggests that the increasing free volume is not being spread out uniformly, but is biased towards regions of existing free volume, causing them to coalesce into super-clusters. Indeed, in the most extreme case, there exists a cluster that is over 2 nm³ in volume, corresponding to over half of the free volume in that particular simulation cell. This trend is borne out by the data, where for $f_{\mathrm{cl}} = 0\,\%$, on average the largest cluster represents no more than 6 % of the total free volume, whereas for $f_{\mathrm{cl}} = 100\,\%$ it represents 17 %. This phenomenon could be due to the localisation of cross-linking in the polymer, such that the inhomogeneity in the polymer increases, resulting in denser regions of excluded volume that subsume the smaller clusters of free volume, allowing the larger ones to coalesce.

Ultimately, while the cluster data is necessary but not sufficient to prove this hypothesis of cross-linking localisation, it has been demonstrated that the computed solubility results for HNBR as a function of cross-linking cannot be dismissed out of hand. This is a trend

worthy of additional study, either through simulation to break down the mechanisms further, or through experiment to see if the predictions of the model are reproduced.

7.2.2 Diffusivity

Diffusivities have been calculated using the same procedure employed in section 6.1 for NBR. In short, $n = 24$ independently generated HNBR configurations were equilibrated at SATP. $N = 6$ gas molecules were inserted into low energy sites in the polymer, sufficiently far from one another (at least 2 nm). After a short equilibration (2 ns), the MSD of the gas molecules as a function of time was recorded for 16 ns. The ensemble averaged MSD as a function of time was computed over all molecules and all time origins, t_o, up to a maximum time of 8 ns. The diffusivity was determined from the gradient of a straight line fitted to the MSD data from 1–8 ns.

Figure 7.10 shows diffusivities in HNBR as a function of cross-link fraction, F_{cl}, as well as a comparison to the diffusivity of the same gases in the NBR that the HNBR was generated from. As with NBR, nonpolar gases have higher diffusivities than polar ones. This is likely to be due to the same reason, i.e., physical binding to the cyano group.

With increasing F_{cl}, the diffusivity of all gases tends to decrease.* As previously shown, while the density of HNBR increases with increasing F_{cl}, the free volume and maximum cluster size also increases, i.e., there is a localisation in free volume. This localisation could account for the decreasing diffusivity, since, if there are fewer cavities, further apart, the chances of a channel opening up between them is smaller. Furthermore, with increasing cross-link fraction the stiffness of the material increases, making it harder for channels to open up to begin with.

Figure 7.11 shows permeabilities in HNBR as a function of cross-link fraction, inferred from the computed solubilities and diffusivities.† The permeabilities of the same gases in the initial NBR structures is also shown. This time precisely the same ordering is not found in NBR and HNBR, since nonpolar CO_2 has a slightly higher permeability than helium,

*The maximum standard error was approximately 15 %, and therefore it is not possible to read too much into any data points that do not fit this trend, as the differences are not sufficiently substantial.

†As in section 6.2.5, CO_2 solubilities, both polar and nonpolar, were recomputed using the force-field of Myshakin *et al.* [158] to ensure consistency with the force-field used for diffusivity simulations.

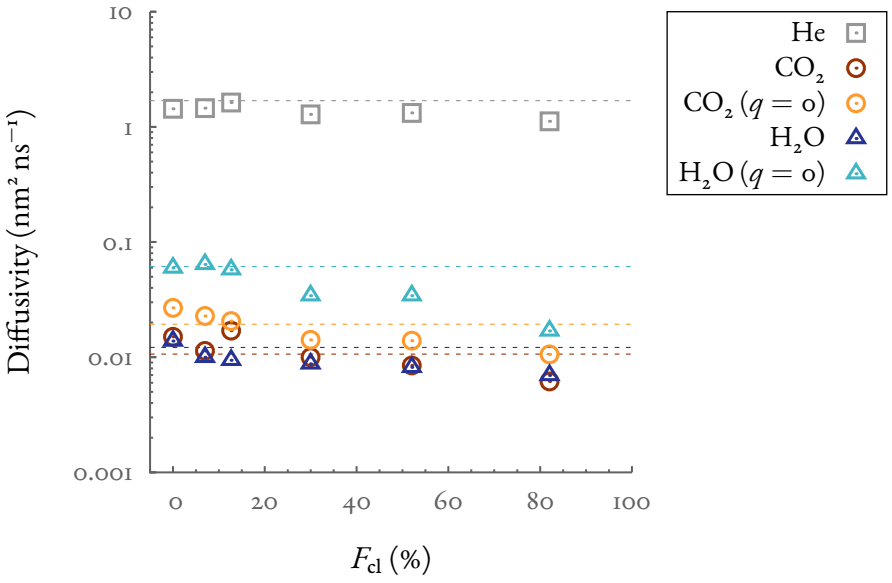


Figure 7.10: Computed diffusivity in HNBR (41.3 % ACN content) as a function of cross-link fraction, F_{cl}. Dashed lines indicate the diffusivity of the gases in the NBR that the HNBR has been generated from.

owing to its higher solubility. With the exception of nonpolar H_2O, permeability increases as F_{cl} increases. This is a solubility driven effect, and is therefore driven by the same phenomena evaluated in section 7.2.1.

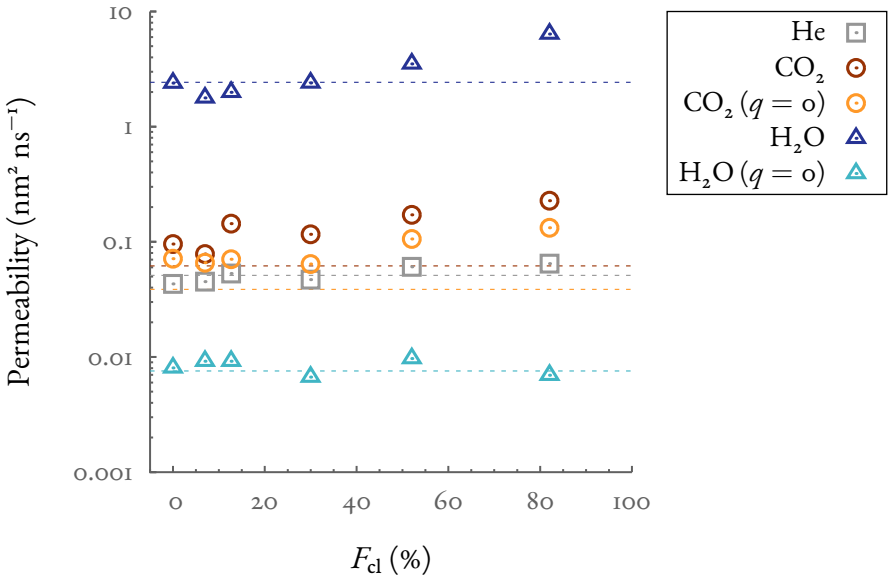


Figure 7.11: Computed permeability in HNBR (41.3 % ACN content) as a function of cross-link fraction, F_{cl}. Dashed lines indicate the permeability of the gases in the NBR that the HNBR has been generated from.

8

Conclusions

Permeation-driven elastomer seal failure in the oil and gas industry is a costly problem, with consequences ranging from corrosive damage to sensitive electronic equipment, to outright tool failure. Previous approaches to tackling this problem have either been through experiment, where it is tough to reproduce downhole conditions and monitor failure, or through finite element modelling, where the difficulty lies in accounting for the coupling of transport, thermal and mechanical phenomena in an elastic medium.

In this thesis, I have approached this problem at a fundamental level using molecular simulation, with the goal of developing an understanding of gas permeation in two widely used elastomers, NBR and HNBR. Although in principle the interatomic interactions would be better described with an *ab initio* method, in practice the length- and time-scales required to study permeation through such simulations would be computationally infeasible.* Furthermore, while coarse-grained approaches are able to expand the length- and time-scales accessible through simulation, they are accompanied by a loss in chemical specificity — something that is necessary when investigating the permeability of specific gases in

*Also, it is as yet unclear whether recent developments for non-local functionals in DFT are sufficiently transferable across different systems, without having to cherry pick the functional to obtain the correct answer [13, 14].

specific elastomers. Therefore I began by developing a fully atomistic model for NBR using the OPLS-AA force-field [26]. This model was verified by computing bulk properties such as density and glass transition temperature and comparing them to experiment, finding reasonable numerical agreement for the former and reproducing observed trends in the latter.

I was then able to investigate the permeability in NBR, defined using the solution-diffusion model as the product of solubility and diffusivity. For solubility, one of the key issues that tends to be left unspoken in the literature is that of convergence. I have demonstrated the importance of properly sampling both the polymer phase space by generating multiple independent initial configurations and the gas-polymer phase space by performing sufficient insertions. This enabled me to compute solubilities at both ambient and elevated conditions with a degree of confidence. As in experiment [71, 92], solubilities at SATP were found to increase with increasing ACN content for all gases, with the increase being more pronounced for polar molecules. To probe this relationship further, the total per-simulation-cell solubilities were decomposed into local per-atom-type solubilities, where the atom types were restricted to carbon atoms of differing orbital hybridisation, and nitrogen. This analysis revealed that polar gas molecules, in particular H_2O, preferred to be absorbed near nitrogen sites in the elastomer. Under elevated conditions, increasing temperature was found to reduce the solubility of H_2O and CO_2, while increasing that of helium. Increasing pressure suppressed the solubility of all gases, but at differing rates such that at sufficiently high pressures the solubility of CO_2 is eventually lower than that of helium, owing to steric effects superseding the stronger interaction between CO_2 and the elastomer. The range of temperatures and pressures considered exceeds those studied in any experimental work that I was able to find, and reflects those found in an oil and gas exploration context.

The diffusivity in NBR was computed in chapter 6 using an MD approach, in which the trajectories of inserted gas molecules were tracked over long simulations. This technique was preferred over TST methods as it allows full polymer relaxation and is not sensitive to any pre-defined fluctuation dampening parameters. The main disadvantage of this method is the substantially higher computational expense required to compute a given trajectory. Nevertheless I was able to compute average diffusivities to within a standard error of ap-

proximately 10 %. The two main types of diffusive behaviour — rattling inside cavities followed by occasional jumps between adjacent cavities — were demonstrated, and it was shown that the normal diffusive regime was reached within 1 ns for all gases. The diffusivity of all gases — independent of polarity — decreased as a function of increasing ACN content. For CO_2 and helium this matches the experimentally observed trend. For H_2O, no data was available for comparison.

Molinari [25] extended the model that I have developed for NBR to HNBR, using a static hydrogenation and cross-linking method that mimics peroxide curing. In chapter 7 I used this model to study the permeability in HNBR as a function of cross-link fraction. I found that while with increasing cross-link fraction the diffusivity showed a slight drop off, the solubility actually increased, despite the density also increasing. Upon further investigation, it was found that the total free volume was increasing as well, due to a localisation in the distribution of free volume, into increasingly larger clusters. This was leading to more available sites for insertion, and therefore a higher solubility. This counter-intuitive result has not been reported in the HNBR literature. In fact, I was unable to find any permeability data for HNBR as a function of cross-linking, so the work in this chapter represents an important set of predictions with which this model can be tested.

In almost all cases, computed solubilities, diffusivities and permeabilities, were overestimated with respect to the available experimental data. This is consistent with permeation simulations throughout the literature, and can be attributed to three main reasons. Firstly, there are differences between the elastomer formulations used in experiment and the systems studied in this work. For example, the NBR samples used by Van Amerongen [71, 92] were vulcanised and contained various processing additives, whereas no cross-links or additives were present in the NBR systems that I have studied. Secondly, there is a substantial discrepancy between the length- and time-scales that it is possible to study via experiment and simulation. In chapter 6 I showed that there is a noticeable inhomogeneity and anisotropy in the NBR systems that I have been using. The use of multiple independent configurations can help to mitigate this. But there is still the fundamental limit of the size of the simulation cell, which is approximately 5 nm in length, meaning features in the

polymer at a length-scale longer than this have been ignored.* Similarly, no more than approximately 10 ns of relaxation was possible following the initial structure generation, over which time the polymer is only able to explore a heavily localised region of its phase-space. Furthermore, by using a single chain, wrapped around itself across periodic boundaries, spurious correlations between atoms are introduced, i.e., the chain is able to interact with itself in unphysical ways. Ideally, to avoid this, larger systems consisting of multiple chains spanning the experimentally observed molecular weight distribution of the polymer would be used. These length- and time-scale issues were particularly noticeable when considering the glass transition temperature, which even in experiments is found to depend on cooling rates [144] as well as the precise methodology used [146], and for which the quantitative agreement with experiment was found to be poor, even across nearly 100 independent configurations each cooled at least 35 ns in total. Finally, there is the issue of the force-field. The force-field consists of two sets of terms — those that govern bonded and non-bonded interactions. The former are parameterised against *ab initio* simulations, and are generally in good agreement with experimental values. In contrast, the latter are parameterised in an aggregate sense, by simulating bulk systems and tweaking the parameters to match the experimental values of quantities such as density and heat of vaporisation. To take polyethylene as an example, while there is evidently a unique choice for, e.g., the equilibrium C—C bond length, there may be multiple ways to define the partial charges and LJ parameters of the carbon and hydrogen atoms to reproduce the correct bulk density. But although the bulk density has limited sensitivity to these non-bonded parameters, the solubility is particularly sensitive to them, as it has an exponential dependence on the precise interaction energy between the gas molecule and the polymer. Similarly, diffusion relies on nanoscale fluctuations in the polymer matrix to open up channels between nearby cavities, a process that has been shown to be sensitive to the force-field [118].

In spite of these limitations, molecular simulation is a useful tool for qualitatively predicting trends in and developing an understanding of gas permeation. For example, while an experimentalist could speculate that electrostatics is crucial in determining the enhanced

*Although it is worth noting that in spite of these limitations with system size, my simulations are the largest that have been performed on NBR. For example, Kucukpinar and Doruker [19] studied systems with six times fewer atoms, and used three independent configurations.

solubility of CO_2 with respect to other gases in NBR, only in simulation could I show this explicitly by setting the partial charges of the carbon and oxygen atoms to zero, showing that the total solubility falls and that the distribution of absorption sites changes. For investigating the issue of permeative elastomer seal failure further, it is clear that simulation has an important part to play.

8.1 Further work

Having understood some of the key drivers of and trends in the permeation of small gases in NBR and HNBR, the next step is to investigate methods of reducing gas permeation with the aim of inhibiting permeative seal failure. Polymer modification is one such method. The cyano group has been shown to be a major factor in the permeation of polar gases, which have higher permeabilities than nonpolar ones. Chemically reducing the number density of cyano groups in the polymer, e.g., by replacing them with CH_3 groups, would likely reduce gas solubility. However, at the same time it would increase diffusivity. The trade off between the two factors could be evaluated as a function of the number density of cyano groups replaced, to determine the net effect on the permeability.

It is worth stressing that a reduction in permeability need not be the end goal of such work, or indeed any experimental investigations, if the aim is to reduce the incidence of explosive decompression. A gas with a high diffusivity but low solubility will be less likely to cause rupture than a gas for which the reverse is true, since there is less gas within the seal to begin with, and what gas is present is quick to egress when the external pressure is relieved. In the ideal case, for a fixed permeability the solubility should be minimised and the diffusivity maximised. In fact, it is possible for an increase in permeability to actually lead to a reduction in seal failure.

Modification of the entire elastomer is problematic, however, as it can lead to undesirable changes in other material properties such as stiffness, tear strength and glass transition temperature, as well as resistance to hydrocarbons and to thermal degradation, all of which have to be optimised when designing an elastomer formulation. An alternative is surface modification. For example, by massively suppressing the solubility by removing all cyano groups in the surface region, say, 1 nm to 1 μm into the seal, the quantity of gas in the elas-

tomer is reduced, due to the modified region effectively acting as a barrier to permeation, and the engineering challenges posed by modification of the seal as a whole are avoided. Any increases in diffusivity over this region become negligible as its width is insubstantial compared to the width of the seal. Molecular simulation is critical in these investigations as it offers a way to quickly screen such potential modifications for efficacy.

Filler particles are another potential candidate for elastomer modification, and could form an important extension to this work. While the interior of the filler agglomerate is inaccessible to small gas molecules, the surface might act to either increase or decrease the permeability, depending on its functionalisation and the type of gas. Although fillers were neglected in this work due to length- and time-scale constraints, it is possible to design atomistic simulations to study the *surface* of filler particles and their precise interactions with different gas molecules. Filler particles could be designed with surfaces that act as a trap for gas molecules, and they could be dispersed preferentially near the surface of the elastomer. Moreover, the surface area to volume ratio of the filler could be optimised by designing a particle with a fractal-like shape.

Another method of overcoming length- and time-scale constraints would be to use coarse-grained simulations. With even the simplest of coarse-graining techniques, the united-atom model, the fastest degrees of freedom in the system, i.e., the C—H bonds, are removed, enabling a faster timestep to be used. Furthermore, as atoms are removed, not only can more atoms be used for the same computational cost, the friction between chains is reduced [47], and therefore the relaxation via reptation occurs more quickly. This means that for the same computational cost, a coarse-grained system can be larger and explore the phase space further than the equivalent fully atomistic system. The disadvantage of this approach is that there is a loss in chemical specificity, which is particularly important when computing permeabilities. One solution is to use reverse-mapping [167], where, after mapping a fully atomistic system to a coarse-grained system for the purposes of equilibration, it can then be mapped *back* to the fully atomistic system in order to study properties that rely on an atomistic level of detail. This would enable larger systems to be studied, over longer time periods.

Finally, some of the predictions made in this thesis need to be experimentally verified. Of particular interest are the results obtained for H_2O, which was found to have a higher per-

meability in NBR than both CO_2 and helium, is a major component in corrosion, and for which no experimental data was found. No permeability data was available for HNBR for any cross-link fraction either, therefore the unexpected result of increasing solubility with cross-link fraction needs to be tested, to determine whether it is just an artefact of the simulation procedure, or truly valid. If it is indeed valid, then reducing the degree of saturation of the polymer towards the surface of an HNBR seal is another tool that could be used to reduce permeation, and ultimately inhibit elastomer seal failure.

Bibliography

[1] R. C. Klingender. *Handbook of Specialty Elastomers*. CRC Press, 2008.

[2] W. J. Roff and J. R. Scott. *Fibres, Films, Plastics and Rubbers: A Handbook of Common Polymers*. Elsevier, 2013.

[3] A. Ciesielski. *An Introduction to Rubber Technology*. iSmithers Rapra Publishing, 1999.

[4] L. W. Lake and R. F. Mitchell. *Petroleum Engineering Handbook: Drilling Engineering*. Vol. 2. Society of Petroleum Engineers, 2006.

[5] C. Avant et al. *Testing the Limits in Extreme Well Conditions*. Technical Report. Quartzdyne – Dover Corporation, 2012.

[6] B. Hughes. *2013 Annual Report*. http://phx.corporate-ir.net/phoenix.zhtml?c=79687&p=irol-reportsannual. Accessed 09-2016.

[7] B. Briscoe, T. Savvas, and C. Kelly. "'Explosive Decompression Failure' of Rubbers: a Review of the Origins of Pneumatic Stress Induced Rupture in Elastomers". *Rubber Chemistry and Technology* 67.3 (1994), pp. 384–416.

[8] A. Gent and D. Tompkins. "Nucleation and Growth of Gas Bubbles in Elastomers". *Journal of Applied Physics* 40.6 (1969), pp. 2520–2525.

[9] A. Stevenson and G. Morgan. "Fracture of Elastomers by Gas Decompression". *Rubber Chemistry and Technology* 68.2 (1995), pp. 197–211.

[10] *Baker Hughes Inc.* `http://www.bakerhughes.com`.

[11] J. Wijmans and R. Baker. "The Solution-Diffusion Model: A Review". *Journal of Membrane Science* 107.1 (1995), pp. 1–21.

[12] W. Henry. "Experiments on the Quantity of Gases Absorbed by Water, at Different Temperatures, and Under Different Pressures". *Philosophical Transactions of the Royal Society of London* 93 (1803), pp. 29–276.

[13] J. F. Dobson and T. Gould. "Calculation of Dispersion Energies". *Journal of Physics: Condensed Matter* 24.7 (2012), p. 073201.

[14] J. Klimeš and A. Michaelides. "Perspective: Advances and Challenges in Treating Van Der Waals Dispersion Forces in Density Functional Theory". *The Journal of Chemical Physics* 137.12 (2012), p. 120901.

[15] M. Karplus and J. A. McCammon. "Molecular Dynamics Simulations of Biomolecules". *Nature Structural & Molecular Biology* 9.9 (2002), pp. 646–652.

[16] B. Alder, D. Gass, and T. Wainwright. "Studies in Molecular Dynamics. VIII. The Transport Coefficients for a Hard-Sphere Fluid". *The Journal of Chemical Physics* 53.10 (1970), pp. 3813–3826.

[17] D. Mackey and A. H. Jorgensen. "Nitrile Rubber". In: *Kirk-Othmer Encyclopedia of Chemical Technology*. John Wiley & Sons, Inc., 2000.

[18] *Therban - HNBR Brochure*. http://therban.com/uploads/tx_lxsmatrix/Therban_Broschure.pdf. Accessed: 12-2016.

[19] E. Kucukpinar and P. Doruker. "Molecular Simulations of Gas Transport in Nitrile Rubber and Styrene Butadiene Rubber". *Polymer* 47.22 (2006), pp. 7835–7845.

[20] M. Song et al. "Molecular Dynamics Simulations and Microscopic Analysis of the Damping Performance of Hindered Phenol AO-60/Nitrile-Butadiene Rubber Composites". *RSC Advances* 4.13 (2014), pp. 6719–6729.

[21] M. Song et al. "Effect of Acrylonitrile Content on Compatibility and Damping Properties of Hindered Phenol AO-60/Nitrile-Butadiene Rubber Composites: Molecular Dynamics Simulation". *RSC Advances* 4 (89 2014), pp. 48472–48479.

[22] B. Qiao, X. Zhao, D. Yue, L. Zhang, and S. Wu. "A Combined Experiment and Molecular Dynamics Simulation Study of Hydrogen Bonds and Free Volume in Nitrile-Butadiene Rubber/Hindered Phenol Damping Mixtures". *Journal of Materials Chemistry* 22 (2012), pp. 12339–12348.

[23] H. Sun, P. Ren, and J. Fried. "The COMPASS Force Field: Parameterization and Validation for Phosphazenes". *Computational and Theoretical Polymer Science* 8.1 (1998), pp. 229–246.

[24] *BIOVIA Materials Studio*. http://accelrys.com/products/collaborative-science/biovia-materials-studio/. Accessed: 12-2016.

[25] N. Molinari, M. Khawaja, A. P. Sutton, and A. A. Mostofi. "Molecular Model for HNBR With Tunable Cross-Link Density". *The Journal of Physical Chemistry B* 120.49 (2016), pp. 12700–12707.

[26] W. L. Jorgensen, D. S. Maxwell, and J. Tirado-Rives. "Development and Testing of the OPLS All-Atom Force Field on Conformational Energetics and Properties of Organic Liquids". *Journal of the American Chemical Society* 118.45 (1996), pp. 11225–11236.

[27] M. Khawaja, A. P. Sutton, and A. A. Mostofi. "Molecular Simulation of Gas Solubility in Nitrile Butadiene Rubber". *The Journal of Physical Chemistry B* (2016).

[28] B. Kopey. "Development of Drilling Technics from Ancient Ages to Modern Times". In: *12th IFToMM World Congress. Francia*. 2007.

[29] E. K. Napitupulu. *10 inch PDC oil drill bit CAD model*. https://grabcad.com/library/10-inch-pdc-oil-drill-bit-1. Accessed 09-2016. 2014.

[30] D. Browne. *PDC drill bit design CAD model*. https://grabcad.com/library/10-inch-pdc-oil-drill-bit-1. Accessed 09-2016. 2014.

[31] H. Rabia. *Oilwell Drilling Engineering: Principles and Practice*. Graham & Trotman, 1985.

[32] F. Gray. *Petroleum Production for the Non-Technical Person*. PennWell Publishing, 1995.

[33] R. F. Mitchell, S. Miska, et al. *Fundamentals of Drilling Engineering*. Society of Petroleum Engineers, 2011.

[34] R. A. Materials. *Bentonite Powder*. http://web.archive.org/web/20151010011852/http://www.reade.com/Products/Minerals_and_Ores/bentonite.html. Accessed: 12-2016.

[35] V. Mahto and V. Sharma. "Rheological Study of a Water Based Oil Well Drilling Fluid". *Journal of Petroleum Science and Engineering* 45.1 (2004), pp. 123–128.

[36] M. Dolz, J. Jiménez, M. J. Hernández, J. Delegido, and A. Casanovas. "Flow and Thixotropy of Non-Contaminating Oil Drilling Fluids Formulated with Bentonite and Sodium Carboxymethyl Cellulose". *Journal of Petroleum Science and Engineering* 57.3 (2007), pp. 294–302.

[37] J. P. Nguyen. *Oil and Gas Field Development Techniques: Drilling*. Institut Français du Pétrole Publications, 1996.

[38] D. Jamieson and J. Tudhope. "Physical Properties of Sea Water Solutions: Thermal Conductivity". *Desalination* 8.3 (1970), pp. 393 –401.

[39] C. Holmes and S. Swift. "Calculation of Circulating Mud Temperatures". *Journal of Petroleum Technology* 22.6 (1970), pp. 670–674.

[40] *Deepwater Horizon Drills World's Deepest Oil & Gas Well [Press Release]*. https://web.archive.org/web/20100426171257/http://www.deepwater.com/fw/main/IDeepwater-Horizon-i-Drills-Worlds-Deepest-Oil-and-Gas-Well-419C151.html. Transocean. Accessed: 12-2016.

[41] Baker Hughes. Personal communication.

[42] *High Pressure, High Temperature - Science of Extremes*. http://www.slb.com/services/technical_challenges/high_pressure_high_temperature.aspx. Schlumberger. Accessed 09-2016.

[43] M. J. Jellison et al. "Telemetry Drill Pipe: Enabling Technology for the Downhole Internet". In: *SPE/IADC drilling conference*. Society of Petroleum Engineers. 2003.

[44] C. E. Grethlein, B. D. Craig, and R. A. Lane. *Elastomeric Seals 101 - A Brief Tutorial*. Technical Report. Alion Science and Technology, 2004.

[45] L. H. Sperling. *Introduction to Physical Polymer Science*. Wiley-Interscience, 2005.

[46] *Standard Terminology Relating to Rubber*. Accessed 09-2016. 2011. URL: http://enterprise.astm.org/filtrexx40.cgi?+REDLINE_PAGES/D1566.htm.

[47] M. Doi. *Introduction to Polymer Physics*. Oxford University Press, 1996.

[48] O. Kallenberg. *Foundations of Modern Probability*. Springer, 2002.

[49] D. Chandler. *Introduction to Modern Statistical Mechanics*. 1st ed. Oxford University Press, 1987.

[50] K. Kremer and G. S. Grest. "Dynamics of Entangled Linear Polymer Melts: A Molecular-Dynamics Simulation". *The Journal of Chemical Physics* 92.8 (1990), pp. 5057–5086.

[51] J. H. Gibbs and E. A. DiMarzio. "Nature of the Glass Transition and the Glassy State". *The Journal of Chemical Physics* 28 (1958), p. 373.

[52] J. Van Parijs, W. F. Broekaert, I. J. Goldstein, and W. J. Peumans. "Hevein: An Antifungal Protein from Rubber-Tree (Hevea Brasiliensis) Latex". *Planta* 183.2 (1991), pp. 258–264.

[53] M. Jacob, S. Thomas, and K. Varughese. "Mechanical Properties of Sisal/Oil Palm Hybrid Fiber Reinforced Natural Rubber Composites". *Composites Science and Technology* 64.7 (2004), pp. 955–965.

[54] *Goodyear*. http://www.goodyear.com/.

[55] H. Mooibroek and K. Cornish. "Alternative Sources of Natural Rubber". *Applied Microbiology and Biotechnology* 53.4 (2000), pp. 355–365.

[56] *Schematic Structure Example of the Vulcanization of Polyisoprene*. Wikimedia Commons. http://en.wikipedia.org/wiki/File:Vulcanization_of_POLYIsoprene_V.2.png. Accessed: 12-2016.

[57] *Schematic Crystalline Block Copolymer*. Wikimedia Commons. http://en.wikipedia.org/wiki/File:SBSstructure.svg. Accessed: 12-2016.

[58] A. N. Gent. *Engineering with Rubber: How to Design Rubber Components*. Hanser Verlag, 2001.

[59] *Styrene-Butadiene O-rings*. Columbia Engineered Rubber, Inc. Accessed: 12-2016.

[60] J. Pimblott, G. Scott, and J. Stuckey. "Bis (Diisopropyl) Thiophosphoryl Disulfide in Cis-1, 4-Polyisoprene Vulcanization Reactions. I. As a Sulfur Donor". *Journal of Applied Polymer Science* 19.3 (1975), pp. 865–877.

[61] M. Geyser and W. McGill. "A Study of the Rate of Formation of Polysulfides of Tetramethylthiuram Disulfide". *Journal of Applied Polymer Science* 55.2 (1995), pp. 215–224.

[62] A. Bhowmick and S. De. "Dithiodimorpholine-Based Accelerator System in Tire Tread Compound for High-Temperature Vulcanization". *Rubber Chemistry and Technology* 52.5 (1979), pp. 985–995.

[63] A. Robinson, J. Marra, and L. Amberg. "Ethylene-Propylene Rubber Vulcanization with Aralkyl Peroxide and Coagents". *Industrial & Engineering Chemistry Product Research and Development* 1.2 (1962), pp. 78–82.

[64] P. R. Dluzneski. "Peroxide Vulcanization of Elastomers". *Rubber Chemistry and Technology* 74.3 (2001), pp. 451–492.

[65] S. M. Mamedov, A. Garibov, S. Rzaeva, F. Yadreev, and O. Sigov. "The Radiation Vulcanisation of Hydrogenated Nitrile Butadiene Rubber". *International Polymer Science and Technology* 42.6 (2015), T7.

[66] J. O'Donnell, N. Rahman, C. Smith, and D. Winzor. "Chain Scission and Cross-Linking in the Radiation Degradation of Polymers: Limitations on the Utilization of Theoretical Expressions and Experimental Results in the Pregel Region". *Macromolecules* 12.1 (1979), pp. 113–119.

[67] J. G. Drobny. *Radiation Technology for Polymers*. CRC press, 2010.

[68] J. G. Drobny. *Technology of Fluoropolymers*. CRC Press, 2008.

[69] G. Heideman, R. Datta, J. Noordermeer, and B. v. Baarle. "Influence of Zinc Oxide During Different Stages of Sulfur Vulcanization. Elucidated by Model Compound Studies". *Journal of Applied Polymer Science* 95.6 (2005), pp. 1388–1404.

[70] R. Mastromatteo, J. Mitchell, and T. Brett Jr. "New Accelerators for Blends of EPDM". *Rubber Chemistry and Technology* 44.4 (1971), pp. 1065–1079.

[71] G. J. Van Amerongen. "Influence of Structure of Elastomers on Their Permeability to Gases". *Journal of Polymer Science* V.3 (1950), pp. 307–332.

[72] B. Boonstra. "Role of Particulate Fillers in Elastomer Reinforcement: A Review". *Polymer* 20.6 (1979), pp. 691–704.

[73] V. Jha, A. Thomas, M. Bennett, and J. Busfield. "Reversible Electrical Behavior with Strain for a Carbon Black-Filled Rubber". *Journal of Applied Polymer Science* 116.1 (2010), pp. 541–546.

[74] V. Jha. "Carbon Black Filler Reinforcement of Elastomers". PhD Thesis. Queen Mary, University of London, 2008.

[75] R. P. Feynman. "Appendix F: Personal Observations on the Reliability of the Shuttle". *Report of the Presidential Commission on the Space Shuttle Challenger Accident* (1986).

[76] R. Eshel. "Prediction of Extrusion Failures of O-ring Seals". *ASLE Transactions* 27.4 (1984), pp. 332–340.

[77] B. Briscoe and S. Zakaria. "Sorption and Dilation of Silicone Elastomer Composites at High Gas Pressures: The Role of Interfacial Quality". *Journal of Polymer Science Part B: Polymer Physics* 30.9 (1992), pp. 959–969.

[78] *VAM Drilling Catalogue*. http://web.archive.org/web/20120913064725/http://www.vamdrilling.com/userfiles/file/catalog.pdf. Accessed: 12-2016.

[79] E. Ho. *Elastomeric Seals for Rapid Gas Decompression Applications in High-Pressure Services*. Technical Report. BHR Group Limited, 2006.

[80] D. Liatsis. "Gas Induced Rupture of Elastomers". PhD Thesis. Imperial College London (University of London), 1989.

[81] J. M. Routh. "Prediction of Explosive Decompression Damage in Elastomer Seals". PhD thesis. Cranfield University, 1999.

[82] G. Rambert, J. Grandidier, L. Cangemi, and Y. Meimon. "A Modelling of the Coupled Thermodiffuso-Elastic Linear Behaviour. Application to Explosive Decompression of Polymers". *Oil & Gas Science and Technology* 58.5 (2003), pp. 571–591.

[83] *DuPont Kalrez Perfluoroelastomer Parts*. https://goo.gl/os7Bdz. Accessed: 12-2016.

[84] *Rigzone - Offshore Rig Day Rates*. http://www.rigzone.com/data/dayrates/. Accessed: 12-2016.

[85] G. M. Geise et al. "Water Purification by Membranes: The Role of Polymer Science". *Journal of Polymer Science Part B: Polymer Physics* 48.15 (2010), pp. 1685–1718.

[86] T. Okano, Y. H. Bae, H. Jacobs, and S. W. Kim. "Thermally On-Off Switching Polymers for Drug Permeation and Release". *Journal of Controlled Release* 11.1 (1990), pp. 255–265.

[87] V. Stannett. "The Transport of Gases in Synthetic Polymeric Membranes—an Historic Perspective". *Journal of Membrane Science* 3.2 (1978), pp. 97–115.

[88] A. Einstein. "The Theory of the Brownian Movement". *Annalen der Physik* 17 (1905), p. 549.

[89] A. Fick. "V. On Liquid Diffusion". *The London, Edinburgh, and Dublin Philosophical Magazine and Journal of Science* 10.63 (1855), pp. 30–39.

[90] T. Graham. "On the Absorption and Dialytic Separation of Gases by Colloid Septa". *The London, Edinburgh, and Dublin Philosophical Magazine and Journal of Science* 32.218 (1866), pp. 401–420.

[91] H. A. Daynes. "The Process of Diffusion Through a Rubber Membrane". In: *Proceedings of the Royal Society of London A: Mathematical, Physical and Engineering Sciences*. Vol. 97. 685. The Royal Society. 1920, pp. 286–307.

[92] G. J. Van Amerongen. "The Permeability of Different Rubbers to Gases and Its Relation to Diffusivity and Solubility". *Journal of Applied Physics* 17.11 (1946), pp. 972–985.

[93] R. Barrer and E. K. Rideal. "Permeation, Diffusion and Solution of Gases in Organic Polymers". *Transactions of the Faraday Society* 35 (1939), pp. 628–643.

[94] S.-J. Marrink and H. J. C. Berendsen. "Simulation of Water Transport Through a Lipid Membrane". *The Journal of Physical Chemistry* 98.15 (1994), pp. 4155–4168.

[95] B. Widom. "Some Topics in the Theory of Fluids". *The Journal of Chemical Physics* 39.11 (1963), p. 2808.

[96] D. Frenkel and B. Smit. *Understanding Molecular Simulations: From Algorithms to Applications*. Academic, San Diego, 1996.

[97] K. Binder. *Monte Carlo and Molecular Dynamics Simulations in Polymer Science*. Oxford University Press, 1995.

[98] G. Deitrick, L. Scriven, and H. Davis. "Efficient Molecular Simulation of Chemical Potentials". *The Journal of Chemical Physics* 90.4 (1989), pp. 2370–2385.

[99] P. Jedlovszky and M. Mezei. "Calculation of the Free Energy Profile of H2O, O2, CO, CO2, NO, and CHCl3 in a Lipid Bilayer with a Cavity Insertion Variant of the Widom Method". *Journal of the American Chemical Society* 122.21 (2000), pp. 5125–5131.

[100] F. Müller-Plathe. "Permeation of Polymers — A Computational Approach". *Acta Polymerica* 45.4 (1994), pp. 259–293.

[101] R. Elber and M. Karplus. "Enhanced Sampling in Molecular Dynamics: Use of the Time-Dependent Hartree Approximation for a Simulation of Carbon Monoxide Diffusion Through Myoglobin". *Journal of the American Chemical Society* 112.25 (1990), pp. 9161–9175.

[102] F. Müller-Plathe, S. C. Rogers, and W. F. van Gunsteren. "Computational Evidence for Anomalous Diffusion of Small Molecules in Amorphous Polymers". *Chemical Physics Letters* 199.3-4 (1992), pp. 237–243.

[103] R. M. Sok, H. J. C. Berendsen, and W. F. van Gunsteren. "Molecular Dynamics Simulation of the Transport of Small Molecules Across a Polymer Membrane". *The Journal of Chemical Physics* 96.6 (1992), p. 4699.

[104] J. Brandrup, E. H. Immergut, E. A. Grulke, A. Abe, and D. R. Bloch. *Polymer Handbook*. Vol. 7. Wiley New York, 1989.

[105] S. M. Auerbach. "Theory and Simulation of Jump Dynamics, Diffusion and Phase Equilibrium in Nanopores". *International Reviews in Physical Chemistry* 19.2 (2000), pp. 155–198.

[106] M. Kotelyanskii and D. N. Theodorou. *Simulation Methods for Polymers*. CRC Press, 2004.

[107] A. A. Gusev, S. Arizzi, U. W. Suter, and D. J. Moll. "Dynamics of Light Gases in Rigid Matrices of Dense Polymers". *The Journal of Chemical Physics* 99 (1993), p. 2221.

[108] A. A. Gusev and U. W. Suter. "Dynamics of Small Molecules in Dense Polymers Subject to Thermal Motion". *The Journal of Chemical Physics* 99.3 (1993), p. 2228.

[109] D. R. Wheeler and J. Newman. "Molecular Dynamics Simulations of Multicomponent Diffusion. 1. Equilibrium Method". *The Journal of Physical Chemistry B* 108.47 (2004), pp. 18353–18361.

[110] E. Tocci, D. Hofmann, D. Paul, N. Russo, and E. Drioli. "A Molecular Simulation Study on Gas Diffusion in a Dense Poly(Ether–Ether–Ketone) Membrane". *Polymer* 42.2 (2001), pp. 521–533.

[111] S. Charati and S. Stern. "Diffusion of Gases in Silicone Polymers: Molecular Dynamics Simulations". *Macromolecules* 9297.98 (1998), pp. 5529–5535.

[112] S. Rutherford, D. Limmer, M. Smith, and K. Honnell. "Gas Transport in Ethylene–Propylene–Diene (EPDM) Elastomer: Molecular Simulation and Experimental Study". *Polymer* 48.22 (2007), pp. 6719–6727.

[113] S. Y. Lim, T. T. Tsotsis, and M. Sahimi. "Molecular Simulation of Diffusion and Sorption of Gases in an Amorphous Polymer". *The Journal of Chemical Physics* 119.1 (2003), p. 496.

[114] T. Yamada, J. L. Graham, and D. K. Minus. "Density Functional Theory Investigation of the Interaction between Nitrile Rubber and Fuel Species". *Energy & Fuels* 23.1 (2008), pp. 443–450.

[115] D. R. Alfonso and A. V. Cugini. "Ab Initio Study of Interaction of a Model Nitrile Polymer with Various Model Fuel Molecules". *Preprints of Papers - American Chemical Society, Division of Fuel Chemistry* 48.2 (2003), p. 508.

[116] S. J. Weiner et al. "A New Force Field for Molecular Mechanical Simulation of Nucleic Acids and Proteins". *Journal of the American Chemical Society* 106.3 (1984), pp. 765–784.

[117] H. R. Warner Jr. "Kinetic Theory and Rheology of Dilute Suspensions of Finitely Extendible Dumbbells". *Industrial & Engineering Chemistry Fundamentals* 11.3 (1972), pp. 379–387.

[118] F. Mueller-Plathe, S. C. Rogers, and W. F. Van Gunsteren. "Diffusion Coefficients of Penetrant Gases in Polyisobutylene Can Be Calculated Correctly by Molecular-Dynamics Simulations". *Macromolecules* 25.24 (1992), pp. 6722–6724.

[119] F. R. Mayo and F. M. Lewis. "Copolymerization. I. A Basis for Comparing the Behavior of Monomers in Copolymerization; The Copolymerization of Styrene and Methyl Methacrylate". *Journal of the American Chemical Society* 66.9 (1944), pp. 1594–1601.

[120] A. K. Bhowmick and H. Stephens. *Handbook of Elastomers*. CRC Press, 2000.

[121] B. Willoughby. "A Structural Analysis of Nitrile Rubbers—the 13 C Resonance Technique". *Polymer Testing* 8.1 (1989), pp. 45–70.

[122] M. P. Allen and D. J. Tildesley. *Computer Simulation of Liquids*. Oxford University Press, 1989.

[123] M. Doi and S. F. Edwards. *The Theory of Polymer Dynamics*. Vol. 73. Oxford University Press, 1988.

[124] D. N. Theodorou and U. W. Suter. "Detailed Molecular Structure of a Vinyl Polymer Glass". *Macromolecules* 18.7 (1985), pp. 1467–1478.

[125] E. Kucukpinar and P. Doruker. "Molecular Simulations of Small Gas Diffusion and Solubility in Copolymers of Styrene". *Polymer* 44.12 (2003), pp. 3607–3620.

[126] S. Plimpton. “Fast Parallel Algorithms for Short-Range Molecular Dynamics”. *Journal of Computational Physics* 117.1 (1995), pp. 1–19.

[127] E. Bitzek, P. Koskinen, F. Gähler, M. Moseler, and P. Gumbsch. “Structural Relaxation Made Simple”. *Physical Review Letters* 97.17 (2006), p. 170201.

[128] D. Doherty, B. Holmes, P. Leung, and R. Ross. “Polymerization Molecular Dynamics Simulations. I. Cross-linked Atomistic Models for Poly(methacrylate) Networks”. *Computational and Theoretical Polymer Science* 8.1 (1998), pp. 169–178.

[129] B. Arab, A. Shokuhfar, and S. Ebrahimi-Nejad. “Glass Transition Temperature of Cross-Linked Epoxy Polymers: a Molecular Dynamics Study”. In: *Nanomaterials: Application & Properties*. 2012.

[130] J. Liu, S. Wu, L. Zhang, W. Wang, and D. Cao. “Molecular Dynamics Simulation for Insight into Microscopic Mechanism of Polymer Reinforcement”. *Physical Chemistry Chemical Physics* 13.2 (2011), pp. 518–529.

[131] W. Eckhardt et al. “591 TFLOPS Multi-Trillion Particles Simulation on SuperMUC”. In: *International Supercomputing Conference*. Springer. 2013, pp. 1–12.

[132] J.-P. Ryckaert, G. Ciccotti, and H. J. Berendsen. “Numerical Integration of the Cartesian Equations of Motion of a System with Constraints: Molecular Dynamics of n-alkanes”. *Journal of Computational Physics* 23.3 (1977), pp. 327–341.

[133] M. Tuckerman, B. J. Berne, and G. J. Martyna. “Reversible Multiple Time Scale Molecular Dynamics”. *The Journal of Chemical Physics* 97.3 (1992), pp. 1990–2001.

[134] S. Plimpton, R. Pollock, and M. Stevens. “Particle-Mesh Ewald and rRESPA for Parallel Molecular Dynamics Simulations”. In: *PPSC*. Citeseer. 1997.

[135] D. C. Rapaport. *The Art of Molecular Dynamics Simulation*. Cambridge University Press, 2004.

[136] H. Sun, S. J. Mumby, J. R. Maple, and A. T. Hagler. “An Ab Initio CFF93 All-Atom Force Field for Polycarbonates”. *Journal of the American Chemical Society* 116.7 (1994), pp. 2978–2987.

[137] *Materials Design MedeA*. http://www.materialsdesign.com/medea. Accessed: 12-2016.

[138] K. Seppelt. "Sulfur/Carbon Double and Triple Bonds". *Pure and Applied Chemistry* 59.8 (1987), pp. 1057–1062.

[139] *Military Standardization Handbook - Rubber*. MIL-HDBK-149B FSC 930. US Department of Defence, 1984.

[140] F. Murnaghan. "The Compressibility of Media Under Extreme Pressures". *Proceedings of the National Academy of Sciences* 30.9 (1944), pp. 244–247.

[141] F. Birch. "Finite Elastic Strain of Cubic Crystals". *Physical Review* 71.11 (1947), p. 809.

[142] J. Han, R. H. Gee, and R. H. Boyd. "Glass Transition Temperatures of Polymers from Molecular Dynamics Simulations". *Macromolecules* 27.26 (1994), pp. 7781–7784.

[143] A. Simperler et al. "Glass Transition Temperature of Glucose, Sucrose, and Trehalose: An Experimental and in Silico Study". *The Journal of Physical Chemistry B* 110.39 (2006), pp. 19678–19684.

[144] A. Soldera. "Comparison Between the Glass Transition Temperatures of the Two PMMA Tacticities: A Molecular Dynamics Simulation Point of View". In: *Macromolecular Symposia*. Vol. 133. 1. Wiley Online Library. 1998, pp. 21–32.

[145] M. D. Ediger, C. Angell, and S. R. Nagel. "Supercooled Liquids and Glasses". *The Journal of Physical Chemistry* 100.31 (1996), pp. 13200–13212.

[146] D. R. Burfield. "Polymer Glass Transition Temperatures". *Journal of Chemical Education* 64.10 (1987), p. 875.

[147] S. Pronk et al. "GROMACS 4.5: A High-Throughput and Highly Parallel Open Source Molecular Simulation Toolkit". *Bioinformatics* 29.7 (2013). Version 5.0.2, pp. 845–854.

[148] H. J. Berendsen, J. P. Postma, W. F. van Gunsteren, and J. Hermans. "Interaction Models for Water in Relation to Protein Hydration". In: *Intermolecular forces*. Springer, 1981, pp. 331–342.

[149] J. G. Harris and K. H. Yung. "Carbon Dioxide's Liquid-Vapor Coexistence Curve and Critical Properties as Predicted by a Simple Molecular Model". *The Journal of Physical Chemistry* 99.31 (1995), pp. 12021–12024.

[150] K. S. Shing and S. T. Chung. "Computer Simulation Methods for the Calculation of Solubility in Supercritical Extraction Systems". *The Journal of Physical Chemistry* 91.6 (1987), pp. 1674–1681.

[151] C. H. Rycroft, G. S. Grest, J. W. Landry, and M. Z. Bazant. "Analysis of Granular Flow in a Pebble-Bed Nuclear Reactor". *Physical Review E* 74.2 (2006), p. 021306.

[152] D. N. Politis, J. P. Romano, and M. Wolf. *Subsampling*. Springer, 1999.

[153] A. Kleiner, A. Talwalkar, P. Sarkar, and M. Jordan. "The Big Data Bootstrap". *arXiv Preprint arXiv:1206.6415* (2012).

[154] B. Efron and R. J. Tibshirani. *An Introduction to the Bootstrap*. CRC press, 1994.

[155] H. Childs et al. "VisIt: An End-User Tool For Visualizing and Analyzing Very Large Data". In: *High Performance Visualization–Enabling Extreme-Scale Scientific Insight*. 2012, pp. 357–372.

[156] J. E. Basconi and M. R. Shirts. "Effects of Temperature Control Algorithms on Transport Properties and Kinetics in Molecular Dynamics Simulations". *Journal of Chemical Theory and Computation* 9.7 (2013), pp. 2887–2899.

[157] H. C. Andersen. "RATTLE: A "Velocity" Version of the SHAKE Algorithm for Molecular Dynamics Calculations". *Journal of Computational Physics* 52.1 (1983), pp. 24–34.

[158] E. M. Myshakin, W. A. Saidi, V. N. Romanov, R. T. Cygan, and K. D. Jordan. "Molecular Dynamics Simulations of Carbon Dioxide Intercalation in Hydrated Na-Montmorillonite". *The Journal of Physical Chemistry C* 117.21 (2013), pp. 11028–11039.

[159] J. H. Wang. "Self-Diffusion Coefficients of Water". *The Journal of Physical Chemistry* 69.12 (1965), pp. 4412–4412.

[160] A. Gent and P. Lindley. "Internal Rupture of Bonded Rubber Cylinders in Tension". In: *Proceedings of the Royal Society of London A: Mathematical, Physical and Engineering Sciences*. Vol. 249. 1257. The Royal Society. 1959, pp. 195–205.

[161] B. S. Bokstein, M. I. Mendelev, and D. J. Srolovitz. *Thermodynamics and Kinetics in Materials Science: A Short Course*. Oxford University Press, 2005.

[162] D. R. Rottach et al. "Molecular Dynamics Simulations of Polymer Networks Undergoing Sequential Cross-Linking and Scission Reactions". *Macromolecules* 40.1 (2007), pp. 131–139.

[163] N. Molinari. *CGModel source code*. https://github.com/Nicola89/CGmodel. Accessed 09-2016. 2015.

[164] G. Severe and J. L. White. "Physical Properties and Blend Miscibility of Hydrogenated Acrylonitrile-Butadiene Rubber". *Journal of Applied Polymer Science* 78.8 (2000), pp. 1521–1529.

[165] R. Parg, C. Wrana, and D. Achten. *Therban Advanced Technology. The New Low Molecular Weight HNBR*. http://www.plastverarbeiter.de/ai/resources/65d192dcbdf.pdf. Accessed: 12-2016.

[166] C. Wrana, K. Reinartz, and H. R. Winkelbach. "Therban®–The High Performance Elastomer for the New Millennium". *Macromolecular Materials and Engineering* 286.11 (2001), pp. 657–662.

[167] F. Müller-Plathe. "Coarse-Graining in Polymer Simulation: From the Atomistic to the Mesoscopic Scale and Back". *ChemPhysChem* 3.9 (2002), pp. 754–769.

A

Force-field parameters

A.1 Nitrile butadiene rubber

The OPLS-AA force-field [26] was used to describe the polymer, in which the potential energy takes the form:

$$E = \sum_{\text{bonds}} \frac{1}{2} k_x (x - x_0)^2 + \sum_{\text{angles}} \frac{1}{2} k_y (y - y_0)^2 + \sum_{\text{dihedrals}} \sum_{n=1}^{4} \frac{1}{2} k_{zn} \left[1 - (-1)^n \cos(nz)\right] + \sum_{i>j} 4\varepsilon_{ij} f_{ij} \left[\left(\frac{\sigma_{ij}}{x_{ij}} \right)^{12} - \left(\frac{\sigma_{ij}}{x_{ij}} \right)^{6} \right] + \sum_{i>j} e^2 f_{ij} \frac{q_i q_j}{x_{ij}} , \tag{A.1}$$

where $f_{ij} = \frac{1}{2}$ if atoms i and j are separated by three bonds, $f_{ij} = 1$ if they are separated by more than three bonds, and $f_{ij} = 0$ otherwise. Geometric combination rules are used, i.e., $\sigma_{ij} = \sqrt{\sigma_{ii}\sigma_{jj}}$ and $\varepsilon_{ij} = \sqrt{\varepsilon_{ii}\varepsilon_{jj}}$. The parameters are shown in Tables A.1, A.2, A.3 and A.4.

Atom types						
Element	Type	Mass ($g\,mol^{-1}$)	σ (nm)	ε ($kcal\,mol^{-1}$)	q (e)	Note
Carbon (sp^3)	CT	12.011	0.35	0.066	−0.18	C in CH_3
Carbon (sp^3)	CT	12.011	0.35	0.066	−0.12	C in CH_2
Carbon (sp^3)	CT	12.011	0.33	0.066	−0.02	C of CH_2 in $(CH_2)-C\equiv N$
Carbon (sp^3)	CT	12.011	0.33	0.066	0.04	C of CH in $(CH)-C\equiv N$
Carbon (sp^2)	CM	12.011	0.355	0.076	−0.115	C in $(CH)=(CH)$
Carbon (sp)	CZ	12.011	0.33	0.066	0.46	C in $C\equiv N$
Nitrogen	NZ	14.007	0.32	0.17	−0.56	N in $C\equiv N$
Hydrogen	HC	1.008	0.25	0.03	0.06	H in $CH_{2,3}$
Hydrogen	HC	1.008	0.242	0.03	0.115	H in $(CH)=(CH)$
Hydrogen	HC	1.008	0.25	0.015	0.06	H in $(CH_{1,2})-C\equiv N$

Table A.1: OPLS force-field atom types for NBR.

Bond types		
Bonds	k_x ($kcal\,mol^{-1}\,nm^{-2}$)	x_0 (nm)
CT−CT	53 600	0.1529
CT−CM	63 400	0.151
CT−CZ	78 000	0.147
CT−HC	68 000	0.109
CM=CM	109 800	0.134
CM−HC	68 000	0.108
CZ≡NZ	130 000	0.1157

Table A.2: OPLS force-field bond types for NBR.

Angle types Angles	k_y (kcal mol^{-1} rad^{-2})	y_0 (°)
CT—CT—CT	116.7	112.7
CT—CT—CM	126	111.1
CT—CT—CZ	116.7	112.7
CT—CT—HC	75	110.7
CT—CM=CM	140	124
CT—CZ≡NZ	300	180
CT—CM—HC	70	117
CM—CT—HC	70	109.5
CM=CM—HC	70	120
CZ—CT—HC	70	108.5
HC—CT—HC	66	107.8

Table A.3: OPLS force-field angle types for NBR.

Dihedral types Dihedrals	k_{z_1} (kcal mol^{-1})	k_{z_2} (kcal mol^{-1})	k_{z_3} (kcal mol^{-1})	k_{z_4} (kcal mol^{-1})
CT—CT—CT—CT	1.3	−0.05	0.2	0
CT—CT—CT—CM	1.3	−0.05	0.2	0
CT—CT—CT—CZ	0	0	0	0
CT—CT—CT—HC	0	0	0.3	0
CT—CT—CM=CM	0.346	0.405	−0.904	0
CT—CT—CM—HC	0	0	0	0
CT—CT—CZ≡NZ	0	0	0	0
CT—CM=CM—CT	0	14	0	0
CT—CM=CM—HC	0	14	0	0
CM—CT—CT—CM	0	0	0	0
CM—CT—CT—CZ	0	0	0	0
CM—CT—CT—HC	0	0	0.366	0
CM=CM—CT—HC	0	0	−0.372	0
CZ—CT—CT—HC	0	0	0.366	0
NZ—CZ—CT≡HC	0	0	0	0
HC—CT—CT—HC	0	0	0.3	0
HC—CT—CM—HC	0	0	0.318	0
HC—CM=CM—HC	0	14	0	0

Table A.4: OPLS force-field dihedral types for NBR.

A.2 Gases

Tables A.5 and A.6 show the non-bonded and bonded parameters for the gases for which solubilities and diffusivities were computed.

Molecule	Atom	σ (nm)	ε (kcal mol^{-1})	q (e)	Source
He	He	0.2556	0.02	0	OPLS [26]
CO_2	C	0.2757	0.0559	0.6512	EPM2 [149]
	O	0.3033	0.16	−0.3256	
CO_2	C	0.28	0.0559	0.6512	Myshakin *et al.* [158]
	O	0.3028	0.1597	−0.3256	
H_2O	H	0	0	0.41	SPC [148]
	O	0.3166	0.1554	−0.82	

Table A.5: Non-bonded force-field parameters for gases studied

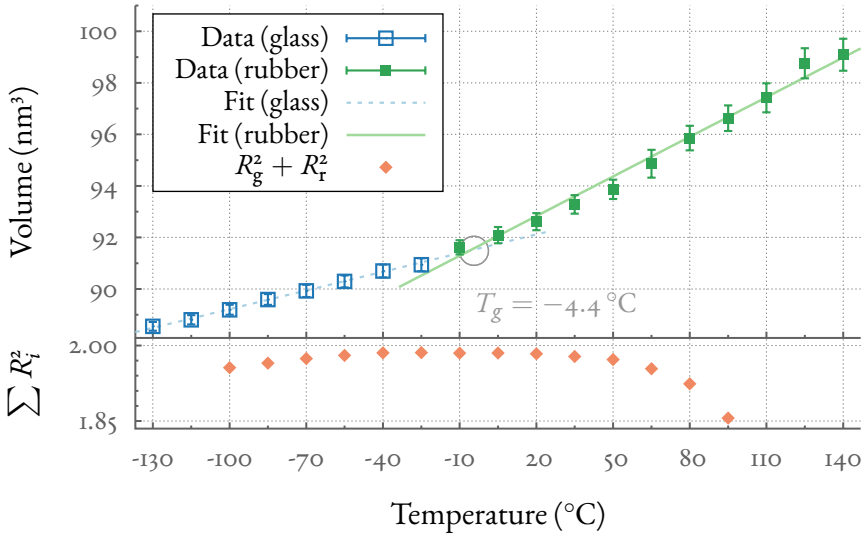
Molecule	x_0 (nm)	k_x (kcal mol^{-1} nm^{-2})	y_0 (°)	k_y (kcal mol^{-1} rad^{-2})	Source
CO_2	0.1149	–	180	295	EPM2 [149]
	0.1162	201 800	180	108	Myshakin *et al.* [158]
H_2O	0.1	82 500	109.47	91.5	SPC [148]

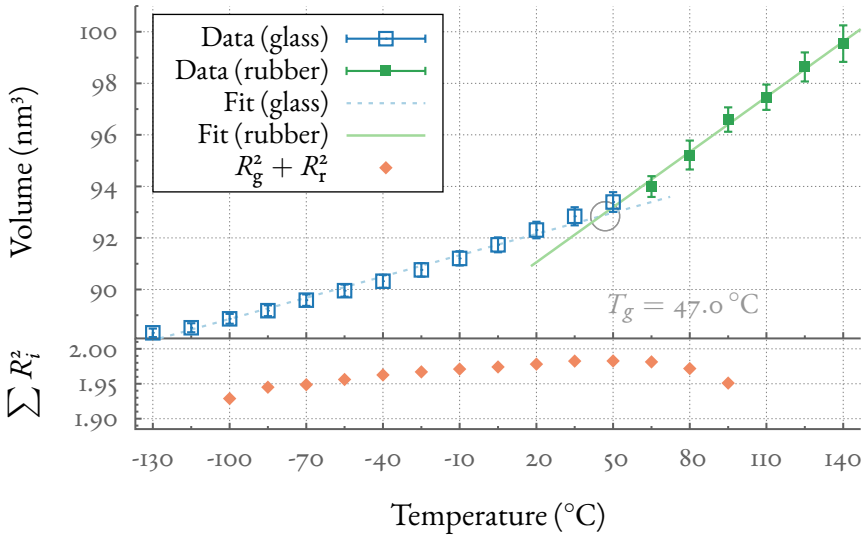
Table A.6: Bonded force-field parameters for gases studied

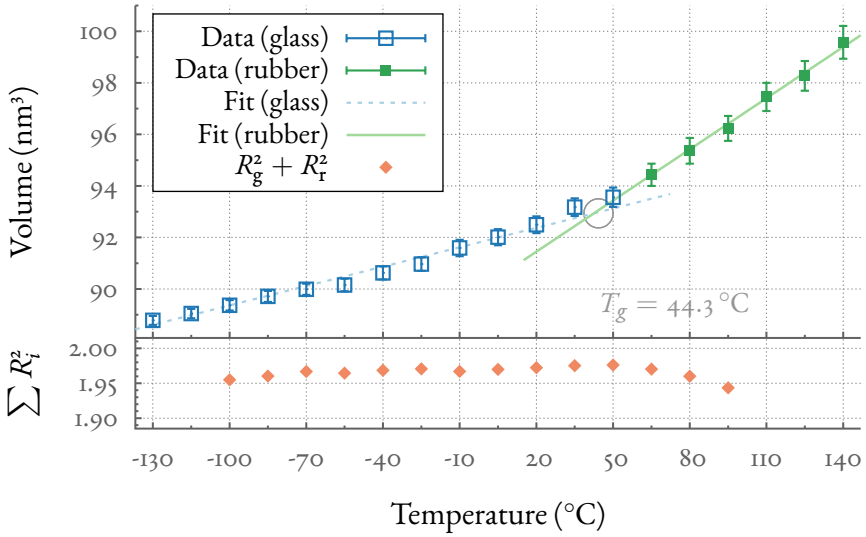
B

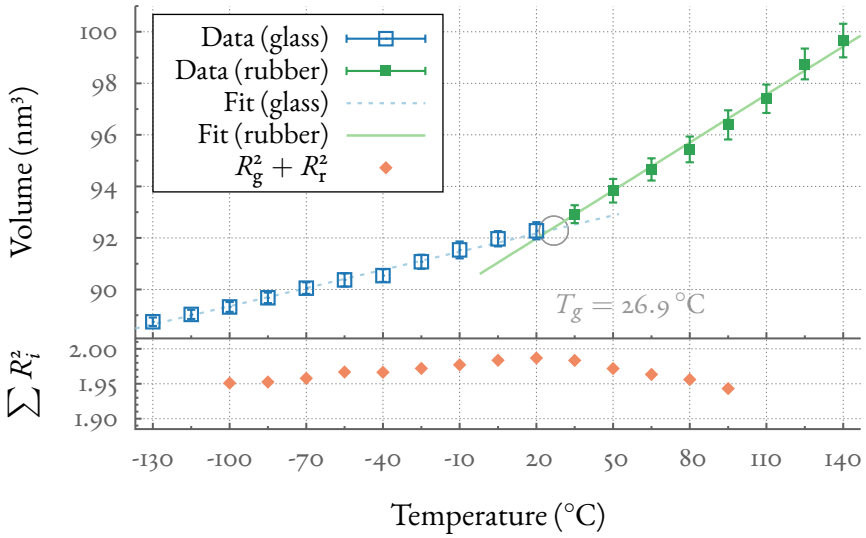
Supplementary volume-temperature plots

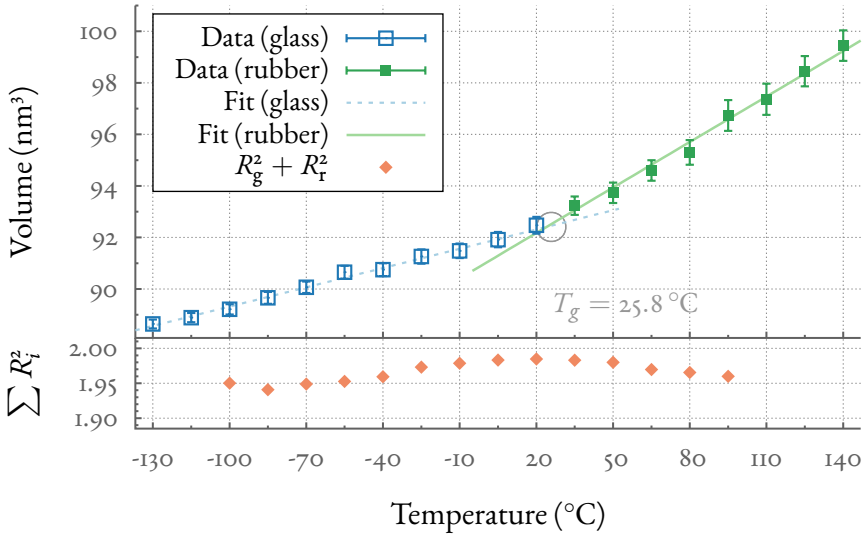
In this appendix I present additional volume-temperature plots used in the computation of T_g in chapter 4, to illustrate the variation in T_g and $\sum R_i^2$ across different independent configurations of NBR of the same underlying ACN content (41.3 %).

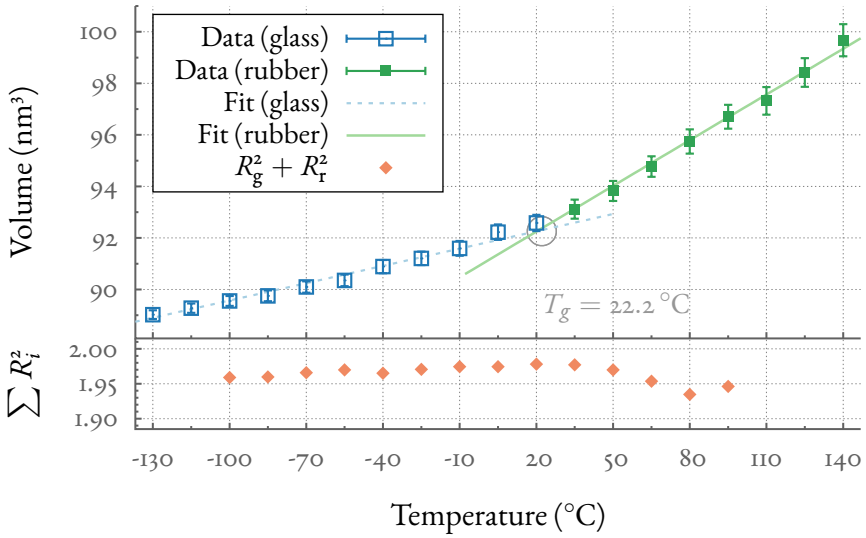

Data (glass)
Data (rubber)
Fit (glass)
Fit (rubber)
$R_g^2 + R_r^2$
$T_g = -4.4\,°C$
Volume (nm³)
$\sum R_i^2$
100
98
96
94
92
90
2.00
1.85
-130
-100
-70
-40
-10
20
50
80
110
140
Temperature (°C)

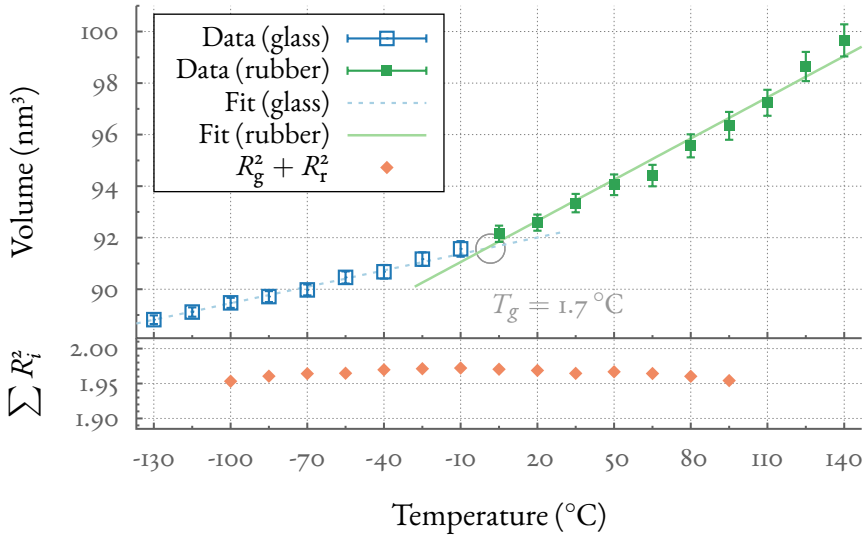

Data (glass)
Data (rubber)
Fit (glass)
Fit (rubber)
$R_g^2 + R_r^2$
$T_g = 47.0\,°C$
Volume (nm³)
$\sum R_i^2$
100
98
96
94
92
90
2.00
1.95
1.90
-130
-100
-70
-40
-10
20
50
80
110
140
Temperature (°C)


Data (glass)
Data (rubber)
Fit (glass)
Fit (rubber)
$R_g^2 + R_r^2$
Volume (nm³)
100
98
96
94
92
90
$T_g = 44.3$ °C
$\sum R_i^2$
2.00
1.95
1.90
-130
-100
-70
-40
-10
20
50
80
110
140
Temperature (°C)


Data (glass)
Data (rubber)
Fit (glass)
Fit (rubber)
$R_g^2 + R_r^2$
Volume (nm³)
100
98
96
94
92
90
$T_g = 26.9$ °C
$\sum R_i^2$
2.00
1.95
1.90
-130
-100
-70
-40
-10
20
50
80
110
140
Temperature (°C)


Data (glass)
Data (rubber)
Fit (glass)
Fit (rubber)
$R_g^2 + R_r^2$
$T_g = 25.8\,°C$
Volume (nm³)
$\sum R_i^2$
100
98
96
94
92
90
2.00
1.95
1.90
-130
-100
-70
-40
-10
20
50
80
110
140
Temperature (°C)


Data (glass)
Data (rubber)
Fit (glass)
Fit (rubber)
$R_g^2 + R_r^2$
$T_g = 22.2\,°C$
Volume (nm³)
$\sum R_i^2$
100
98
96
94
92
90
2.00
1.95
1.90
-130
-100
-70
-40
-10
20
50
80
110
140
Temperature (°C)


Data (glass)
Data (rubber)
Fit (glass)
Fit (rubber)
$R_g^2 + R_r^2$
T_g = 1.7 °C
Volume (nm³)
$\sum R_i^2$
100
98
96
94
92
90
2.00
1.95
1.90
-130
-100
-70
-40
-10
20
50
80
110
140
Temperature (°C)

C

Republication permissions

Figure 2.5 reproduced from Jha *et al.* [73]

JOHN WILEY AND SONS LICENSE TERMS AND CONDITIONS

Aug 23, 2016

This Agreement between Mohammed Musab Khawaja ("You") and John Wiley and Sons ("John Wiley and Sons") consists of your license details and the terms and conditions provided by John Wiley and Sons and Copyright Clearance Center.

License Number	3934840249650
License date	Aug 23, 2016
Licensed Content Publisher	John Wiley and Sons
Licensed Content Publication	Journal of Applied Polymer Science
Licensed Content Title	Reversible electrical behavior with strain for a carbon black-filled rubber
Licensed Content Author	V. Jha,A. G. Thomas,M. Bennett,J. J. C. Busfield
Licensed Content Date	Dec 1, 2009
Licensed Content Pages	6
Type of use	Dissertation/Thesis
Requestor type	University/Academic
Format	Print and electronic
Portion	Figure/table
Number of figures/tables	1
Original Wiley figure/table number(s)	Figure 1
Will you be translating?	No
Title of your thesis / dissertation	Modelling the Permeability of Nitrile Rubber
Expected completion date	Sep 2016
Expected size (number of pages)	150
Requestor Location	Mohammed Musab Khawaja Imperial College Exhibition Road London, other BA7 7DX United Kingdom Attn:
Publisher Tax ID	EU826007151
Billing Type	Invoice
Billing Address	Mohammed Musab Khawaja Imperial College Exhibition Road London, United Kingdom BA7 7DX Attn: Mohammed Musab Khawaja
Total	0.00 GBP
Terms and Conditions	

TERMS AND CONDITIONS

This copyrighted material is owned by or exclusively licensed to John Wiley & Sons, Inc. or one of its group companies (each a"Wiley Company") or handled on behalf of a society with

which a Wiley Company has exclusive publishing rights in relation to a particular work (collectively "WILEY"). By clicking "accept" in connection with completing this licensing transaction, you agree that the following terms and conditions apply to this transaction (along with the billing and payment terms and conditions established by the Copyright Clearance Center Inc., ("CCC's Billing and Payment terms and conditions"), at the time that you opened your RightsLink account (these are available at any time at http://myaccount.copyright.com).

Terms and Conditions

- The materials you have requested permission to reproduce or reuse (the "Wiley Materials") are protected by copyright.

- You are hereby granted a personal, non-exclusive, non-sub licensable (on a stand-alone basis), non-transferable, worldwide, limited license to reproduce the Wiley Materials for the purpose specified in the licensing process. This license, **and any CONTENT (PDF or image file) purchased as part of your order,** is for a one-time use only and limited to any maximum distribution number specified in the license. The first instance of republication or reuse granted by this license must be completed within two years of the date of the grant of this license (although copies prepared before the end date may be distributed thereafter). The Wiley Materials shall not be used in any other manner or for any other purpose, beyond what is granted in the license. Permission is granted subject to an appropriate acknowledgement given to the author, title of the material/book/journal and the publisher. You shall also duplicate the copyright notice that appears in the Wiley publication in your use of the Wiley Material. Permission is also granted on the understanding that nowhere in the text is a previously published source acknowledged for all or part of this Wiley Material. Any third party content is expressly excluded from this permission.

- With respect to the Wiley Materials, all rights are reserved. Except as expressly granted by the terms of the license, no part of the Wiley Materials may be copied, modified, adapted (except for minor reformatting required by the new Publication), translated, reproduced, transferred or distributed, in any form or by any means, and no derivative works may be made based on the Wiley Materials without the prior permission of the respective copyright owner.**For STM Signatory Publishers clearing permission under the terms of the STM Permissions Guidelines only, the terms of the license are extended to include subsequent editions and for editions in other languages, provided such editions are for the work as a whole in situ and does not involve the separate exploitation of the permitted figures or extracts,** You may not alter, remove or suppress in any manner any copyright, trademark or other notices displayed by the Wiley Materials. You may not license, rent, sell, loan, lease, pledge, offer as security, transfer or assign the Wiley Materials on a stand-alone basis, or any of the rights granted to you hereunder to any other person.

- The Wiley Materials and all of the intellectual property rights therein shall at all times remain the exclusive property of John Wiley & Sons Inc, the Wiley Companies, or their respective licensors, and your interest therein is only that of having possession of and the right to reproduce the Wiley Materials pursuant to Section 2 herein during the continuance of this Agreement. You agree that you own no right, title or interest in or to the Wiley Materials or any of the intellectual property rights therein. You shall have no rights hereunder other than the license as provided for above in Section 2. No right, license or interest to any trademark, trade name, service mark or other branding ("Marks") of WILEY or its licensors is granted hereunder, and you agree that you shall not assert any such right, license or interest with respect thereto

- NEITHER WILEY NOR ITS LICENSORS MAKES ANY WARRANTY OR REPRESENTATION OF ANY KIND TO YOU OR ANY THIRD PARTY, EXPRESS, IMPLIED OR STATUTORY, WITH RESPECT TO THE MATERIALS

OR THE ACCURACY OF ANY INFORMATION CONTAINED IN THE MATERIALS, INCLUDING, WITHOUT LIMITATION, ANY IMPLIED WARRANTY OF MERCHANTABILITY, ACCURACY, SATISFACTORY QUALITY, FITNESS FOR A PARTICULAR PURPOSE, USABILITY, INTEGRATION OR NON-INFRINGEMENT AND ALL SUCH WARRANTIES ARE HEREBY EXCLUDED BY WILEY AND ITS LICENSORS AND WAIVED BY YOU.

- WILEY shall have the right to terminate this Agreement immediately upon breach of this Agreement by you.
- You shall indemnify, defend and hold harmless WILEY, its Licensors and their respective directors, officers, agents and employees, from and against any actual or threatened claims, demands, causes of action or proceedings arising from any breach of this Agreement by you.
- IN NO EVENT SHALL WILEY OR ITS LICENSORS BE LIABLE TO YOU OR ANY OTHER PARTY OR ANY OTHER PERSON OR ENTITY FOR ANY SPECIAL, CONSEQUENTIAL, INCIDENTAL, INDIRECT, EXEMPLARY OR PUNITIVE DAMAGES, HOWEVER CAUSED, ARISING OUT OF OR IN CONNECTION WITH THE DOWNLOADING, PROVISIONING, VIEWING OR USE OF THE MATERIALS REGARDLESS OF THE FORM OF ACTION, WHETHER FOR BREACH OF CONTRACT, BREACH OF WARRANTY, TORT, NEGLIGENCE, INFRINGEMENT OR OTHERWISE (INCLUDING, WITHOUT LIMITATION, DAMAGES BASED ON LOSS OF PROFITS, DATA, FILES, USE, BUSINESS OPPORTUNITY OR CLAIMS OF THIRD PARTIES), AND WHETHER OR NOT THE PARTY HAS BEEN ADVISED OF THE POSSIBILITY OF SUCH DAMAGES. THIS LIMITATION SHALL APPLY NOTWITHSTANDING ANY FAILURE OF ESSENTIAL PURPOSE OF ANY LIMITED REMEDY PROVIDED HEREIN.
- Should any provision of this Agreement be held by a court of competent jurisdiction to be illegal, invalid, or unenforceable, that provision shall be deemed amended to achieve as nearly as possible the same economic effect as the original provision, and the legality, validity and enforceability of the remaining provisions of this Agreement shall not be affected or impaired thereby.
- The failure of either party to enforce any term or condition of this Agreement shall not constitute a waiver of either party's right to enforce each and every term and condition of this Agreement. No breach under this agreement shall be deemed waived or excused by either party unless such waiver or consent is in writing signed by the party granting such waiver or consent. The waiver by or consent of a party to a breach of any provision of this Agreement shall not operate or be construed as a waiver of or consent to any other or subsequent breach by such other party.
- This Agreement may not be assigned (including by operation of law or otherwise) by you without WILEY's prior written consent.
- Any fee required for this permission shall be non-refundable after thirty (30) days from receipt by the CCC.
- These terms and conditions together with CCC's Billing and Payment terms and conditions (which are incorporated herein) form the entire agreement between you and WILEY concerning this licensing transaction and (in the absence of fraud) supersedes all prior agreements and representations of the parties, oral or written. This Agreement may not be amended except in writing signed by both parties. This Agreement shall be binding upon and inure to the benefit of the parties' successors, legal representatives,

and authorized assigns.

- In the event of any conflict between your obligations established by these terms and conditions and those established by CCC's Billing and Payment terms and conditions, these terms and conditions shall prevail.
- WILEY expressly reserves all rights not specifically granted in the combination of (i) the license details provided by you and accepted in the course of this licensing transaction, (ii) these terms and conditions and (iii) CCC's Billing and Payment terms and conditions.
- This Agreement will be void if the Type of Use, Format, Circulation, or Requestor Type was misrepresented during the licensing process.
- This Agreement shall be governed by and construed in accordance with the laws of the State of New York, USA, without regards to such state's conflict of law rules. Any legal action, suit or proceeding arising out of or relating to these Terms and Conditions or the breach thereof shall be instituted in a court of competent jurisdiction in New York County in the State of New York in the United States of America and each party hereby consents and submits to the personal jurisdiction of such court, waives any objection to venue in such court and consents to service of process by registered or certified mail, return receipt requested, at the last known address of such party.

WILEY OPEN ACCESS TERMS AND CONDITIONS
Wiley Publishes Open Access Articles in fully Open Access Journals and in Subscription journals offering Online Open. Although most of the fully Open Access journals publish open access articles under the terms of the Creative Commons Attribution (CC BY) License only, the subscription journals and a few of the Open Access Journals offer a choice of Creative Commons Licenses. The license type is clearly identified on the article.
The Creative Commons Attribution License
The Creative Commons Attribution License (CC-BY) allows users to copy, distribute and transmit an article, adapt the article and make commercial use of the article. The CC-BY license permits commercial and non-
Creative Commons Attribution Non-Commercial License
The Creative Commons Attribution Non-Commercial (CC-BY-NC)License permits use, distribution and reproduction in any medium, provided the original work is properly cited and is not used for commercial purposes.(see below)

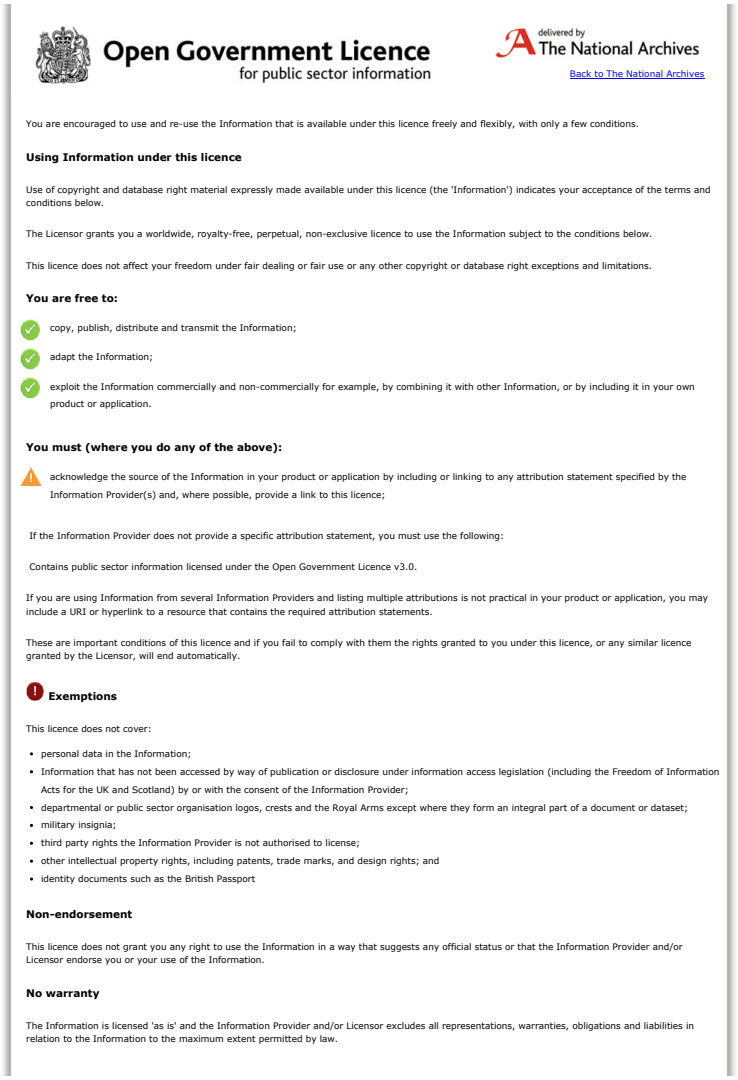
Creative Commons Attribution-Non-Commercial-NoDerivs License
The Creative Commons Attribution Non-Commercial-NoDerivs License (CC-BY-NC-ND) permits use, distribution and reproduction in any medium, provided the original work is properly cited, is not used for commercial purposes and no modifications or adaptations are made. (see below)
Use by commercial "for-profit" organizations
Use of Wiley Open Access articles for commercial, promotional, or marketing purposes requires further explicit permission from Wiley and will be subject to a fee.
Further details can be found on Wiley Online Library
http://olabout.wiley.com/WileyCDA/Section/id-410895.html

Other Terms and Conditions:

v1.10 Last updated September 2015

Questions? customercare@copyright.com or +1-855-239-3415 (toll free in the US) or +1-978-646-2777.

Figure 2.7 reproduced from Ho *et al.* [79] under the Open Government Licence.



Open Government Licence
for public sector information

delivered by The National Archives

Back to The National Archives

You are encouraged to use and re-use the Information that is available under this licence freely and flexibly, with only a few conditions.

Using Information under this licence

Use of copyright and database right material expressly made available under this licence (the 'Information') indicates your acceptance of the terms and conditions below.

The Licensor grants you a worldwide, royalty-free, perpetual, non-exclusive licence to use the Information subject to the conditions below.

This licence does not affect your freedom under fair dealing or fair use or any other copyright or database right exceptions and limitations.

You are free to:

- copy, publish, distribute and transmit the Information;
- adapt the Information;
- exploit the Information commercially and non-commercially for example, by combining it with other Information, or by including it in your own product or application.

You must (where you do any of the above):

- acknowledge the source of the Information in your product or application by including or linking to any attribution statement specified by the Information Provider(s) and, where possible, provide a link to this licence;

If the Information Provider does not provide a specific attribution statement, you must use the following:

Contains public sector information licensed under the Open Government Licence v3.0.

If you are using Information from several Information Providers and listing multiple attributions is not practical in your product or application, you may include a URI or hyperlink to a resource that contains the required attribution statements.

These are important conditions of this licence and if you fail to comply with them the rights granted to you under this licence, or any similar licence granted by the Licensor, will end automatically.

Exemptions

This licence does not cover:

- personal data in the Information;
- Information that has not been accessed by way of publication or disclosure under information access legislation (including the Freedom of Information Acts for the UK and Scotland) by or with the consent of the Information Provider;
- departmental or public sector organisation logos, crests and the Royal Arms except where they form an integral part of a document or dataset;
- military insignia;
- third party rights the Information Provider is not authorised to license;
- other intellectual property rights, including patents, trade marks, and design rights; and
- identity documents such as the British Passport

Non-endorsement

This licence does not grant you any right to use the Information in a way that suggests any official status or that the Information Provider and/or Licensor endorse you or your use of the Information.

No warranty

The Information is licensed 'as is' and the Information Provider and/or Licensor excludes all representations, warranties, obligations and liabilities in relation to the Information to the maximum extent permitted by law.

The Information Provider and/or Licensor are not liable for any errors or omissions in the Information and shall not be liable for any loss, injury or damage of any kind caused by its use. The Information Provider does not guarantee the continued supply of the Information.

Governing Law

This licence is governed by the laws of the jurisdiction in which the Information Provider has its principal place of business, unless otherwise specified by the Information Provider.

Definitions

In this licence, the terms below have the following meanings:

'Information' means information protected by copyright or by database right (for example, literary and artistic works, content, data and source code) offered for use under the terms of this licence.

'Information Provider' means the person or organisation providing the Information under this licence.

'Licensor' means any Information Provider which has the authority to offer Information under the terms of this licence or the Controller of Her Majesty's Stationery Office, who has the authority to offer Information subject to Crown copyright and Crown database rights and Information subject to copyright and database right that has been assigned to or acquired by the Crown, under the terms of this licence.

'Use' means doing any act which is restricted by copyright or database right, whether in the original medium or in any other medium, and includes without limitation distributing, copying, adapting, modifying as may be technically necessary to use it in a different mode or format.

'You', 'you' and 'your' means the natural or legal person, or body of persons corporate or incorporate, acquiring rights in the Information (whether the Information is obtained directly from the Licensor or otherwise) under this licence.

About the Open Government Licence

The Controller of Her Majesty's Stationery Office (HMSO) has developed this licence as a tool to enable Information Providers in the public sector to license the use and re-use of their Information under a common open licence. The Controller invites public sector bodies owning their own copyright and database rights to permit the use of their Information under this licence.

The Controller of HMSO has authority to license Information subject to copyright and database right owned by the Crown. The extent of the Controller's offer to license this Information under the terms of this licence is set out in the UK Government Licensing Framework.

This is version 3.0 of the Open Government Licence. The Controller of HMSO may, from time to time, issue new versions of the Open Government Licence. If you are already using Information under a previous version of the Open Government Licence, the terms of that licence will continue to apply.

These terms are compatible with the Creative Commons Attribution License 4.0 and the Open Data Commons Attribution License, both of which license copyright and database rights. This means that when the Information is adapted and licensed under either of those licences, you automatically satisfy the conditions of the OGL when you comply with the other licence. The OGLv3.0 is Open Definition compliant.

Further context, best practice and guidance can be found in the UK Government Licensing Framework section on The National Archives website.

OGL

Go to the version 1 of the licence.
Go to the version 2 of the licence.
Go to the Welsh version of the licence.

Figures 3.2 and 3.3 reproduced from Van Amerongen [92].

AIP PUBLISHING LLC LICENSE
TERMS AND CONDITIONS

Aug 23, 2016

This Agreement between Mohammed Musab Khawaja ("You") and AIP Publishing LLC ("AIP Publishing LLC") consists of your license details and the terms and conditions provided by AIP Publishing LLC and Copyright Clearance Center.

License Number	3934841391696
License date	Aug 23, 2016
Licensed Content Publisher	AIP Publishing LLC
Licensed Content Publication	Journal of Applied Physics
Licensed Content Title	The Permeability of Different Rubbers to Gases and Its Relation to Diffusivity and Solubility
Licensed Content Author	G. J. Van Amerongen
Licensed Content Date	Apr 15, 2004
Licensed Content Volume Number	17
Licensed Content Issue Number	11
Type of Use	Thesis/Dissertation
Requestor type	Student
Format	Print and electronic
Portion	Figure/Table
Number of figures/tables	2
Title of your thesis / dissertation	Modelling the Permeability of Nitrile Rubber
Expected completion date	Sep 2016
Estimated size (number of pages)	150
Requestor Location	Mohammed Musab Khawaja Imperial College Exhibition Road London, other BA7 7DX United Kingdom Attn:
Billing Type	Invoice
Billing Address	Mohammed Musab Khawaja Imperial College Exhibition Road London, United Kingdom BA7 7DX Attn: Mohammed Musab Khawaja
Total	0.00 GBP
Terms and Conditions	

AIP Publishing LLC -- Terms and Conditions: Permissions Uses

AIP Publishing hereby grants to you the non-exclusive right and license to use and/or distribute the Material according to the use specified in your order, on a one-time basis, for the specified term, with a maximum distribution equal to the number that you have ordered. Any links or other content accompanying the Material are not the subject of this license.

1. You agree to include the following copyright and permission notice with the reproduction of the Material:"Reprinted from [FULL CITATION], with the permission of AIP Publishing." For an article, the credit line and permission notice must be printed on the first page of the article or book chapter. For photographs, covers, or tables, the notice may appear with the Material, in a footnote, or in the reference list.
2. If you have licensed reuse of a figure, photograph, cover, or table, it is your responsibility to ensure that the material is original to AIP Publishing and does not contain the copyright of another entity, and that the copyright notice of the figure, photograph, cover, or table does not indicate that it was reprinted by AIP Publishing, with permission, from another source. Under no circumstances does AIP Publishing purport or intend to grant permission to reuse material to which it does not hold appropriate rights.
   You may not alter or modify the Material in any manner. You may translate the Material into another language only if you have licensed translation rights. You may not use the Material for promotional purposes.
3. The foregoing license shall not take effect unless and until AIP Publishing or its agent, Copyright Clearance Center, receives the Payment in accordance with Copyright Clearance Center Billing and Payment Terms and Conditions, which are incorporated herein by reference.
4. AIP Publishing or Copyright Clearance Center may, within two business days of granting this license, revoke the license for any reason whatsoever, with a full refund payable to you. Should you violate the terms of this license at any time, AIP Publishing, or Copyright Clearance Center may revoke the license with no refund to you. Notice of such revocation will be made using the contact information provided by you. Failure to receive such notice will not nullify the revocation.
5. AIP Publishing makes no representations or warranties with respect to the Material. You agree to indemnify and hold harmless AIP Publishing, and their officers, directors, employees or agents from and against any and all claims arising out of your use of the Material other than as specifically authorized herein.
6. The permission granted herein is personal to you and is not transferable or assignable without the prior written permission of AIP Publishing. This license may not be amended except in a writing signed by the party to be charged.
7. If purchase orders, acknowledgments or check endorsements are issued on any forms containing terms and conditions which are inconsistent with these provisions, such inconsistent terms and conditions shall be of no force and effect. This document, including the CCC Billing and Payment Terms and Conditions, shall be the entire agreement between the parties relating to the subject matter hereof.

This Agreement shall be governed by and construed in accordance with the laws of the State of New York. Both parties hereby submit to the jurisdiction of the courts of New York County for purposes of resolving any disputes that may arise hereunder.

V1.1

Questions? customercare@copyright.com or +1-855-239-3415 (toll free in the US) or +1-978-646-2777.